
Southwest Atlantic intermediate and deep water circulation:
20,000 years of water mass re-organization and current strength variability

Dissertation zur Erlangung
des akademischen Grades eines Doktors der Naturwissenschaften

Dr. rer. nat.
im Fachbereich 5 (Geowissenschaften)
der Universität Bremen

vorgelegt von
Grit Warratz
geboren am 15. März 1988

Bremen, der 19. Oktober 2017

Gutachter:

Prof. Dr. Rüdiger Henrich

Fachbereich Geowissenschaften
Universität Bremen
Klagenfurter Straße 2
28359 Bremen

Prof. Dr. Bernhard Diekmann

Alfred-Wegener Institut
Helmholtz-Zentrum für Polar- und Meeresforschung
Telegrafenberg A43
14473 Potsdam

Tag des Promotionskolloquiums: 12. Dezember 2017

Preface

This cumulative doctoral thesis is the outcome of the research project Seafloor Dynamics – Climatic control on large-scale sedimentary structures (SD2) and was funded through the DFG-Research Center/Cluster of Excellence “The Ocean in the Earth System” (MARUM). This research was supported by GLOMAR - Bremen International Graduate School for Marine Sciences.

The studies compiled in this thesis were carried out in the working group Sedimentology and Paleoceanography at the Faculty of Geosciences and MARUM – Center for Marine Environmental Sciences (University of Bremen) from November 2014 until October 2017.

Grit Warratz
Oktober 2017

Versicherung an Eides Statt / *Affirmation in lieu of an oath*

**gem. § 5 Abs. 5 der Promotionsordnung vom 15.07.2015 /
according to § 5 (5) of the Doctoral Degree Rules and Regulations of 15 July, 2015**

Ich / I, Grit Warratz, Im Hollergrund 9, 28357 Bremen, Matrikel-Nr. 3025342

(Vorname / First Name, Name / Name, Anschrift / Address, ggf. Matr.-Nr. / student ID no., if applicable)

versichere an Eides Statt durch meine Unterschrift, dass ich die vorliegende Dissertation selbständig und ohne fremde Hilfe angefertigt und alle Stellen, die ich wörtlich dem Sinne nach aus Veröffentlichungen entnommen habe, als solche kenntlich gemacht habe, mich auch keiner anderen als der angegebenen Literatur oder sonstiger Hilfsmittel bedient habe und die zu Prüfungszwecken beigelegte elektronische Version (PDF) der Dissertation mit der abgegebenen gedruckten Version identisch ist. / *With my signature I affirm in lieu of an oath that I prepared the submitted dissertation independently and without illicit assistance from third parties, that I appropriately referenced any text or content from other sources, that I used only literature and resources listed in the dissertation, and that the electronic (PDF) and printed versions of the dissertation are identical.*

Ich versichere an Eides Statt, dass ich die vorgenannten Angaben nach bestem Wissen und Gewissen gemacht habe und dass die Angaben der Wahrheit entsprechen und ich nichts verschwiegen habe. / *I affirm in lieu of an oath that the information provided herein to the best of my knowledge is true and complete.*

Die Strafbarkeit einer falschen eidesstattlichen Versicherung ist mir bekannt, namentlich die Strafandrohung gemäß § 156 StGB bis zu drei Jahren Freiheitsstrafe oder Geldstrafe bei vorsätzlicher Begehung der Tat bzw. gemäß § 161 Abs. 1 StGB bis zu einem Jahr Freiheitsstrafe oder Geldstrafe bei fahrlässiger Begehung. / *I am aware that a false affidavit is a criminal offence which is punishable by law in accordance with § 156 of the German Criminal Code (StGB) with up to three years imprisonment or a fine in case of intention, or in accordance with § 161 (1) of the German Criminal Code with up to one year imprisonment or a fine in case of negligence.*

Bremen, 19.10.2017

Ort / Place, Datum / Date

Unterschrift / Signature

Content

THESIS ABSTRACT	I
ZUSAMMENFASSUNG	III
List of figures	V
List of tables	VII
List of abbreviations	VIII
Chapter 1	1
Introduction	
1.1. Motivation and scientific objectives	1
1.1.1 Deglacial re-organization of the deep water mass structure	
1.1.2 Reconstruction of deep southern component water strength	
1.1.3 Contourite-turbidite interaction within a blind canyon system	
1.1.4 Influence of Antarctic Intermediate Water on slope instabilities	
1.2 Southwest Atlantic circulation	7
1.2.1 Modern circulation	
1.2.2 Glacial circulation	
1.3 Study area	11
1.3.1 Sediment provenances of eastern South America – From source to sink	
1.3.2 Morphology of the Argentine continental margin	
1.3.3 The Argentine Contourite Depositional System	
1.3.4 The blind Mar del Plata Canyon	
1.4 Oceanographic Proxies	19
1.4.1 Sortable silt – The paleocurrent proxy	
1.4.2 Clay mineralogy – The transport pathway proxy	
1.5. Thesis outline	22
1.6 Declaration of co-author contributions	22
Chapter 2	25
Deglacial changes in the strength of deep southern component water and sediment supply at the Argentine continental margin	
<u>G. Warratz</u> , R. Henrich, I. Voigt, C. M. Chiessi, G. Kuhn, H. Lantzsch (published in <i>Paleoceanography</i> 32, doi:10.1002/2016PA003079)	
Abstract	26
2.1 Introduction	27
2.2 Background information	28

2.2.1	Physiography and oceanographic setting	
2.2.2	Clay mineral provenances	
2.3	Materials and methods	31
2.3.1	Visual core description and radiographs	
2.3.2	Age models	
2.3.3	XRF core scanning	
2.3.4	Biogenic opal, carbonate and organic carbon content	
2.3.5	Grain-size determination	
2.3.6	Clay mineral analyses	
2.4	Results	35
2.4.1	Age models and linear sedimentation rates	
2.4.2	Sedimentological classification	
2.4.3	Sortable silt	
2.4.4	Clay mineral assemblages	
2.5	Discussion	40
2.5.1	Sediment input along the deep Argentine continental margin	
2.5.2	Carbonate content and preservation – Hints for spatial and temporal variations in Southwest Atlantic deep-water mass structure?	
2.5.3	Changes in deep SCW strength since the Last Glacial Maximum	
2.6	Conclusions	47
	Acknowledgements	49
	Supporting information	50
Chapter 3	53
	Interaction of a deep-sea current with a blind submarine canyon (Mar del Plata Canyon, Argentina)	
	<u>G. Warratz</u> , T. Schwenk, I. Voigt, G. Bozzano, R. Henrich, R. Violante, H. Lantzsch (submitted to <i>Sedimentology</i> on 02 August 2017)	
	Abstract	54
3.1	Introduction	55
3.2	Background information	56
3.2.1	Oceanography and related sedimentary regimes	
3.2.2	Mar del Plata Canyon	
3.3	Material and methods	59
3.3.1	Hydroacoustics	
3.3.2	Core locations and recovery	
3.3.3	Grain-size determination	
3.3.4	Magnetic susceptibility	
3.3.5	X-ray fluorescence core scanning	
3.3.6	Radiographic imaging	

3.3.7	X-ray diffraction	
3.3.8	Stratigraphic framework	
3.4	Results	62
3.4.1	Morphological analyses of the canyon thalweg	
3.4.2	Sedimentological and depositional characteristics	
3.4.2.1	Sediment facies 1	
3.4.2.2	Sediment facies 2 – Identification of turbidite deposits	
3.4.3	Spatial and temporal turbidite distribution	
3.5	Discussion	69
3.5.1	Location of sediment failure	
3.5.2	Contourite facies	
3.5.3	Turbidite provenance and generation	
3.5.4	Timing of turbidite successions	
3.6	Conclusions	76
	Acknowledgements	78
	Supporting information	79
Chapter 4	81
	Deglacial shift of deep southern component water in the Southwest Atlantic	
	G. Warratz, I. Voigt, C. M. Chiessi, R. Henrich, H. Lantsch	
	<i>(in preparation for submission to Earth and Planetary Science Letters)</i>	
	Abstract	82
4.1	Introduction	83
4.2	Modern oceanographic setting	84
4.3	Material and methods	85
4.3.1	Age models	
4.3.2	Sortable silt grain-size measurements	
4.3.3	Total carbon, total organic carbon and carbonate content	
4.4	Results	88
4.4.1	Age models	
4.4.2	Sortable silt grain-size measurements	
4.4.3	Total organic and carbonate content	
4.5	Discussion	91
4.5.1	Deglacial changes in deep water mass source reflected by carbonate content	
4.5.2	Deglacial changes in deep water mass strength	
4.6	Conclusions	96
	Acknowledgements	98
	Supporting information	99

Chapter 5 **103**
 Conclusions and future perspectives

References **107**

Acknowledgements

Thesis Abstract

As one of the major players of the Atlantic meridional overturning circulation, the deep southern component water (SCW), comprising Lower Circumpolar Deep Water (LCDW) and Antarctic Bottom Water (AABW), ventilates the deep waters and influences global climate. However, detailed information about deep SCW strength are lacking, due to its corrosivity resulting in a lack of appropriate paleoceanographic archives. In order to improve the accuracy of ocean circulation variability, detailed deep SCW reconstructions require additional efforts from many branches of climate research. In the frame of this thesis, seven radiocarbon-dated sediment cores from the Argentine continental margin (i.e. from contourite deposits, the Mar del Plata Canyon and the deep slope) are investigated. These core sites provide the opportunity to investigate the intermediate and deep water mass circulation, e.g., deep SCW flow strength variations, of the deep Southwest Atlantic during the last 20,000 years. Furthermore, part of these sediment cores are used to analyze the poorly constrained influence of intermediate and deep ocean currents on sedimentary processes within a blind canyon system.

The first part of this thesis (Chapter 2) dedicates on deep SCW current strength variations in the Southwest Atlantic during the last 20,000 years. Changes in deep SCW strength are addressed by applying three coherent terrigenous sortable silt (SS_{mean} and $SS_{\%}$) paleocurrent-proxy records. Clay mineral investigations, as transport source path tracer, demonstrate that southern-sourced terrigenous sediment was continuously transported to the core sites since the Last Glacial Maximum (LGM). Reduced carbonate content from the LGM until 13 cal ka BP indicate an oceanographic configuration that reveals a shallower northern component water (NCW), thereby providing space for CO_3^{2-} under-saturated deep SCW. Increased carbonate content from 13 cal ka BP onwards points towards an admixture of well-ventilated NCW. This expansion of CO_3^{2-} saturated NCW most probably changed the chemical deep-water properties in the deep Southwest Atlantic causing enhanced carbonate preservation. This deep-water circulation and increased terrigenous SS_{mean} and $SS_{\%}$ indicate enhanced deep SCW flow strength from 14 to 10 cal ka BP, implying a direct influence of NCW on deep SCW flow strength. Thus, NCW re-initiation induced a vertical contraction of the deep SCW and was accompanied by a consistent migration of the high-energetic LCDW/AABW interface.

Within the second part (Chapter 3), sedimentological, mineralogical, bathymetric and Parasound data are combined to investigate the contourite-turbidite interaction within the blind Mar del Plata Canyon. Blind canyons, which do not have a connection to the shelf, are the most

common submarine canyons at continental margins, but investigations concerning their evolution and oceanographic factors influencing sedimentary processes remain sparse. The Mar del Plata Canyon on the Argentine continental margin is incorporated into a major contourite depositional system. The canyon head originates on the Ewing Terrace at about 1000 m water depth and acts as a sink for contouritic material delivered by the Antarctic Intermediate Water (AAIW) nepheloid layer. The canyon-downslope track expires on the Necochea Terrace (~ 3900 m water depth). It was shown that turbidites were restricted to the Last Glacial Maximum (LGM) until the late deglacial. During LGM and early deglacial, turbidites are more abundant at the distal northern canyon flank. Due to persistent deep SCW flow, suspended sediment clouds were deflected to the north. During the late deglacial most turbidite beds thinned out within the distal sector of the canyon. In addition, the composition of all turbidite beds pointed towards a contouritic source on the southern Ewing Terrace. Bathymetric data support that the upper part of the canyon reveals V-shaped patterns indicating areas of canyon flank instability where retrogressive failures were induced. Compared to less sediment supply during the Holocene, it is possible to relate the glacial turbidity current activity in the Mar del Plata Canyon to a strong glacial AAIW nepheloid layer sediment transport causing high sediment supply. Thus, turbidite deposits can generally be used to reconstruct changes in AAIW circulation.

The last section of this thesis (Chapter 4) focuses on the reconstruction of the vertical shift of the deep NCW/SCW and LCDW/AABW interfaces using sediment core transect from 2,800 to 4,000 m water depth. Enhanced carbonate content during the Holocene indicates the increased influence of NADW at the expense of deep SCW improving carbonate preservation. This reconstruction further supports the slight deepening of the NCW/SCW interface from the late deglacial until the Holocene (Chapter 2). An additional SS_{mean} record from the deep Argentine margin in 3,600 m water depth reveals a peak in deep SCW current strength between 15 and 11 cal ka BP. This peak was considered to represent the LCDW/AABW interface, producing stronger current strength. Comparing all SS_{mean} records of this thesis, a downward shift in the LCDW/AABW interface can be reconstructed. This interface reaches the shallowest (deepest) core site by 15 (14) cal ka BP and shifts further downward in the water column. Hence, the deglacial downward shift of this interface was introduced due (i) to NCW deepening at the expense of deep SCW spreading and (ii) enhanced LCDW inflow into the deep Southwest Atlantic during the late deglacial.

Zusammenfassung

Als entscheidende Komponente der Atlantischen Meridionalen Umwälzbewegung trägt die tiefe Südkomponentenwassermasse (SCW) grundlegend zur Ventilation der tiefen Wassermassen bei und beeinflusst primär das globale Klima. Aufgrund der Korrosivität dieser tiefen SCW sind detaillierte Rekonstruktionen von Strömungsvariationen im Südwestatlantik kaum bekannt. Diese Rekonstruktionen sind jedoch in vielen Bereichen der Klimaforschung unerlässlich, um Schwankungen im marinen Zirkulationskreislauf verstehen und analysieren zu können. Im Rahmen dieser Dissertation wurden sieben radiokarbon-datierte Sedimentkerne von dem Argentinischen Kontinentalhang untersucht, um Aufschluss über die Variabilität der Zwischen- und Tiefenwasserzirkulation des Südwestatlantiks (z. B. über Strömungsstärkenvariationen der tiefen SCW) innerhalb der letzten 20.000 Jahre zu gewinnen. Einige dieser Kerne wurden außerdem untersucht, um den bisher wenig erforschten Einfluss von Strömungen auf gravitative Massenumlagerungen in submarinen Canyons zu analysieren.

Der erste Teil der vorliegenden Arbeit (Kapitel 2) befasst sich mit der Rekonstruktion von Strömungsstärkenvariationen der tiefen SCW im Südwestatlantik innerhalb der letzten 20.000 Jahre, die aus dem Antarktischen Bodenwasser (AABW) und dem tiefen Zirkumpolaren Tiefenwasser (LCDW) zusammengesetzt ist. In diesem Rahmen werden Strömungsstärkenvariationen unter Anwendung des relativen Strömungsindikators „Sortable silt“ (SS_{mean} und $SS_{\%}$) untersucht. Insbesondere die analysierten Tonmineral-Vergesellschaftungen, als Anzeiger eines spezifischen Quellgebietes, belegen einen kontinuierlichen und nordwärts gerichteten terrigenen Sedimenttransport entlang des Argentinischen Kontinentalhanges seit dem letzten glazialen Maximum (LGM). Fehlende Karbonatgehalte bis 13 cal ka BP verdeutlichen die Ausdehnung der CO_3^{2-} un- tersättigten tiefen SCW im Südwestatlantik, wohingegen die Nordkomponentenwassermasse (NCW) in geringere Wassertiefen verdrängt wurde. Erhöhte Karbonatgehalte seit 13 cal ka BP deuten auf eine CO_3^{2-} gesättigte NCW hin, die in größere Wassertiefen vordrang und die chemische Signatur des tiefen Südwestatlantiks grundlegend veränderte. Zusätzlich kennzeichnen erhöhte terrigene SS_{mean} und $SS_{\%}$ Werte während des späten Deglazials eine erhöhte Strömungsstärke der energetischen LCDW/AABW Grenzschicht innerhalb der tiefen SCW. Demnach beeinflusste die sich in den tiefen Südwestatlantik ausbreitende NCW die vertikale Ausdehnung der tiefen SCW. Diese Strömungsvariation veranschaulicht eine kontinuierliche Verlagerung (Vertiefung) der hochenergetischen LCDW/AABW Grenzschicht vom Deglazial bis in das späte Holozän.

Der zweite Teil der Arbeit (Kapitel 3) behandelt die strömungsinduzierten Konturrit-Turbidit- Wechselwirkungen innerhalb des Mar del Plata Canyons, der über keine Anbindung zum Schelf

verfügt. Trotz der großen Masse dieser Canyons an kontinentalen Rändern sind wenige Informationen über deren Entstehung und den Einfluss von Ozeanströmungen auf Sedimentationsprozesse bekannt. Der in einem großen Konturablagerungssystem eingebundene Mar del Plata Canyon wurde anhand einer morphologischen Analyse mit bathymetrischen Datensätzen sowie Parasound Profilen ausgewertet und mit sedimentologischen und mineralogischen Daten verglichen. Da der Kopfbereich des Canyons auf der Ewing Terrasse in 1300 m Wassertiefe liegt, wird der Canyon aktuell durch den Sedimenttransport der Nepheloid-Schicht des Antarktischen Zwischenwassers (AAIW) genährt. Weiter hangabwärts läuft der Canyon auf der Necochea Terrasse in circa 3900 m Wassertiefe aus. Die Turbidit-Aktivität innerhalb des Canyons ist grundsätzlich auf das LGM und Deglazial beschränkt, wobei die auf der Necochea Terrasse auslaufenden Sedimentströme von der tiefen SCW erfasst und nach Norden verlagert wurden. Lediglich die Turbidite des späten Deglazials lagerten sich entlang des proximalen Canyon-Profiles ab, ohne den distalen Sektor zu erreichen. Identische Mineralvergesellschaftungen und Korngrößenanalysen deuten auf ein Turbidit-Quellgebiet auf der Ewing Terrasse hin. Dieser Bereich ist durch eine Amphitheater-ähnliche Morphologie geprägt, die für Instabilitäten prädestiniert ist. Demnach weist die auf das LGM und Deglazial beschränkte Turbiditaktivität auf eine erhöhte Sedimentanlieferung durch ein verstärktes bzw. verlagertes glaziales AAIW hin. Folglich kann die Turbiditaktivität innerhalb dieses Canyons als Anzeiger für Veränderungen in der AAIW Zirkulation genutzt werden.

Im letzten Abschnitt dieser Arbeit (Kapitel 4) wird erneut die Tiefenwasserstruktur des Südwestatlantiks rekonstruiert, vorrangig die vertikale Verlagerung der NCW/SCW und LCDW/AABW Grenzschichten. Die untersuchten Sedimentkerne aus einer Wassertiefe von 2.800 bis 4.000 m weisen auf einen erhöhten Karbonatgehalt seit 11 cal ka BP hin, der die Präsenz des NCW im tiefen Südwestatlantik verdeutlicht. Diese Ergebnisse ermöglichen die Rekonstruktion einer kontinuierlichen Vertiefung der NCW/SCW Grenzschicht von dem späten Deglazial bis in das Holozän. Ein neuer SS_{mean} Datensatz vom tiefen Argentinischen Kontinentalhang in 3.600 m Wassertiefe zeigt ein Wertemaximum von 15 bis 11 cal ka BP, welches die hochenergetische LCDW/AABW Grenzschicht mit erhöhten Strömungsstärken charakterisiert. Durch den Vergleich aller Paläo-Strömungsdatsätze dieses Kontinentalhanges konnte die vertikale Verlagerung dieser Grenzschicht detailliert rekonstruiert werden. Demnach erreichte die Grenzschicht die flachste (tiefste) Kernlokation vor 15 (14) ka BP und verlagerte sich während des Holozäns in größere Wassertiefen. Diese Wassermassenverlagerung wird mit der (i) deglazialen Verlagerung des NCW und der vertikalen Einengung der tiefen SCW, sowie (ii) der erhöhten LCDW Bildung im Südlichen Ozean begründet.

List of figures

Chapter 1

- Figure 1.1:** Simplified illustration of the modern and deglacial Southwest Atlantic water mass structure exemplifying unanswered questions.
- Figure 1.2:** Northward-flowing Antarctic Intermediate Water (AAIW) nepheloid layer crossing the Mar del Plata Canyon axis.
- Figure 1.3:** Overview map of the area of investigation at the Argentine continental margin indicating major water masses of the Southwest Atlantic.
- Figure 1.4:** Southwest Atlantic salinity, oxygen and temperature transect along the South American continental margin indicating prevailing water masses.
- Figure 1.5:** Interglacial and glacial Atlantic meridional overturning schematics redrawn from *Howe et al.* [2016].
- Figure 1.6:** Location of all investigated gravity cores at the Argentine continental margin listed in Table 1.1.
- Figure 1.7:** Sediment source areas, i.e. Buenos Aires province, Tandilia, and Ventania, delivering sediments to the Argentine continental margin.
- Figure 1.8:** Overview map showing the Argentine continental margin and its morphological features.
- Figure 1.9:** Location of three major drifts in the Argentine Basin [*Hernandez-Moline et al.*, 2009].
- Figure 1.10:** Morpho-sedimentary map of the Argentine continental margin displaying the contourite depositional system [modified from *Voigt et al.*, 2013].
- Figure 1.11:** Grain size distribution and sortable silt parameter.
- Figure 1.12:** Oceanographic configuration and corresponding clay mineral path ways in the South Atlantic.

Chapter 2

- Figure 2.1:** Location of the investigated marine sediment cores together with the main elements of the deep circulation and bathymetry of the Southwest Atlantic.
- Figure 2.2:** Stratigraphic correlation based on both calibrated AMS ^{14}C ages and down-core Fe/K records.
- Figure 2.3:** Bulk grain size distribution GeoB13861-1, GeoB13823-2 and GeoB13824-1.
- Figure 2.4:** Sortable silt grain-size data of GeoB13861-1, GeoB13823-2 and GeoB13824-1.
- Figure 2.5:** Clay mineralogy of sediment cores GeoB13861-1 (black) and GeoB13823-2 (green).
- Figure 2.6:** Multi-proxy records from the Southwest Atlantic.
- Figure 2.7:** Block diagrams showing the spatial distribution and flow strength of southern component water (SCW) at the distal Mar del Plata (MdP) Canyon and along the Necochea Terrace.
- Figure 2.SI 1:** Examples for classification of homogenous background sediments and turbidite beds.
- Figure 2.SI 2:** Age model reconstruction based on eight AMS ^{14}C ages of GeoB13862-2,

Chapter 3

Figure 3.1: Schematic intermediate and deep water circulation in the Southwest Atlantic from *Stramma and England [1999]*.

Figure 3.2: Morpho-sedimentary map of the NE Argentine continental margin indicating the erosional and depositional features.

Figure 3.3: Mar del Plata Canyon thalweg profile and corresponding morphological features.

Figure 3.4: Simplified core descriptions of GeoB13861-1, GeoB13924-1 and GeoB13823-2 indicating different sedimentary facies

Figure 3.5: Sections of GeoB13861-1 and GeoB13823-2 to characterize turbidites, which are clearly distinguishable from the contourite facies.

Figure 3.6: Mineralogical quantification, integrated K-feldspar/plagioclase intensity ratio, integrated quartz/feldspar intensity ratio and quartz/phyllsilicate ratio based on weight percentage.

Figure 3.7: Time line of total thickness per thousand years (cm/ka) and turbidite recurrence rate in number per thousand years (T/ka).

Figure 3.8: Parasound profiles crossing two potential areas for sediment instabilities (original and interpretation).

Figure 3.9: Grain-size and compositional data of sediments.

Figure 3.10: Simplified turbidite distribution and oceanographic implications for distinct time periods.

Chapter 4

Figure 4.5: Oceanographic setting at the southeastern South American continental margin and modern along-slope salinity profile.

Figure 4.2: Age model of cores GeoB6308 and GeoB6309-1 based on AMS ^{14}C ages.

Figure 4.3: Grain-size dependent records of core GeoB6308.

Figure 4.4: Carbonate content vertical transect covering water depths from ~ 2800 to 4000 m.

Figure 4.5: Terrigenous sortable silt paleocurrent records (SS_{mean}) from the Argentine Margin.

Figure 4.6: Paleocurrent strength proxy records displaying the vertical deepening of the LCDW/AABW interface.

Figure 4.6: Schematic evolution of deep southern component water (SCW) in the Southwest Atlantic.

Figure 4.SI 1: Sortable silt mean values measured with Laser Coulter and Sedigraph

Figure 4.SI 2: Comparison of sortable silt (SS_{mean}) results applying **(a)** the age model of this study and **(b)** an age model disregarding an additional TOC ^{14}C reservoir age of 1035 ± 200

Figure 4.SI 3: Terrigenous grain-size distribution showing percentages of fine sand, silt and clay fractions. Period of increased SS_{mean} values are indicated.

List of tables

Chapter 1

Table 1.1: Sediment gravity cores used in this study.

Chapter 2

Table 2.1: Location and corresponding data of the sediment cores used in this study.

Table 2.2: Accelerator mass spectrometry radiocarbon dates and calibrated ages.

Chapter 3

Table 3.2: Core locations and recovery of sediment cores used in this study.

Table 3.SI 1: Accelerator mass spectrometry radiocarbon dates and calibrated ages used in this study to constrain the age models.

Table 3.SI 2: Classification, base depths, thicknesses, and approximated ages of turbidite beds in sediment cores GeoB13861-1, GeoB13823-2, GeoB13824-1. (Tm – muddy Turbidite, Ts – sandy Turbidite).

Chapter 4

Table 4.3: Location and water depth of the cores investigated in this study^a and previously published^b [Warratz et al., 2017] neighboring cores.

Table 4.4: AMS ¹⁴C ages used to compile the age model of cores GeoB6308 and GeoB6309-1.

Table 4.SI 1: Comparison of reservoir age uncorrected (blue) and corrected (red) TOC AMS ¹⁴C ages used to compile the age model of cores GeoB6308.

List of abbreviations

Antarctic Circumpolar Current	ACC
Antarctic Bottom Water	AABW
Antarctic Intermediate Water	AAIW
Atlantic meridional overturning circulation	AMOC
Deep Western Boundary Current	DWBC
Brazil Current	BC
Brazil-Malvinas confluence zone	BMC
Circumpolar Deep Water	CDW
Contourite depositional System	CDS
Chlorite	ChI
Illite	I
Kaolinite	Kao
Last Glacial Maximum	LGM
Lower Circumpolar Deep Water	LCDW
Malvinas Current	MC
North Atlantic Deep Water	NADW
Northern component water	NCW
Smectite	Sm
Sortable silt mean size	SS _{mean}
Sortable silt weight percentage	SS%
South Atlantic Current	SAC
Southern component water	SCW
Subantarctic Front	SAF
Upper Circumpolar Deep Water	UCDW

Chapter 1

Introduction

1.1 Motivation and scientific objectives

The Southwest Atlantic is a highly dynamic current region and, thus, of significant importance for the global oceanic circulation and heat transfer. Intermediate and deep-ocean currents along the western boundary of the Southwest Atlantic shape the South American continental margin, including the Argentine continental margin. These bottom currents (also termed contour currents) erode, resuspend, transport, and deposit sediments at the seafloor [e. g., *Stow et al.*, 2008]. All Antarctic-sourced water masses affect the continental margin and generate depositional (contourite drifts) and erosional (terraces) features defined as complex Contourite Deposition Systems (CDS, see *section 1.3.3*) [*Hernández-Molina et al.*, 2009; *Preu et al.*, 2013]. Such contourites are an outstanding archive for former climate change and have important implications in the field of paleoceanography. For instance, studying these depositional systems may provide crucial knowledge on the variability of bottom-water circulation and ocean-climate coupling [*Stow et al.*, 2002].

In recent times, Atlantic paleoceanographic reconstructions have mainly focused on changes in the strength of the Atlantic meridional overturning circulation (AMOC), i.e. the ability of the deep ocean to absorb heat and carbon, and its impact on global climate [e.g., *Böhm et al.*, 2015; *Lopes dos Santos et al.*, 2010; *Lynch-Stieglitz et al.*, 2007]. The AMOC transports heat through warm, saline surface currents from the tropics to the polar and subpolar North Atlantic. Here, heat and CO₂ is released to the atmosphere and produces a southward current of cold water in the deep Atlantic. The North Atlantic Deep Water (NADW) travels south at depth until it enters the Antarctic Circumpolar Current (ACC) and upwells. In the Southern Hemisphere, Antarctic Bottom Water (AABW), underling the NADW as a mixture of water masses formed at the Antarctic continental shelf [*Orsi et al.*, 1999], enters the ACC. The AABW mixes with overlying water und leaves the Southern Ocean again as a dense water mass to the north [*Orsi et al.*, 1999]. Spreading away from the Southern Ocean, AABW warms on its way to the North Atlantic. The Antarctic Intermediate Water (AAIW) supplies the upper fraction of the northward flow required to balance the export of NADW, contributing to the upper limb of the AMOC and influencing the inter-hemispheric heat exchange [*Lumpkin and Speer*, 2007].

However, different AMOC modes in the past have been proposed [Boyle and Keigwin, 1987]: During modern times (interglacial mode), deep water formation was active in the North Atlantic and NADW occupied most of the deep Atlantic basin. In the glacial mode, a freshened northern component water (NCW) was most probably located at shallower depth level than today. Below 2,000 m water depth, a mixture with a large fraction of deep southern component water (SCW alias glacial AABW) and a smaller fraction of NCW bathed the Atlantic [Freeman *et al.*, 2016; Howe *et al.*, 2016; Lynch-Stieglitz *et al.*, 2007]. During glacial intervals, the reduced formation of deep water in the North Atlantic, which ventilates the deep ocean and contributes to the formation of SCW in modern times [e.g., Talley, 2013], most likely contributed to the reduction of atmospheric CO₂ due to greater sequestration of CO₂ in the ocean [e.g., Toggweiler, 1999]. Especially the deep SCW exerts a strong control on water mass stratification and storage of CO₂ in the deep ocean [Kuhlbrodt *et al.*, 2007]. These different modes constitute evidence for a link between changes in ocean circulation and changes in surface climate [Bond *et al.*, 1993].

Recent studies have mostly focused on changes in water mass structure and its penetration into the Atlantic across the Last Glacial Maximum (LGM) [Howe *et al.*, 2016; Lund *et al.*, 2011; Lynch-Stieglitz *et al.*, 2007; Rutberg *et al.*, 2000] and the subsequent deglaciation [Boyle and Keigwin, 1987; Came *et al.*, 2008; McManus *et al.*, 2004]. However, current strength variations of Antarctic-sourced water masses have only been investigated by Voigt *et al.* [2016]. They have shown that Holocene millennial-scale changes in the current strength of AAIW are anti-phased with perturbations in NADW circulation. Abruptly increased AAIW advection correlates to periods of reduced NADW strength and vice versa. Despite the significance of the deep SCW for the global circulation system, circulation changes in the Southwest Atlantic, i.e. variations in current strength, remain poorly constrained. This lack of information is usually a result of low carbonate content of deep-sea sediments attributed to strongly corrosive southern-sourced deep water masses [Volbers and Henrich, 2002]. The missing carbonate content in marine sediments limits the obtainment of age control and impedes a reliable assessment of changes in deep SCW circulation [Kuhn and Diekmann, 2002].

The overarching goal of this thesis is to contribute to increase the limited knowledge about deep SCW variations (i.e. strength and position) during the last 20,000 years. A detailed reconstruction of depth-specific variations in mid-depth and deep ocean circulation in the Southwest Atlantic was archived highlighting the last deglacial period and the Holocene. Furthermore, Antarctic-sourced bottom-currents and their impact on along and downslope sedimentary regimes were investigated and their influence on slope stability along the Argentine continental margin was studied.

1.1.1 Deglacial re-organization of the deep water mass structure

The deep SCW and the NADW are the main driving overturning cells of the AMOC [e.g., *Kuhlbrodt et al., 2007; Rahmstorf, 2002*]. As mentioned above, several studies have shown that the Atlantic water mass structure changed since the last glacial, revealing a shoaled and weakened NCW production and a deep SCW expanded at depth [e.g., *Böhm et al., 2015; Came et al., 2008; Freeman et al., 2016; Howe et al., 2016; Lippold et al., 2016; Lynch-Stieglitz et al., 2007; McManus et al., 2004*]. However, deep SCW records in the Southwest Atlantic, revealing detailed variations in the position and vertical shift of the deep SCW relative to the NCW, remain sparse (Figure 1.1a and b). The acquisition of suitable datasets has received considerable interest, due to their importance for unraveling the global oceanic circulation.

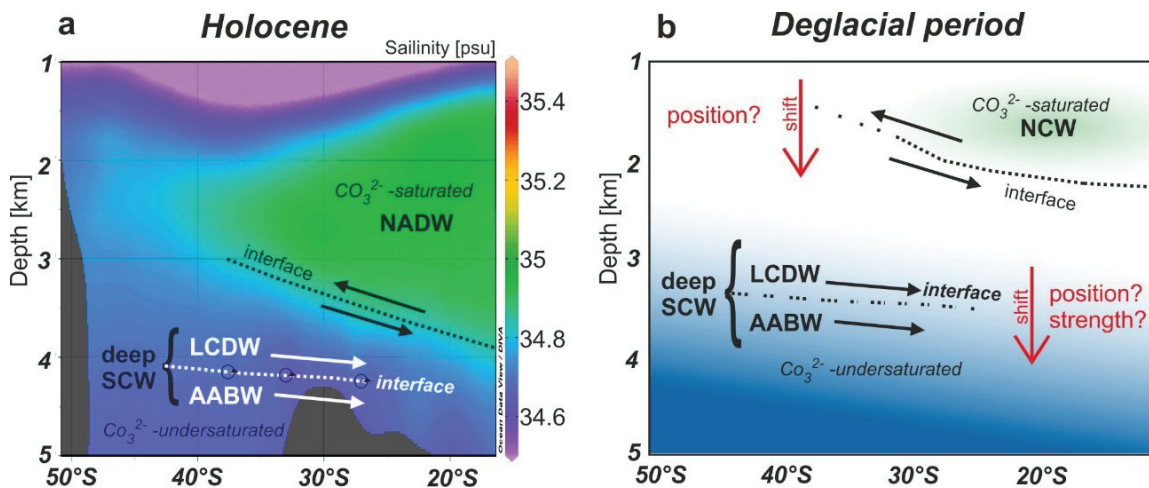


Figure 1.1: (a) Simplified illustration of the modern Southwest Atlantic water mass structure. (b) Schematic representation of the deglacial water mass distribution and penetration in the Southwest Atlantic showing unanswered questions, i.e. the detailed temporal shift and strength of deep SCW (AABW – Antarctic Bottom Water, LCDW – Lower Circumpolar Deep Water, NADW – modern North Atlantic Deep Water, NCW – glacial northern component water, SCW – southern component water comprising the LCDW and AABW; black and white arrows indicate current direction; dashed lines depict the interfaces between water masses).

A combination of different proxies, such as clay minerals (as a transport pathway proxy [*Petschick et al., 1996*]) and carbonate content (a proxy for preservative/corrosive potential of water masses [*Henrich et al., 2003*]) variations through time, may give further insights into the temporal and spatial variability of the NCW and deep SCW. Certain clay mineral distributions representing source regions are supplied by NCW (kaolinite) and SCW (Al-illite or chlorite) (for further information see *section 1.4.2*). Carbonate content varies in different deep water masses according to their differential preservation and corrosivity patterns. Principally, the NCW is a well-ventilated, CO₃²⁻-saturated, and, thus, carbonate preserving water mass. Deep SCW, in contrast, is CO₃²⁻-undersaturated and shows signs of strong carbonate corrosivity [Figure 1.1; *Henrich et al., 2003*]. These characteristic distinctions of water masses allow for a detailed

discrimination of the deglacial NCW deepening at the expense of deep SCW. These distinctions in turn provides further information regarding changes in overall circulation and ventilation of the deep Southwest Atlantic.

1.1.2 Reconstruction of deep southern component water strength

Several studies have reconstructed the geometry and strength of the AMOC since the last glacial, showing that freshwater entering the North Atlantic and Southern Ocean may have significantly affected AMOC by weakening NCW production [e.g., *Lynch-Stieglitz et al.*, 2007; *McManus et al.*, 2004; *Negre et al.*, 2010; *Roberts et al.*, 2010]. However, changes in current strength of deep SCW, apparently affecting deep ocean ventilation, are still poorly constrained (Figure 1.1b). Paleocurrent strength variations can be determined using the sortable silt proxy [i.e., SS_{mean} and $SS_{\%}$; *McCave et al.*, 1995], since low or high SS_{mean} values indicate weak or strong current flow strength (for further information see *section 1.4.1*). The sortable silt proxy allows to study changing water mass strength and/or formation in source areas and varying deep water mass structure in the Southwest Atlantic during the last 20,000 years (Figure 1.1b).

1.1.3 Contourite-turbidite interaction within a blind canyon system

The Southeast American continental margin reveals several submarine canyons incising the continental slope [*Hernández-Molina et al.*, 2009]. Blind canyons, which are strictly confined to the continental slope, are in fact the majority of all submarine canyons [74% of all canyons along the Southeast American margin; *Harris and Whiteway*, 2011]. Despite the remarkable amount of blind canyons incising continental margins all over the world, sedimentary processes and factors triggering their evolution have to be clarified.

Several years ago, two main models were debated for the initiation of blind canyons: the upslope erosion model and the downslope erosion model [*Pratson et al.*, 1994; *Twichell and Roberts*, 1982]. *Pratson and Coakley* [1996] defined the upslope erosion model explaining the origin of numerous blind canyons starting their evolution by local, retrogressive slope failures and mass wasting at the most downslope position. These processes cause further upslope failures. *Harris and Whiteway* [2011] also considered slope failures being responsible for blind canyon evolution. However, *Pratson et al.* [1994] added a downslope erosion model, where existing downslope conduits might be (re-)used by turbidity currents forming present-day canyon morphology. In this downslope erosion model, retrogressive failures act as a process widening the present canyon morphology. Prominent examples for blind canyon formation related to both processes are the continental slope off New Jersey [*Pratson and Coakley*, 1996] or on the flanks of the Canary Islands [*Krastel et al.*, 2001]. The most prominent blind canyon at the

Argentine continental margin is the Mar del Plata Canyon. The modern canyon head originates at the Ewing Terrace in a mid-slope position and reveals no buried upslope continuation. Based on these canyon initiation models, *Krastel et al.* [2011] suggested the upslope erosion model to be responsible for the Mar del Plata canyon formation, but further support is lacking.

The Argentine continental margin is shaped by the incursion of strong currents creating erosional (terraces) and depositional (contourite drifts) features [*Hernández-Molina et al.*, 2009]. The Mar del Plata intersects this CDS and the canyon head interacts with the northward-flowing AAW nepheloid layer (Figure 1.2) flowing along the Ewing Terrace [*Preu et al.*, 2013]. The canyon decreases the transport capacity of AAIW and, thus, changes the contourite deposition around the canyon head, while releasing the suspended material into the canyon [*Voigt et al.*, 2013].

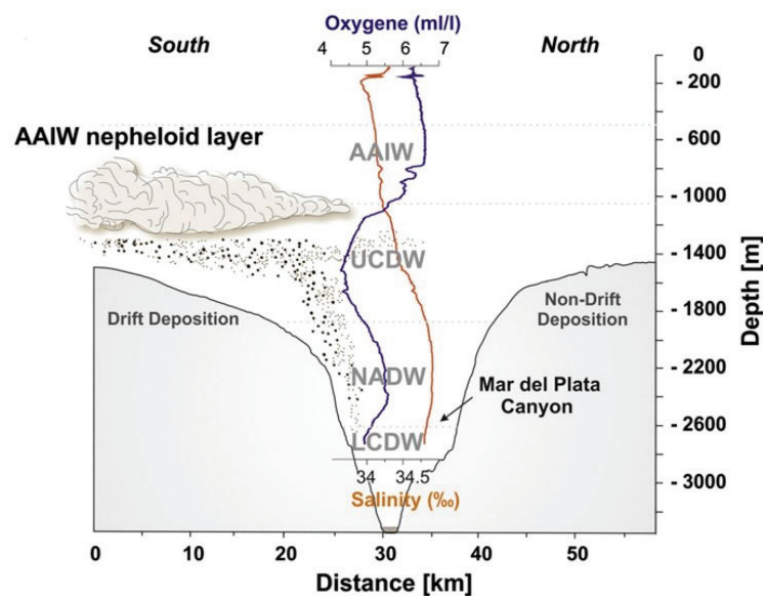


Figure 1.2: Northward-flowing Antarctic Intermediate Water (AAIW) nepheloid layer crossing the Mar del Plata Canyon axis and releasing suspended material into the canyon [Figure from *Voigt et al.*, 2013].

In contrast to the upper Mar del Plata Canyon, the depositional pattern in the distal canyon area, located on the Necochea Terrace on the deepest slope, remains poorly constrained. This area reveals further information on contourite-turbidite interactions driven by internal processes within the CDS, in particular, by variations in deep SCW flowing along the Necochea Terrace. Further comparative stratigraphic, mineralogical and sedimentological investigations of turbidite beds and Ewing terrace contourites offer crucial insights into the contourite-turbidite interaction giving information on timing, source areas and trigger mechanisms. In addition, canyon morphology investigations provide further information to decode source and trigger mechanisms of these down-slope sediment flows.

1.1.4 Influence of Antarctic Intermediate Water on slope instabilities

Voigt et al. [2013] showed that the AAIW nepheloid layer along the Ewing Terrace clearly affects the sedimentation within the upper part of the Mar del Plata Canyon (Figure 1.2). The deposits inside the canyon were similar in composition and grain size to the drift deposits on the Ewing Terrace, thus, indicating a current-controlled sedimentation in the canyon. The dominance of the sortable silt fraction over other particles in the size spectrum indicated that sedimentation responds to current-controlled hydrodynamic processes [*McCave et al.*, 1995]. Sortable silt reconstructions by *Voigt et al.* [2016] support abrupt variations in AMOC with enhanced (reduced) northward advection of AAIW during periods of reduced (enhanced) North Atlantic Deep Water (NADW) circulation during the Holocene.

The Holocene AAIW variability raises the question, whether the changes were restricted to the AAIW level or whether they also induced general changes in deeper circulation levels. Assuming that turbidity currents are the result of AAIW nepheloid layer sedimentation [*Voigt et al.*, 2013], extensive mapping of turbidite beds in the vicinity of the Mar del Plata Canyon and their correlation to distinct periods of gravity-driven transports, would provide evidence on variations in AAIW position in the water column and/or current strength.

Up to date, the deglacial AAIW circulation and strength is still under debate: *Pahnke et al.* [2008] presented a neodymium isotopic variations (as a tracer for water mass mixing) indicating enhanced northward advection of AAIW during periods of reduced AMOC during the last deglaciation. These events were interpreted to coincide with increased AAIW formation and warming in the southwest Pacific. This hypothesis was supported by *Hendry et al.* [2012], who have investigated intermediate depth silicic acid concentrations. During the Last Glacial Maximum, these concentrations were similar to Holocene values. Nevertheless, the authors noticed high silicic acid pulses during abrupt changes in ocean and atmospheric circulation also indicating changes in intermediate water formation. In contrast to these two studies, *Huang et al.* [2014] applied foraminifera-based neodymium isotopic composition and proposed similar glacial and Holocene AAIW contribution in the Atlantic, but recorded a pronounced decrease in AAIW fraction during North Atlantic cold events. Compiling both approaches, AAIW fraction and strength during the last deglaciation remains controversial. However, the Mar del Plata Canyon is controlled by the AAWI nepheloid layer sediment delivery to the upper canyon [e.g., *Voigt et al.*, 2013]. Such contouritic sediments respond to glacial/interglacial variations in AAIW strength and position, which would effectively change sediment delivery to the canyon head, affecting slope stability. Thus, these sediments are another approach to investigate AAIW circulation.

1.2 Oceanic circulation – state of the art

1.2.1 Modern South Atlantic circulation

The study area at the Argentine continental margin encompasses the Southwest Atlantic from 35° - 40°S and is bathymetrically restricted by the Argentine Basin in the South and the Brazil Basin in the North (Figure 1.3). An essential characteristic of this margin is the interaction of highly active oceanographic processes with the seafloor, which is regarded as one of the world's most dynamic hydrographic regimes [e.g., *Chelton et al.*, 1990].

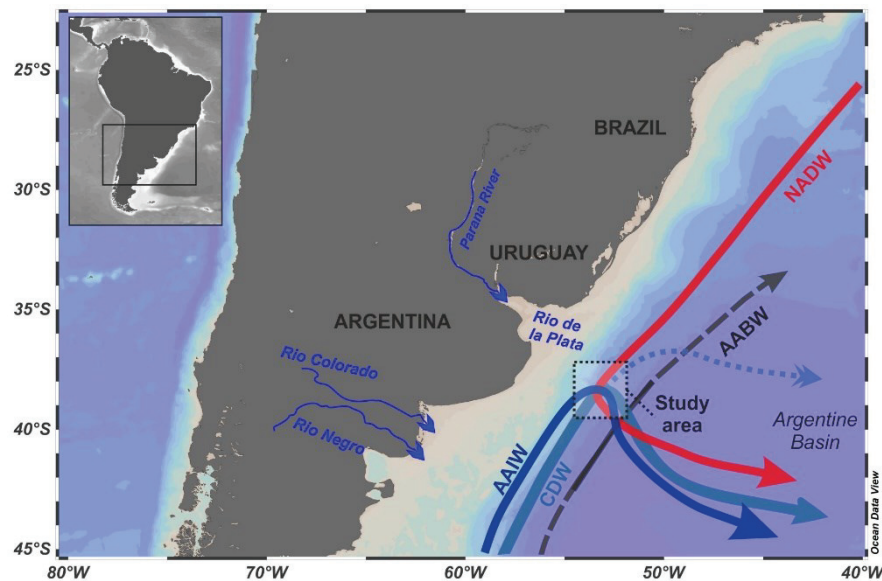


Figure 1.3: Overview map of the area of investigation at the Argentine continental margin indicating major water masses of the Southwest Atlantic: AABW – Antarctic Bottom Water, AAIW – Antarctic Intermediate Water, CDW – Circumpolar Deep Water, NADW – North Atlantic Deep Water [Figure created with Ocean Data View 4.7.2, *Schlitzer*, 2015].

Below, a detailed description of the paleoceanographic setting and their effect on carbonate and organic carbon distribution in surface sediments is provided:

The upper-level circulation is dominated by the southward-flowing Brazil Current (BC) and the northward-flowing Malvinas Current (MC), together with the confluence of both currents [BMC, *Peterson and Stramma*, 1991; *Stramma and England*, 1999]. The warm, saline and nutrient-depleted BC denotes the western portion of the subtropical gyre and originates at 10°S. The cold, fresh and nutrient-rich MC encounters at 38°S (Figure 1.4.a and b) as a branch of the Antarctic Circumpolar Current (AAC) east of the Drake Passage [*Peterson et al.*, 1996]. The modern migration of the BMC ranges between 32° and 40°S [*Olson et al.*, 1988]. After being in contact, the BC and MC turn southeastward flowing offshore to form the South Atlantic Current [SAC, *Peterson and Stramma*, 1991]. *Frenz et al.* [2003] presented reduced carbonate content in surface sediments offshore La Plata mouth. The reduction indicates terrigenous dilution in

response to high river discharge and/or enhanced supralysoclineal dissolution of carbonate due to high organic-carbon flux rates. Such flux rates are associated with the high-productivity at the BMC zone. Hydrogen-enriched organic-matter of mixed marine and terrigenous origin, stimulated by high mean freshwater discharge from the La Plata River, decrease from shallow sites off La Plata to deeper marine settings. The organic matter distribution also indicates an enhanced carbonate dissolution in relation to remineralization of settling reactive organic matter [Frenz *et al.*, 2003].

The intermediate circulation south of the confluence zone is forced by the northward-flowing AAIW (500 – 1000 m) and two Circumpolar Deep Water (CDW, 1000 – 4000 m water depth) fractions [Stramma and England, 1999]: the Lower Circumpolar Deep Water (LCDW) and the Upper Circumpolar Deep Water (UCDW, Figure 1.3). Interfaces between all water masses can be determined by density changes (Figure 1.4a) displaying a deepening to the North at basin scale [Arhan *et al.*, 2002a; Piola and Matano, 2001]. The UCDW is characterized by relatively low oxygen and high nutrient concentrations and originates in the Indian and Pacific Oceans [Callahan, 1972]. The LCDW is the highly saline component of the CDW, which occupies most of the deep ACC entering the South Atlantic through the Drake Passage [Orsi *et al.*, 1995] and is derived from modified NADW [Dinniman *et al.*, 2011; Whitworth and Nowlin, 1987].

In the South Atlantic, the AAIW originates from surface regions of the circumpolar layer, especially in the northern Drake Passage and the Falkland Current loop [Arhan *et al.*, 2002b]. Recognized by subsurface oxygen maximum and salinity minimum north of about 50°S (Figure 1.4) [Stramma and England, 1999], the oxygen maximum becomes absent north of 15°S. The spreading of the AAIW from the South Atlantic to the North Atlantic can be identified by a salinity minimum near the equator.

North of the BMZ zone, the high-oxygen NADW forms (Figure 1.4b) and is transported by the Deep Western Boundary Current (DWBC) from the Northern Hemisphere into the South Atlantic [Stramma and England, 1999]. The depth and thickness of the NADW decreases from the equator (1200 to 3900 m) to the BMC zone (1700 to 3000 m, Figure 1.4). The salinity maximum of the relatively warm NADW lies near 1600 m depth near the equator and deepens to 2500 m at 25°S (Figure 1.4a). The NADW travels South as far as 48°S [Frenz *et al.*, 2003], where it turns away from the continent towards the east. A main chemical property of the southward-flowing NADW is its oversaturation with respect to CO_3^{2-} [$> 110 \mu\text{mol kg}^{-1}$; Dittert *et al.*, 1999] enhancing carbonate preservation.

The NADW renews part of the CDW in the South Atlantic and is a major source of heat and salt [Gordon, 1971; Jacobs *et al.*, 1985]. The upwelling CDW causes basal melting of ice shelves and

affects most of the Southern Ocean water mass formation [Jacobs *et al.*, 1985]. Heat or salt delivery changes CDW geochemical signature and, thus, affect the properties of newly formed water masses in the Southern Ocean [Jacobs *et al.*, 1985].

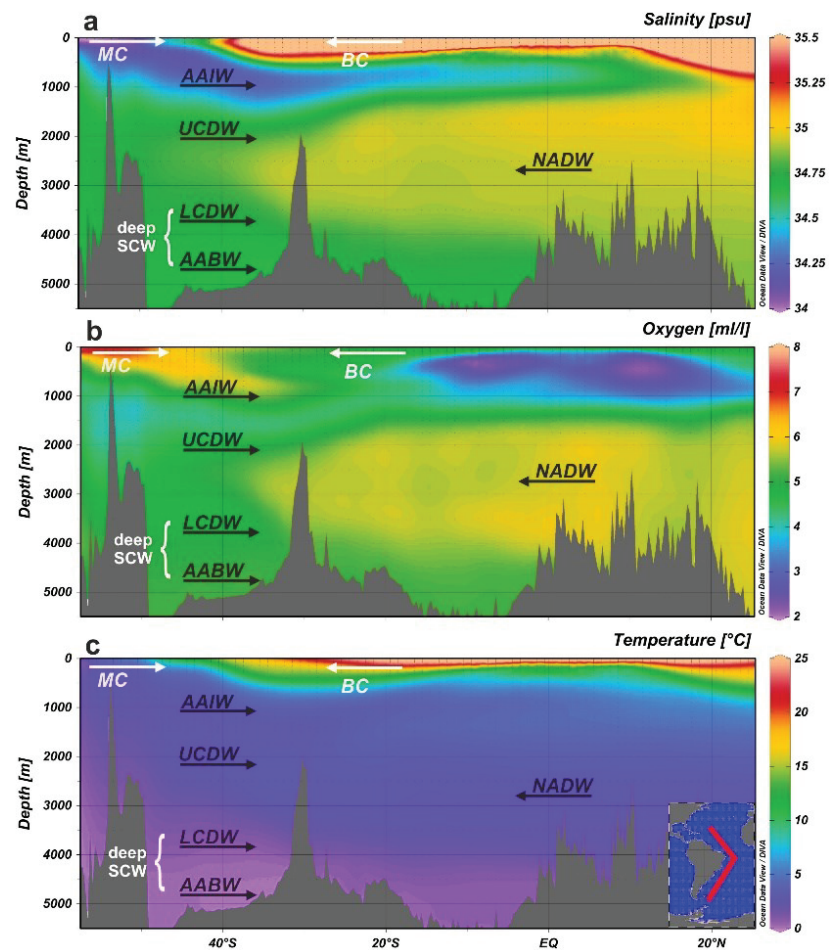


Figure 1.4: Southwest Atlantic (a) salinity, (b) oxygen and (c) temperature transect along the South American continental margin indicating prevailing water masses (figure created using Ocean Data View, WOA_09; Diva-gridded; Schlitzer [2015]; AABW – Antarctic Bottom Water, AAIW – Antarctic Intermediate Water, BC – Brazil Current, LCDW – Lower Circumpolar Water, MC – Malvinas Current, NADW – North Atlantic Deep Water, SCW – southern component water, UCDW – Upper Circumpolar Deep Water).

The low oxygen AABW (> 4000 m water depth) represents the deepest part of the circulation system (Figure 1.4). The AABW is partially trapped in the Argentine Basin, generating a large cyclonic gyre in 3500 – 4000 m water depth [Arhan *et al.*, 2002b; Hernández-Molina *et al.*, 2008b]. The upper AABW originates in the AAC and consists of either old LCDW or of Weddell Sea Deep Water (WSDW) [Orsi *et al.*, 1999]. The AABW enters the basin from the South before turning to the West, passing the Malvinas/Falkland Escarpment, until heading north along the Argentine continental slope. As a western boundary current, the AABW flows northward entering the Brazil Basin through the Vema Channel [e.g., Faugères and Stow, 1993; Hernández-Molina *et al.*, 2010].

All these intermediate and deep water masses of southern origin (AAIW, CDW, and AABW) display under-saturation of carbonate ions [$\text{CO}_3^{2-} < 90 \mu\text{mol kg}^{-1}$; *Frenz et al.*, 2003]. Hence, dissolution of carbonate is increased within these water masses. *Frenz et al.* [2003] showed that decreasing carbonate content in a water depth level above 1,500 m records the transition between NADW to LCDW and AAIW. The main reasons are: (i) low carbonate production in cold surface waters, (ii) strong dilution by high terrigenous river discharge, and (iii) increased carbonate corrosivity [*Frenz et al.*, 2003]. Below 4,000 m water depth, carbonate dissolution leads to a relative enrichment of organic carbon. Organic carbon preservation in the AABW is supported by low oxidation rates of organic matter due to the low oxygen AABW [*Frenz et al.*, 2003]. *Frenz et al.* [2003] further discussed that the NADW is represented in high carbonate content and very low organic carbon concentrations in surface sediments. High oxygen concentrations of this water mass result in a low preservation potential of organic matter.

1.2.2 Glacial deep South Atlantic circulation

The glacial South Atlantic circulation has received renewed scientific attention since the late 1980s. Comprehensive studies have shown that the glacial intermediate- and deep-water circulation was significantly different from the modern distribution (Figure 1.5) [e.g., *Boyle and Keigwin*, 1982; *Curry and Lohmann*, 1983].

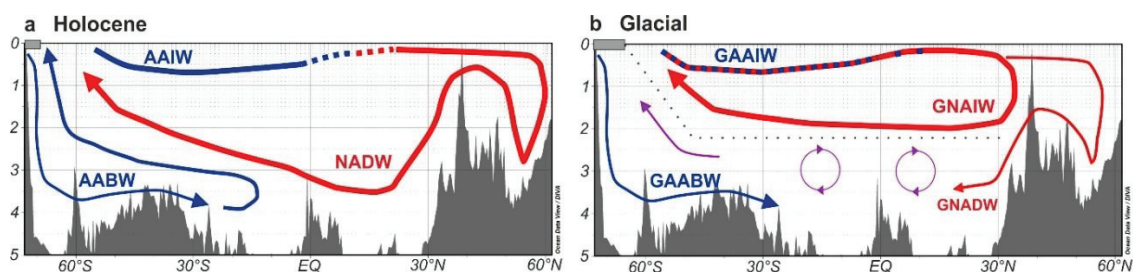


Figure 1.5: (a) Interglacial and (b) glacial Atlantic meridional overturning schematics in an Atlantic N-S transect redrawn from *Howe et al.* [2016] exemplifying the Antarctic Bottom Water – AABW, Antarctic Intermediate Water – AAIW, Glacial North Atlantic Intermediate Water - GNAIW, North Atlantic Deep Water – NADW, and their glacial counterparts. The glacial water mass distribution (b) displays a deep Atlantic Ocean occupied by an expanded glacial AABW (GAABW) with additional minor proportions of glacial NADW (GNADW) (Figure partly created using Ocean Data View [Schlitzer, 2015]).

A study by *Curry and Oppo* [2005] suggests that the glacial circulation comprises three water masses below the subtropical gyre: The water mass end-member compositions were very different and mixing among water masses resulted in very strong meridional and bathymetric gradients in the western Atlantic. (i) An intermediate southern component water mass (glacial AAIW) was present at 1000 m water depth (Figure 1.5b). This water mass was analog to modern AAIW, but formed without strong sea-air enrichment in $\delta^{13}\text{C}$ [*Curry and Oppo*, 2005]. (ii) Another water mass centered at 1500 m represented the southward penetration of Glacial North Atlantic

Intermediate Water (GNAIW, Figure 1.5b) with a $\delta^{13}\text{C}$ composition of 1.5 ‰ [Curry and Oppo, 2005]. Several authors supported this continued but shoaled GNAIW southward flow during the LGM [e.g., Lynch-Stieglitz et al., 2007] without a major reduction in the overturning cell. A strong bathymetric gradient in (very low) $\delta^{13}\text{C}$ marks the presence of the mixing zone between GNAIW and (iii) the deep SCW below 2000 m water depth [Curry and Oppo, 2005]. The deep SCW expansion was reinforced by several studies [Freeman et al., 2016; Lippold et al., 2016]. Others, in contrast, suggest that this glacial SCW expansion was probably not as extensive (Figure 1.5b) as previously proposed containing minor proportions of glacial NADW [Howe et al., 2016]. Weaver et al. [2003] argued that the dense water formation is strongly affected by meltwater discharge and that it may have led to the strengthening of ocean circulation in the other hemisphere.

1.3 Study area

The study area is located in the Southwest Atlantic at the northern sector of the Argentine continental margin between 35 and 40°S (Figures 1.1 and 1.6). A huge number of gravity cores were collected during several research cruises to Argentina and Uruguay, i.e. M78/3 [Krstel et al., 2012], M29/1 [Segl et al., 1994], M49/1 [Spieß et al., 2003], and M46/3 [Bleil et al., 2001].

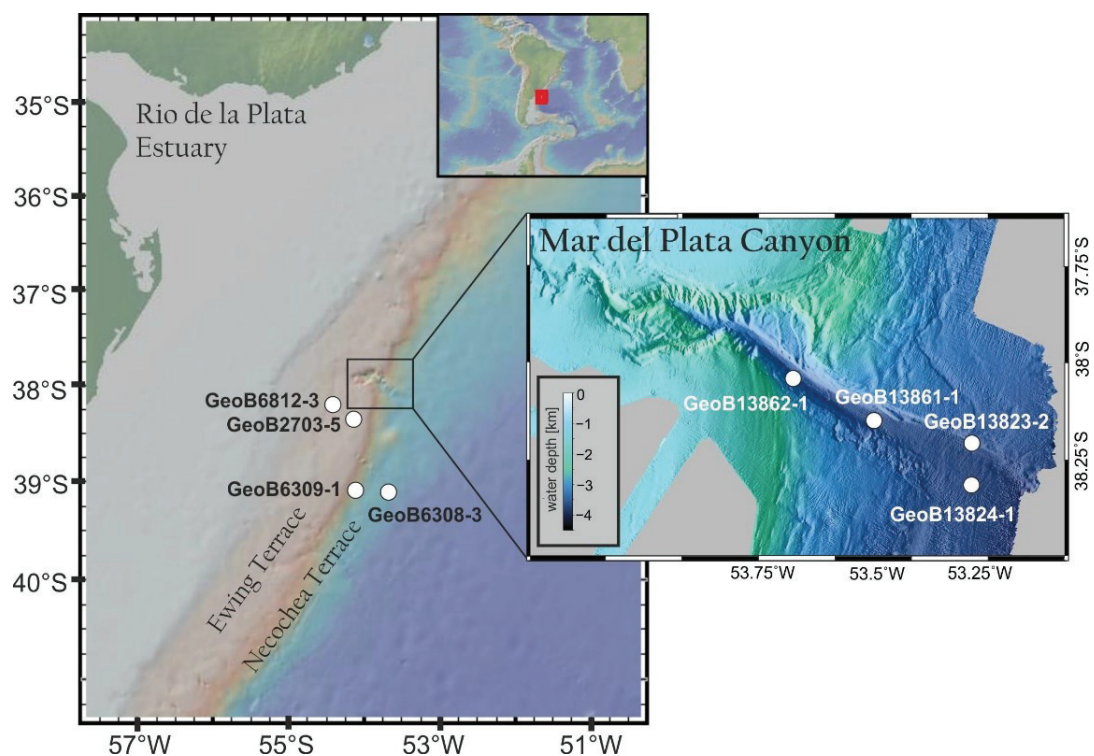


Figure 1.6: Location of all investigated gravity cores at the Argentine continental margin listed in Table 1.1 (map created using www.geomapapp.org and GMRT data [Ryan et al., 2009]).

Table 1.1: Sediment gravity cores used in this study.

Location	Cruise	Core	Latitude	Longitude	Water depth (m)	Recovery (cm)
Mar del Plata Canyon and Necochea Terrace	M78/3a	GeoB13823-2	38°08.68'S	53°20.6'W	3780	938
	M78/3a	GeoB13824-1	38°13'14'S	53°21.29'W	3821	1066
	M78/3b	GeoB13861-1	38°09.18'S	53°60.9'W	3715	668
	M78/3b	GeoB13862-1	38°01.85'S	53°74.50'W	3588	1016
Ewing Terrace	M29/1	GeoB2703-5	38°30.60'S	54°12.10'W	1189	467
	M49/1	GeoB6812-3	38°18.20'S	54°47.70'W	734	186
Southern Necochea Terrace and Argentine slope	M46/3	GeoB6308-3	39°18.1'S	53°57.9'W	3620	793
	M46/3	GeoB6309-1	39°10.0'S	54°08.7'W	2867	862

GeoB13861-1, GeoB13823-2, and GeoB1384-1 were recovered within the distal Mar del Plata Canyon and on the Necochea Terrace (Figure 1.6). The deep core sites within Necochea drift at > 3600 m water depth were used to investigate the deglacial deep Southwest Atlantic circulation. GeoB13862-1 contained nine radiocarbon ages [Voigt *et al.*, 2013] covering the Holocene period. These AMS ¹⁴C ages of GeoB13862-1 and further AMS ¹⁴C ages of GeoB13861-1 and GeoB13823-2 were used to compile the age models. X-ray fluorescence Fe/K downcore records were used for core-to-core age model tuning (for further information see *Chapter 2, Age models*). The contouritic background sediments of these cores were used to reconstruct deep SCW current strength variations during the last 20,000 (*sections 1.1.1 and 1.1.2*).

The sortable silt and carbonate records of these cores were compared to GeoB6308-1 (Figure 1.6), which is located on the Necochea Terrace south of the canyon. All these sortable silt records were used to present deep SCW current strength variations by detecting the deglacial deepening of the highly energetic LCDW/AABW interface during the last 20,000 years.

The three cores GeoB13861-1, GeoB13823-2, and GeoB13824-1 (Figure 1.6) were also used to investigate the turbidity current activity and contourite-turbidite interaction within the blind Mar del Plata Canyon. In addition, two other cores located on the Ewing Terrace (GeoB2703-5 and GeoB6812-3; Figure 1.6) were studied to estimate sediment provenience of turbidity currents by comparing sediment texture and mineralogical composition (*sections 1.1.3 and 1.1.4*).

1.3.1 Sediment provenances of eastern South America – from source to sink

Continental margins represent the major sink for terrigenous particles along the source-to-sink pathway from continent to the deep sea. The coastal areas of southeast South America play a major role in the sediment supply to the Argentine continental margin.

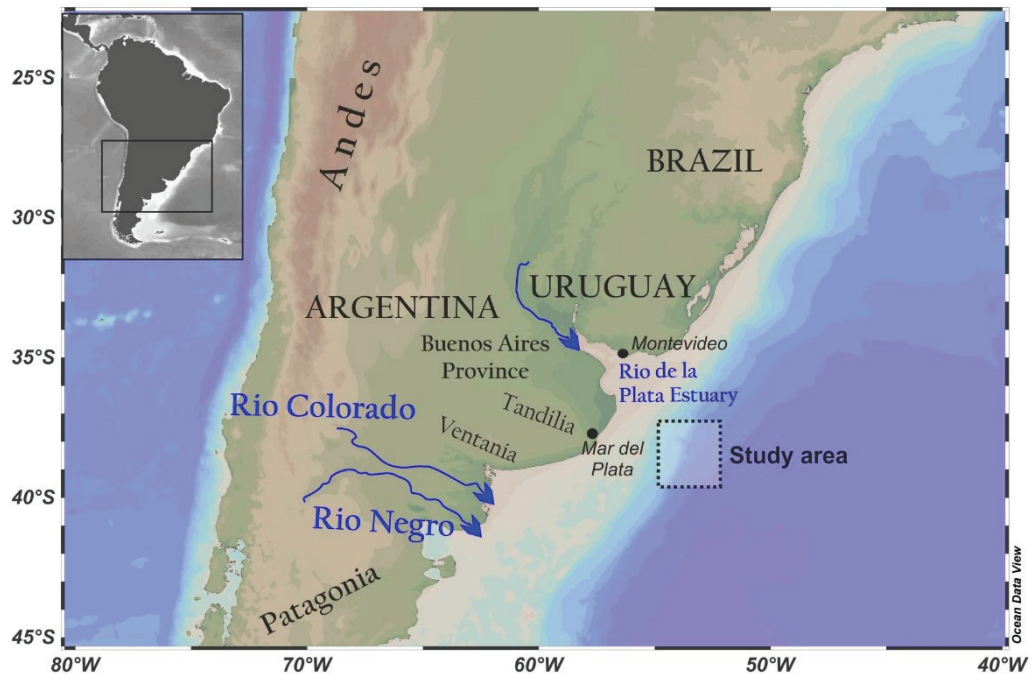


Figure 1.7: Sediment source areas, i.e. Buenos Aires province, Tandilia, and Ventania, delivering sediments to the Argentine continental margin (Figure created with Ocean Data View [Schlitzer, 2015]).

The Argentine continental margin is bounded by the Buenos Aires Province (“Pampas”), interrupted by the Tandilia and Ventania ranges, and influenced by the Rio de la Plata (Figure 1.7). The northern Pampa is located between Tandilia Range and the Rio de la Plata axis, whereas the southern Pampa is located between Ventania and Tandilia [Bozzano *et al.*, 2011]. The Tandilia range reaches the coast at 38°S (Figure 1.7) and covers an igneous metamorphic basement, which is overlain by Precambrian and early Paleozoic sedimentary cover with common quartz and quartz-arkosic arenites, dolostones, shales and conglomerates [Dalla Salda *et al.*, 2006]. The Ventania Range (Figure 1.7), in contrast, consists of igneous metamorphic basement and a Paleozoic cover composed of quartzites, siltstones, sandstones and conglomerates [e.g., Kilmurray, 1975]. Thus, the Tandilia and Ventania ranges deliver major amounts of feldspar, quartz, and dolomite.

The Pampas are covered by late Pleistocene to Holocene loess deposits [Zárate, 2003], which are volcanoclastic with a Patagonian/southern Andean source in the southern area, and from north-western areas of the Chilean Altiplano and Paraná Basalt province in the northern area

[Smith *et al.*, 2003]. Thus, coastal fringe sediments are characterized by major amounts of quartz, feldspar and lithic fragments.

Especially the shelf from northern Patagonia to the Pampa region (Figure 1.7) reveals volcanic-pyroclastic elements (“Pampean-Patagonian suite”) and is covered by fine to medium siliciclastic sands. Detrital sediment supply to the continental slope is primarily transported by rivers and wind [Gaiero *et al.*, 2004; Gaiero *et al.*, 2003] and consists mainly of quartz, pyroxene, feldspars (mainly plagioclase), and olivine.

The fluvial sedimentary load is delivered by three major rivers, i.e. the Rio de la Plata, Rio Colorado and Rio Negro. The Rio Negro and Rio Colorado are located in northern Patagonia and flow from the Andean Cordillera to the South Atlantic Ocean. Since both river drainage areas are characterized by volcanic rocks and late Tertiary volcanoclastic deposits, their sediment load to the ocean consist of major amounts of volcanic minerals [Blasi and Manassero, 1990], which include pyroxene, olivine and plagioclase.

The Rio de la Plata is the second largest fluvial system in South America (Figure 1.7) and marks the transition zone between the Brazilian shield and the “Pampas” region [Burone *et al.*, 2013]. The major sediment source has a modern drainage catchment area of 35,000 km², annual freshwater discharge of 22,000 m³ s⁻¹ and sediment supply of 80x10⁶ t year⁻¹ [Giberto *et al.*, 2004]. This river supplies silts and silty clays to the shelf, although fluvial sediments, such as quartz, feldspars, and lithic fragments are first trapped inside the La Plata Estuary. Generally, the suspension cloud of the river follows the paleo-topography of the Rio de la Plata, spreading freshwater over the entire continental shelf off the Plata Estuary [Piola *et al.*, 2005]. Recent studies have shown that the low-salinity tongue is transported to the northeast up to 27°S due to austral winter southwesterly wind regime [de Mahiques *et al.*, 2004; Piola *et al.*, 2005]. Also during the last glacial, the La Plata River sediment load is deflected the North over the exposed continental shelf [Ewing and Lonardi, 1971]. Moreover, Chiessi [2008] supported, that the sedimentary load of the La Plata River was directly delivered to the North and suggested a transport towards the Rio Grande Cone, located within the western Argentine Basin north of the Mar del Plata Canyon.

1.3.2 Morphology of the Argentine continental margin

The Argentine continental margin is a volcanic passive margin located between 35° and 49°S. From North to South, the continental margin trends south-west until 45° S, where it changes its orientation to east south-east (Figure 1.8a). Except of the large-scale tectonic evolution since Late Jurassic-Cretaceous times, gravitational mass and turbidity processes are mainly affecting

the continental margin [Franke *et al.*, 2007; Hinz *et al.*, 1999]. The passive continental margin developed by the Eocene-Mid Miocene, when Antarctic water-masses began to actively influence the area [Hernández-Molina *et al.*, 2010]. At least since this time, along-slope sedimentary processes are the main controlling factors [Ewing and Lonardi, 1971; Hernández-Molina *et al.*, 2009]. Since Late Pliocene, the morpho-sedimentary evolution of the slope raised present characteristics [Ewing and Lonardi, 1971] revealing the following main features:

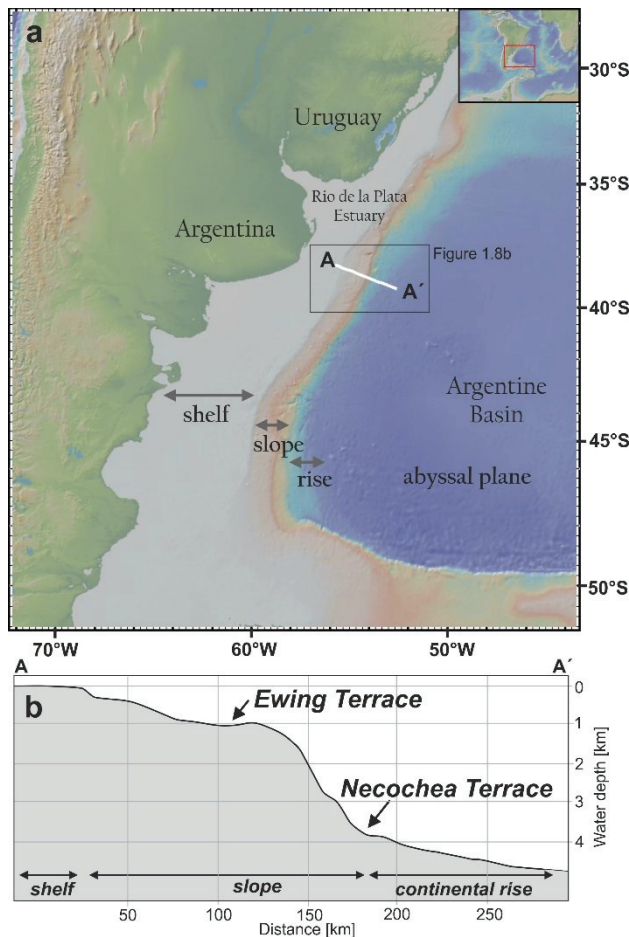


Figure 1.8: (a) Overview map showing the Argentine continental margin and its morphological features (shelf, slope, rise, abyssal plane). (b) Profile A-A' exported from GMRT Grid Version 3.4, [Ryan *et al.*, 2009] (Figure created using www.geomapp.org).

(I) The modern continental shelf is located on the South American continental crust, whereas the lower slope and rise lie on the transition of continental and oceanic crust [Hernández-Molina *et al.*, 2010]. The shelf width varies from North to South [Hinz *et al.*, 1999]. The narrowest section of the shelf is located near Mar del Plata and widens to the South (Figure 1.8b). At the coastline, the funnel-shaped la Plata Estuary is developed [Lantzsch *et al.*, 2014]. The La Plata paleo-valley located at the inner continental shelf off the Uruguayan coast reveals an elongated seafloor depression [Cavallotto *et al.*, 2004; Lantzsch *et al.*, 2014]. The outer shelf is characterized by a morphological step in 80 m water depth. This step was suggested to be related to a sea-level lowstand delta system [e.g., Preu *et al.*, 2012; Urien and Ewing, 1974].

(II) Width of the Argentine slope varies between 50 km to 300 km. It has an average slope gradient of 2° [e.g., Ewing and Lonardi, 1971] and is crossed by various submarine canyons, i.e., the Mar del Plata Canyon [Hernández-Molina *et al.*, 2010]. At water depths of 120 to 3,500 m, the slope displays significant changes in gradients (Figure 1.8b). The upper slope (120-500 m) is steep (1:33) and exhibits an abrupt shelf-upper slope transition. The middle slope (500-1,300 m) has a more gentle and less uniform gradient (1:120-1:160), whereas the lower slope (1,300-

3,500 m) is again steeper (1:20) and gradually merges into the continental rise [Figure 1.8b, *Hernández-Molina et al.*, 2010]. A particular feature of the Argentine continental slope are morphological terraces (Figure 1.8b), i.e., the Ewing Terrace (in 1,000 m) and the Necochea Terrace (in 3,500 m) [*Hernández-Molina et al.*, 2009; *Preu et al.*, 2013].

(III) *Hernández-Molina et al.* [2010] described the continental rise as being located in the central and northern sector of the margin, covering a water depth range of 3,200 to 3,500 m with a width of 250 km (Figure 1.8b). (IV) The transition to the abyssal plane (Argentine basin) follows at a water depth of 5,000 m with a clear North-East trend and makes up an area of 200,000 km².

The Argentine abyssal plain contains three major contourite drifts (Figure 1.9): the Zapiola, Argyro and Ewing drifts - generated by the deep and southern-sourced AABW [*Ewing and Lonardi*, 1971; *Hernández-Molina et al.*, 2008a; *Hernández-Molina et al.*, 2010].

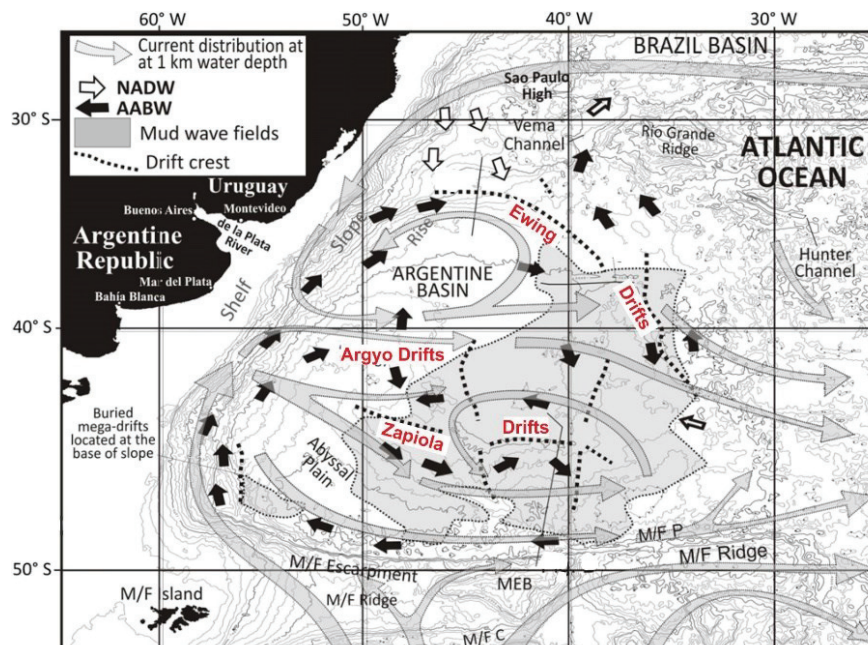


Figure 1.9: Location of three major drifts in the Argentine Basin, i.e. Argyro, Ewing, and Zapiola drift, and corresponding current directions forcing their distribution [Figure modified from *Hernández-Molina et al.*, 2010]

The Zapiola drift (i) is centered in the southern part of the basin with a diameter of 350 km, a maximum thickness of 3,000 m and curvy-linear crests [Figure 1.9; *Ewing and Lonardi*, 1971; *Hernández-Molina et al.*, 2010]. Here, a steady southward flow with varying flow intensities across the drift was described as the western part of the cyclonic gyre centered around the Zapiola Drift, which is responsible for sediment wave evolution [*von Lom-Keil et al.*, 2002]. The Argyro drift (ii) has been interpreted as a series of smaller drifts within central part of the Argentine Basin [Figure 1.9; *Hernández-Molina et al.*, 2010]. The Ewing drift (iii) has an east-southeast extension from the South American rise into the abyssal plain toward the Zapiola drift

[Hernández-Molina *et al.*, 2010]. The crest line is arc shaped and a second parallel crest lies eastward. Both crests are consistent with the general pathways expected for a return flow of abyssal water [Flood and Shor, 1988].

1.3.3 The Argentine Contourite Depositional System

The universally excepted term “contourite” applies to sediments which are deposited or reworked by bottom currents driven by thermohaline circulation, deep-sea tidal forces or internal waves [Rebesco, 2014; Stow *et al.*, 2002]. These bottom or contour currents operate as part of the normal thermohaline circulation [Stow *et al.*, 2008]. Such currents continuously affect sedimentation along continental margins and are often long-lived through geologic time and [Hernández-Molina *et al.*, 2008a; Hernández-Molina *et al.*, 2009; Stow *et al.*, 2008]. Subsequent contouritic sediments are suggested to be fairly continuous and reveal temporal records of relatively high resolution. Contouritic accumulation rates can be much higher than those in adjacent pelagic sequences [Rebesco, 2014], thus, yielding valuable information on the variability of ocean circulation patterns and current velocities.

Contourite deposition is a complex process and involves multiphase entrainment, long-distance transport for long time periods and interaction among depositional processes [McCave, 2008; Stow *et al.*, 2002; Stow and Faugères, 2008]. Erosive features, such as contourite terraces, may develop, where bottom currents are strong enough to erode the continental margin. Depositional features, such as contourite drifts, develop outside of the high velocity zone (Figure 1.10). A compilation of various contourite drifts and erosive features are summarized as a CDS [Hernández-Molina *et al.*, 2003; Hernández-Molina *et al.*, 2008a]. The CDS offshore Argentina was described by Hernández-Molina *et al.* [2009] and Preu *et al.* [2013]. Both favor a current-controlled processes related to Antarctic sourced water masses (Figure 1.10) over tectonic processes as a major governing factor for terrace formation.

Seismo-acoustic and hydro-acoustic morpho-sedimentary analyses of the Argentine continental margin allowed for the characterization of erosive and depositional features. Preu *et al.* [2013] described three major terraces are located in an upper slope (La Plata Terrace), middle slope (Ewing Terrace) and lower slope position (Necochea Terrace):

(I) The uppermost La Plata Terrace is located in 500-600 m water depth and deepens towards the North. This terrace is forced by the interface of surface waters and the AAIW [Preu *et al.*, 2013] indicating energetic current pattern driven by major vertical density gradients [Reid *et al.*, 1977]. Water-mass interfaces characterize pycnoclines affected by several baroclinic activities and represent zones dominated by turbulent and intense bottom currents (e.g. internal tides)

[Arhan *et al.*, 2002a; Cacchione *et al.*, 2002]. Hence, *Preu et al.* [2013] proposed a dynamic sedimentary environment of the slope above the La Plata Terrace indicating erosion favored by general turbulent bottom currents conditions. Lower slope angles on the terrace, in contrast, imply more tabular flow conditions with lower flow velocities favoring uniform sedimentation along the La Plata contourite terrace.

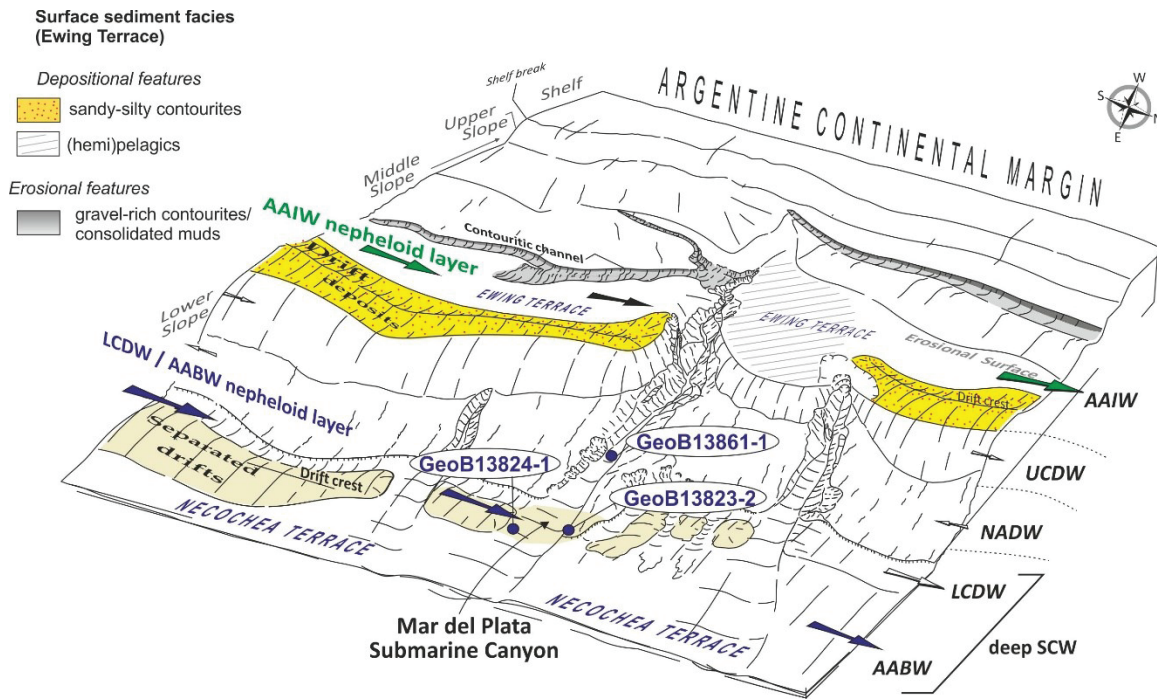


Figure 1.10: Morpho-sedimentary map of the Argentine continental margin displaying the contourite depositional system (CDS) with erosive (terraces) and depositional (drifts) features. The Mar del Plata Canyon intersects the CDS. Redrawn from *Preu et al.* [2013]; *Voigt et al.* [2016] and *Voigt et al.* [2013] with surface sediment distribution on the Ewing Terrace [*Bozzano et al.*, 2011]. Gravity cores locations and water masses with their modern boundaries affecting sedimentation along the Argentine continental margin have been indicated: AABW – Antarctic Bottom Water, AAIW – Antarctic Intermediate Water, LCDW – Lower Circumpolar Water, NADW – North Atlantic Deep Water, UCDW – Upper Circumpolar Deep Water, SCW – southern component water.

(II) The Ewing Terrace on the middle slope in 1200 – 1400 m water depth is the largest terrace of the CDS and is continuous along the Patagonian margin [Figure 1.10; *Hernández-Molina et al.*, 2009]. Erosion at this depth is related to the AAIW [*Preu et al.*, 2013] flowing as a fast bottom current favored by margin morphology with regional flow velocities of 15-20 cm s⁻¹ in 1000 m water depth [*Gwiliam*, 1996]. The terrace is located at the boundary of AAIW and UCDW, resulting in erosion, i.e., along a deep contouritic channel in the transition between the middle slope and Ewing Terrace, and plastered drift deposition on the seaward boundary of the terrace [*Preu et al.*, 2013]. The latter requires a continuous decrease in flow velocities with increasing distance from the middle slope allowing the deposition of recently eroded material.

(III) Along the deepest Necochea Terrace (Figure 1.10), *Preu et al.* [2013] and *Hernández-Molina et al.* [2009] described continuous elongated drift deposits based on seismic investigations. Corresponding sediments were proposed to be delivered by the glacial and northward-flowing LCDW/AABW nepheloid-layer in 3500 to 3900 m water depth (Figure 1.10). The modern LCDW/AABW interface is located below the Necochea Terrace at about 4000 m water depth [*Stramma and England, 1999*], thus, displaying a modern LCDW-influenced Necochea Terrace.

1.3.4 The blind Mar del Plata Canyon

The Mar del Plata Canyon at 38°S incises the CDS at the Argentine continental margin in WNW–ESE orientation [*Krastel et al., 2011; Violante et al., 2010*]. The canyon head is located at about 1,000 m water depth (Figure 1.10). The canyon extends over 110 km distance down to the Necochea Terrace in ca. 3900 m water depth [*Krastel et al., 2011*]. Generally, the canyon reveals a V-shaped cross section and steep flanks. Incisions vary from 200 m in the upper part to 1000 m in the middle part and decreases at the distal end at water depths exceeding 3400 m [*Krastel et al., 2011*]. Similarly to the incision, canyon sinuosity varies from a meandering to an almost straight pattern from the top to the bottom (Figure 1.10). Based on hydroacoustic and seismic investigations, *Krastel et al.* [2011] showed that this canyon does not have a refilled or buried upslope continuation to the shelf.

1.4 Oceanographic proxies

1.4.1 Sortable silt – The paleocurrent proxy

“Sortable silt” mean size (SS_{mean}) and weight percentage ($SS_{\%}$) are sedimentological near-bottom paleo-current strength proxies (Figure 1.11a), whose size sorting vary in response to hydrodynamic processes [*McCave et al., 1995*]. Sediment sorting occurs principally during resuspension or deposition by processes of aggregate breakup and particle size selection related to settling velocity and stress [*McCave et al., 1995*]. Strengthened currents increase shear stress along the seafloor and particles become resuspended. When currents weaken, particles settle out and redeposit on the seafloor (Figure 1.11b).

During the last decades, several studies supported the use of the “sortable silt” fraction for paleoceanographic studies and obtained variations in current strength of major water masses, i.e., in the Southern Ocean [e.g., *McCave et al., 2014*], North Atlantic [e.g., *Bianchi and McCave, 1999; Channell et al., 2016*] or South Atlantic [e.g., *Diekmann and Kuhn, 2002; Frenz et al., 2003; Krueger et al., 2008; Voigt et al., 2016*].

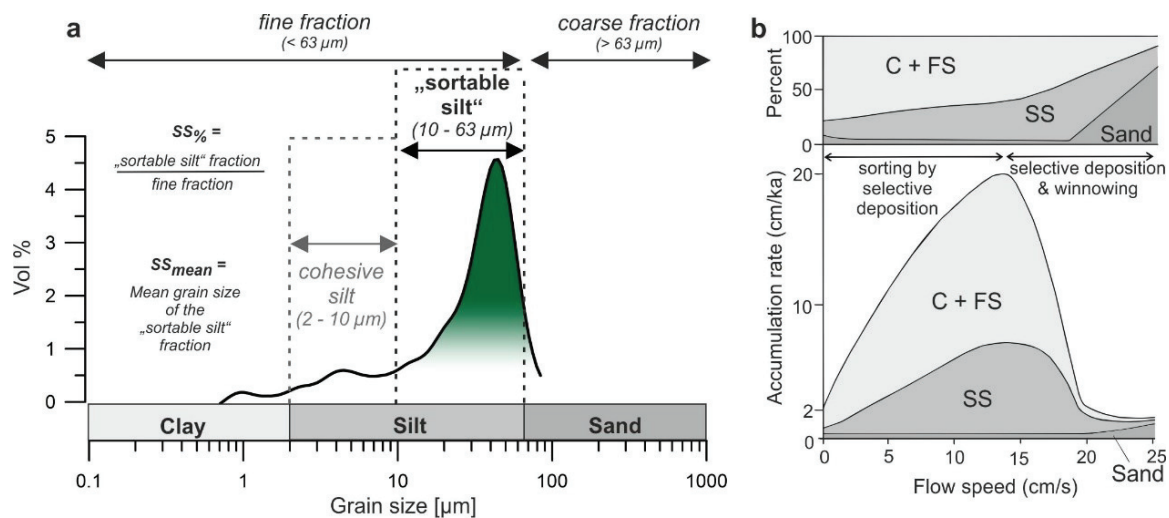


Figure 1.11: (a) Grain size distribution and sortable silt (SS) parameter classification [McCave *et al.*, 1995]. (b) Flow speed versus accumulation rate resulting in winnowing or deposition of specific grain-size classes, redrawn from McCave and Hall [2006] (C – clay, FS – fine silt, SS – sortable silt).

The SS_{mean} of the 10 – 63 μm terrigenous silt fraction (Figure 1.11a) is a parameter that varies independently of the sediment supply in current sorted and deposited muds (< 63 μm). SS_{mean} of the 10- 63 μm is a more sensitive indicator of bottom current strength than the total silt fraction (63 – 2 μm) which includes cohesive material initially defined by Ellwood and Ledbetter [1977]. Due to the break-up of aggregates, silt coarser than 10 μm largely responds to hydrodynamic forces on erosion and deposition as single particles. Higher SS_{mean} values represent relatively stronger near-bottom flow strength and vice versa [McCave *et al.*, 2014]. Since deposition of coarser material under strong currents also involves suppression of fine sediment deposition, the $SS_{\%}$ can be used to support the SS_{mean} as an indicator of current strength (Figure 1.11).

1.4.2 Clay mineralogy – The transport pathway proxy

Clay minerals are the main constituents of modern abyssal sediment. During the last decades, downcore clay mineral fluctuations were used as reliable tracers of past deep water composition in the South Atlantic [Petschick *et al.*, 1996]. These clay minerals, i.e. chlorite, illite, kaolinite and smectite, are useful proxies to reconstruct variable extensions of northern and southern sourced deep water routes (Figure 1.12a) by monitoring their current-transported fine-grained detritus [e.g., Diekmann *et al.*, 2000; Diekmann *et al.*, 1996; Krueger *et al.*, 2008; Petschick *et al.*, 1996].

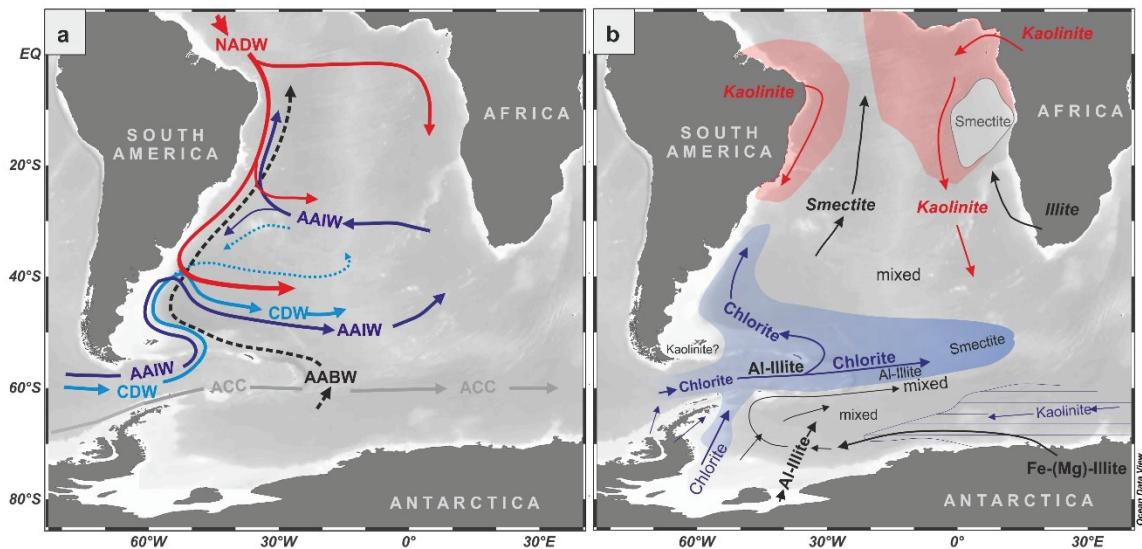


Figure 1.12: (a) Oceanographic configuration [Stramma and England, 1999] and (b) corresponding clay mineral path ways in the South Atlantic specified by Petschick et al. [1996]. AABW: Antarctic Bottom Water, ACC: Antarctic Circumpolar Current, AAIW: Antarctic Intermediate Water, CDW: Circumpolar Deep Water, NADW: North Atlantic Deep Water.

The clay mineral distribution in surface sediments of the South Atlantic and adjacent Southern Ocean was described in detail by *Petschick et al.* [1996]. The resulting elementary clay mineral distribution pattern is depicted in Figure 1.12b:

(I) *Petschick et al.* [1996] and *Diekmann and Kuhn* [1999] defined the distribution of chlorite and well crystallized (Al-)illite (Figure 1.12b), which is related to the northward flowing SCW derived from Antarctic Peninsula and southernmost South America where granitoid batholiths and low metamorphic Andean rocks of West Antarctica remain. These components are commonly derived from the Pacific coast of Antarctica via the Drake Passage. Since chlorite is destroyed by chemical weathering in warm and humid climates of adjacent tropical source, a chlorite minimum is confined to low latitudes along the coasts off Brazil and West Africa.

(II) Smectite is related to high amounts of Si-poor rocks, located in southern South America, Antarctic Peninsular and volcanic arcs. The mineral is enriched in the subantarctic and subtropical South Atlantic and transported by northerly and easterly flowing bottom currents [*Petschick et al.*, 1996].

(III) In contrast to chlorite or smectite, kaolinite and poorly crystallized illite were observed where the southward flowing NADW prevails (Figure 1.12b). These clay minerals reveal a dominant latitudinal distribution with increased amounts in the low latitudes, where continental source rocks (e. g., from Brazil) are mainly affected by intensive chemical weathering [*Petschick et al.*, 1996]. Low kaolinite content is restricted to the circumantarctic area between 50°S and 60°S, most probably as a result of dilution by high amounts of smectite and chlorite [*Petschick et al.*, 1996].

1.5 Thesis Outline

This dissertation comprises an “introductory” chapter (Chapter 1) followed by three stand-alone manuscripts, which have already been published, are under review or will soon be submitted to peer-reviewed international scientific journals.

The first manuscript “*Deglacial changes in the strength of deep southern component water strength and sediment supply at the Argentine continental margin*” (Chapter 2) assesses the persistent but variable deep SCW nepheloid layer discharge along the Argentine continental margin during the last 20,000 years. The manuscript shows an increased current strength of deep SCW during the late deglacial, connected to the high-energetic LCDW/AABW interface occupying all core sites. The increase was related to the deglacial re-initiation of modern NADW.

The second manuscript “*Interaction of a deep-sea current with a blind submarine canyon (Mardel Plata Canyon)*” (Chapter 3) provides new insights into turbidity-current activity in a mid-slope canyon, which has no direct connection to shelf or onshore-river system. Results from sediment cores shows that the glacial AAIW nepheloid layer led to increased sediment deposition along the Ewing Terrace and that these mid-slope sediments are the source of turbidity-currents. The AAIW position and strength were the main trigger for glacial slope instabilities within a blind-canyon system.

The third manuscript “*Deglacial shift of deep southern component water in the Southwest Atlantic*” (Chapter 4) focuses on deep water mass circulation using a core transect covering the whole range of the deep South Atlantic water masses. Based on the findings, the temporal and vertical migration of the LCDW/AABW interface within the water column was reconstructed during the late deglacial period due to the coherent deepening of the NCW/SCW interface.

1.6 Declaration of co-author contributions

All manuscripts of this dissertation were developed in close collaboration with the co-authors. This section provides information on the individual contributions of each co-author to the individual manuscripts and the current manuscript status.

Chapter 2: “*Deglacial changes in the strength of deep southern component water strength and sediment supply at the Argentine continental margin*”

Grit Warratz, Rüdiger Henrich, Ines Voigt, Cristiano M. Chiessi, Gerhard Kuhn, Hendrik Lantzsch

Status: Published in *Paleoceanography* 34 on 20 July 2017

The three sediment cores utilized in this study were collected during Meteor Cruise M78/3 (2009, Chief Scientist: Sebastian Krastel). I confirm that I have carried out all sample preparation (i.e. grain-size separations; chemical preparation; selection of planktonic foraminifera for radiocarbon dating, radiographic images) and measurements (i.e. grain-size measurements with the Sedigraph; carbonate, total carbon and organic carbon measurements with LECO; X-ray diffraction of oriented clay filter cakes at AWI, Bremerhaven; X-ray fluorescence (XRF) core scans; magnetic susceptibility (MS) core scans) and data processing (e.g., age model generation using calib 7.0 and AnalySeries 1.1; calculation of clay mineral assemblages with MacDiff 4.2.6), except of data-provided by Ines Voigt (XRF scans and radiographs of GeoB13861-1 and GeoB13862-1). I further confirm that I have predominantly contributed to the overall scientific concept and the interpretation of all data, created all figures and tables, and wrote all sections of the manuscript. However, the interpretation greatly benefitted from regular discussion with all co-authors.

(Personal contribution: ~ 80 %)

Chapter 3: “Interaction of a deep-sea current with a blind submarine canyon (Mar del Plata Canyon)”

Grit Warratz, Tilmann Schwenk, Ines Voigt, Graziella Bozzano, Rüdiger Henrich, Roberto Violante, Hendrik Lantzsch

Status: Submitted to *Sedimentology* on 02 August 2017

The three sediment cores, bathymetric, and hydro-acoustic data sets used in this study were acquired during Meteor Cruise M78/3. The scientific concept of this manuscript was developed during preparation of the 1st Manuscript (Chapter 2). I confirm that I have carried out all sedimentological analyses (see section above). In addition, I confirm that I have taken all turbidite samples for grain-size analyses with the Laser Diffraction Particle Analyzer at MARUM. XRD random powder sample measurements were carried by Christoph Vogt. I have interpreted the mineralogical composition. Bathymetric data sets and hydro-acoustic profiles were processed by Tilmann Schwenk. I have created the bathymetric maps using Generic Mapping Tools. I further confirm that I have predominantly contributed to the scientific concept and interpretation of all data, created and improved all figures (except for Figure 3.3, which was created by Tilmann Schwenk) as well as tables, and wrote all sections of the manuscript (except for section 3.4.1, which was developed in cooperation with Tilmann Schwenk). The interpretation was a continuous process, which benefitted from suggestions and regular discussions with Tilmann Schwenk and all further co-authors.

(Personal contribution: ~ 70 %)

Chapter 4: “Deglacial shift of deep southern component water in the Southwest Atlantic”

Grit Warratz, Ines Voigt, Cristiano M. Chiessi, Rüdiger Henrich, Hendrik Lantsch

Status: In preparation for submission to *Earth and Planetary Science Letters*

This manuscript comprises a compilation of all sediment core data sets from the 1st and 2nd Manuscript (Chapter 2 and 3) and two new cores (i.e. GeoB6308 and GeoB6309). I confirm that I have carried out the sample preparation, grain-size separation, and grain-size measurements (Sedigraph and Laser Particle Size Analyzer), and generated the age model in close collaboration with Ines Voigt and Cristiano Chiessi. The latter co-author provided new total organic carbon radiocarbon ages (TOC AMS ¹⁴C ages). I confirm that I mainly contributed to the scientific concept and interpretation, created all figures, and wrote the whole manuscript. The interpretation was improved by regular discussion with all co-authors.

(Personal contribution: ~ 80)

Chapter 2

Deglacial changes in the strength of deep southern component water and sediment supply at the Argentine continental margin

**Grit Warratz¹, Rüdiger Henrich¹, Ines Voigt¹, Cristiano M. Chiessi², Gerhard Kuhn³,
Hendrik Lantzsich¹**

¹University of Bremen, MARUM – Center for Marine Environmental Sciences and Faculty of Geosciences, Klagenfurter Straße, D-28359 Bremen, Germany.

²School of Arts, Sciences and Humanities, University of São Paulo, Av. Arlindo Bettio 1000, CEP03828-000 São Paulo SP, Brazil.

³Alfred-Wegener-Institut Helmholtz-Zentrum für Polar und Meeresforschung, Bremerhaven, Am Alten Hafen 26, D-27568 Bremerhaven, Germany.

*- Manuscript published in *Paleoceanography* -*

Citation:

*Warratz, G., R. Henrich, I. Voigt, C. M. Chiessi, G. Kuhn, and H. Lantzsich (2017), Deglacial changes in the strength of deep southern component water and sediment supply at the Argentine continental margin, *Paleoceanography*, 32, doi:10.1002/2016PA003079*

Abstract

The deep southern component water (SCW), comprising Lower Circumpolar Deep Water (LCDW) and Antarctic Bottom Water (AABW), is a major component of the global oceanic circulation. It has been suggested that the deep Atlantic water mass structure changed significantly during the last glacial/interglacial cycle. However, deep SCW source-proximal records remain sparse. Here we present three coherent deep SCW paleo-current records from the deep Argentine continental margin shedding light on deep-water circulation and deep SCW flow strength in the Southwest Atlantic since the Last Glacial Maximum (LGM). Based on increased sortable silt values, we propose enhanced deep SCW flow strength from 14 to 10 cal ka BP relative to the early deglacial/LGM and the Holocene. We propose a direct influence of deep northern component water (NCW) on deep SCW flow strength due to vertical narrowing of deep SCW spreading, concurrent with a migration of the high-energetic LCDW/AABW interface occupying our core sites. We suggest a shoaled NCW until 13 cal ka BP, thereby providing space for deep SCW spreading that resulted in reduced carbonate preservation at our core sites. Increased carbonate content from 13 cal ka BP indicates that the NCW expanded changing deep water properties at our core sites in the deep Southwest Atlantic. However, southern-sourced terrigenous sediments continued to be deposited at our core sites, suggesting that deep SCW flow was uninterrupted along the Argentine continental margin since the LGM.

2.1 Introduction

The deep southern component water (SCW) (i.e., Lower Circumpolar Deep Water (LCDW) and Antarctic Bottom Water (AABW)) is an important component of the global deep overturning circulation. Deep SCW flows northward along the Argentine continental margin to ventilate the deep-waters of the Atlantic Ocean [Stramma and England, 1999]. It was suggested that any change in deep SCW circulation pattern would have a major influence on global climate, since deep-water formation processes set the interhemispheric shape and strength of the deep global overturning cell [e.g., Kuhlbrodt *et al.*, 2007].

Marked reorganizations of the South Atlantic Ocean circulation occurred from the Last Glacial Maximum [LGM, 23-19 cal ka BP, Mix *et al.*, 2001] into the Holocene [e.g., Curry and Oppo, 2005; Howe *et al.*, 2016; Marchitto and Broecker, 2006; Marchitto *et al.*, 1998, Menviel *et al.*, 2016]. Several authors propose a continued but shoaled and freshened glacial North Atlantic Deep Water (NADW) southward flow during the LGM [e.g., Lynch-Stieglitz *et al.*, 2007] without a major reduction in the overturning cell, but implying that the deep SCW were expanded at depth [Freeman *et al.*, 2016; Lippold *et al.*, 2016]. In contrast, others suggest that this deep SCW expansion was probably not as extensive during the LGM as previously suggested [Howe *et al.*, 2016].

Thus, although the deep-water mass geometry in the Southwest Atlantic changed over the last 20 ka [e.g., Curry and Oppo, 2005; Freeman *et al.*, 2016; Lippold *et al.*, 2016; Oppo and Curry, 2012], there is little knowledge about the variability of the deep SCW circulation (i.e., flow strength) in this source-proximal area. The lack of information is commonly related to low carbonate content of deep Southwest Atlantic glacial sediments attributed to strongly corrosive deep-water masses [e.g., Volbers and Henrich, 2002]. Missing carbonate severely limits age control and makes changes in deep SCW circulation difficult to assess [Kuhn and Diekmann, 2002].

Here, we are able to overcome this issue by analyzing three radiocarbon-dated sediment cores (~ 3750 m water depth) from a submarine canyon (i.e., Mar del Plata Canyon) and an adjacent deep sea terrace (i.e., Necochea Terrace) at the Argentine continental margin (Figure 2.1). We first reconstruct the source of the sediment deposited within the distal Mar del Plata Canyon and along the Necochea Terrace using clay mineral assemblages and their relation to source areas [Diekmann and Kuhn, 1999; Krueger *et al.*, 2008; Petschick *et al.*, 1996]. Secondly, we use fluctuations in carbonate contents, primarily controlled by dissolution, to monitor changes in deep-water chemistry which respond to changes in water mass geometry [Henrich *et al.*, 2003; Volbers and Henrich, 2004]. Finally, we assess relative flow strength variations of the deep SCW using sortable silt as a paleo-current strength proxy [McCave, 2008; McCave *et al.*, 1995].

2.2 Background information

2.2.1 Physiography and oceanographic setting

The Southwest Atlantic forms an oceanographic key location in the global conveyor belt, where major surface, intermediate and deep-water masses converge [Gordon, 1981; Piola and Gordon, 1989]. Different water masses that are formed in remote areas of the world (i.e., the North Atlantic, South Pacific and Antarctic regions) extend into the Southwest Atlantic and generate one of the most energetic regions in the world ocean [Reid, 1989; Stramma and England, 1999]. The modern intermediate and deep-water layers are governed by the northward-flowing Antarctic Intermediate Water (AAIW, ~500-1000 m), Circumpolar Deep Water (CDW, ~1000-4000 m) and Antarctic Bottom Water (AABW, >4000 m) [Reid et al., 1977; Stramma and England, 1999] (Figure 2.1a). The southward-flowing North Atlantic Deep Water (NADW; ~ 2000 - 3000 m) vertically divides CDW into the Upper and Lower CDW (UCDW and LCDW, respectively) [Arhan et al., 2003; Piola and Matano, 2001]. In particular, the southern sourced AABW is one of the major components of the global meridional circulation [e.g., Rahmstorf, 2002]. The cold and low salinity AABW [Reid, 1996; Orsi et al., 1999] can be formed by two processes, namely by mixing of ice-shelf water (ISW) and CDW, and also by coastal polynya activity in various areas around Antarctica (i.e., Weddel Sea, Adélie Land, Ross-Sea, Prydz Bay) [e.g., Stramma and England, 1999; Orsi et al., 1999, Bindoff, 2000]. The ISW Mode depends on the existence of large ice shelves [Krueger et al., 2012] related to higher sea levels. The water underneath these ice shelves is super-cooled and flows down the slope forming deep SCW [Foldvik and Gammelsrod, 1988]. The Polynya Mode corresponds to atmosphere-sea-ice-ocean interactions on the large continental shelf of the Weddell Sea and in polynyas [Krueger et al., 2012; Smith et al., 2010]. Due to the contact with the atmosphere, the surface water cools down and results in dense brine water [i.e., Killworth, 1977]. The LCDW is a highly saline water mass of the CDW that in turn occupies most of the deep layers of the Antarctic Circumpolar Current (ACC) and is assumed to be mainly or entirely wind driven [Orsi et al., 1995; Barker and Thomas, 2004], but with restraining influence of perennial sea-ice cover changes as well [McCave et al., 2014].

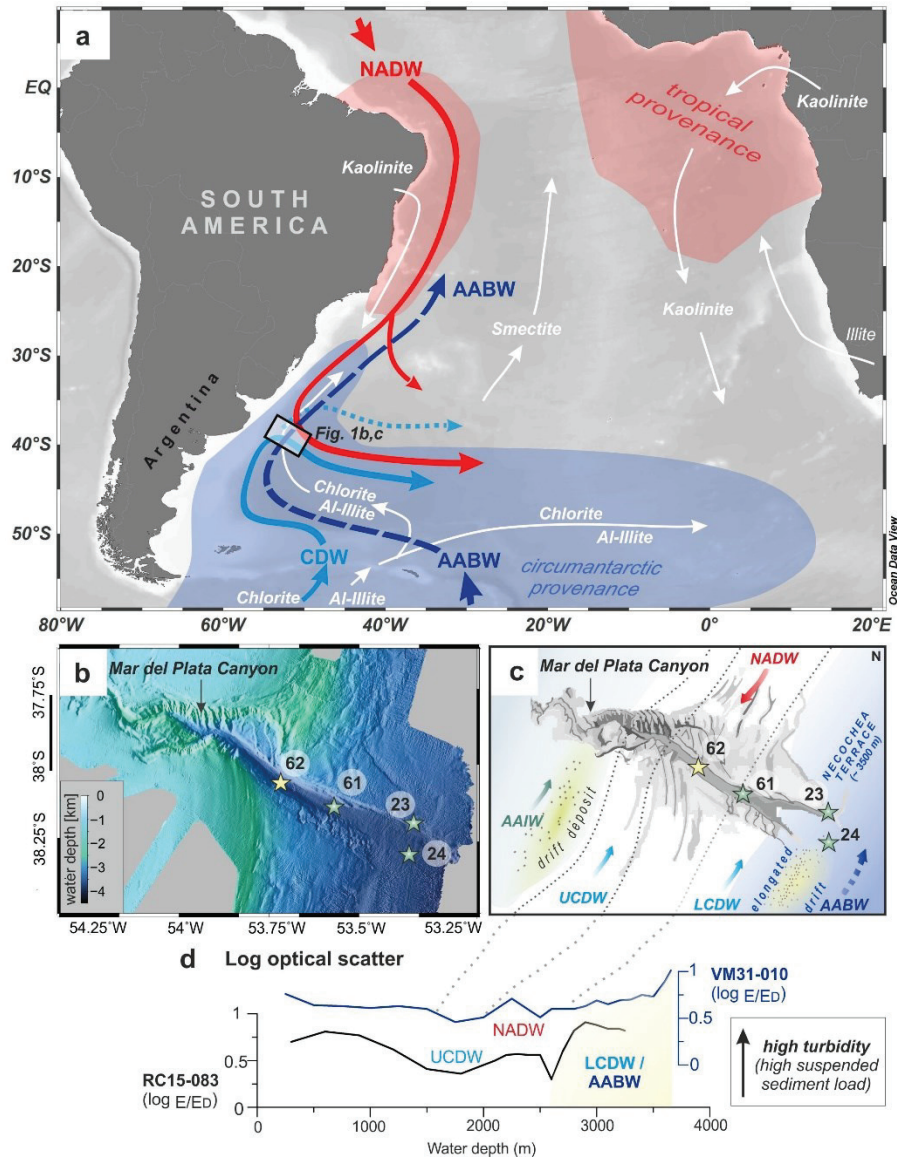


Figure 2.1: Location of the investigated marine sediment cores together with the main elements of the deep circulation and bathymetry of the Southwest Atlantic (map created using Ocean Data View [Schlitzer, 2002, 2015]). **(a)** Schematic deep-water circulation based on Stramma and England [1999]. Thick arrows indicate the flow of the major deep-water masses color coded according to their ventilation source region; blue: Antarctic Bottom Water (AABW) and Circumpolar Deep Water (CDW), red: North Atlantic Deep Water (NADW). Black box shows the location of the Mar del Plata Canyon and the Necochea Terrace. Shaded areas indicate clay mineral source areas; blue: circumantarctic provenance, red: tropical provenance. Thin white arrows indicate clay mineral transport pathways after Petschick *et al.* [1996]. **(b)** Bathymetric map of the Mar del Plata Canyon and the Necochea Terrace [Krastel *et al.*, 2001] (green stars: GeoB13823-2 (23), GeoB13824-1 (24), GeoB13861-1 (61) from this study; yellow star: GeoB13862-1 (62) from Voigt *et al.* [2013]). **(c)** Modern deep-water masses influencing the Mar del Plata Canyon and adjacent drift deposits depicted yellow according to Preu *et al.* [2013]. AAIW: Antarctic Intermediate Water, LCDW: Lower Circumpolar Deep Water, UCDW: Upper Circumpolar Deep Water. **(d)** Turbidity measurements at the southern flank of the Mar del Plata Canyon at 38°S (RC15-083) and to the north of the canyon at 37°S (VM31-010) from the world ocean nepheloid layer composition data base assembled by Lamont-Doherty Earth Observatory [GeoMapApp.org] implying a pronounced northward-flowing LCDW-AABW nepheloid layer

that testifies strong current activity in the range of deep Antarctic sourced water masses (yellow shaded area).

These intermediate and deep-water masses are responsible for a contourite depositional system (CDS) at the Argentine continental margin [e.g., *Hernandez-Molina et al.*, 2009]. In particular, around ~3500 m water depth the relatively strong LCDW and AABW shape the Argentine continental margin and build up elongated drifts along the Necochea Terrace [*Preu et al.*, 2013]. The large and deeply incised Mar del Plata Canyon (Fig. 2.1a to c), a typical mid-slope canyon system, is also incorporated into this major CDS [*Hernandez-Molina et al.*, 2009; *Preu et al.*, 2013]. The canyon head is located at about 1000 m water depth. The canyon extends over 110 km distance and terminates on the Necochea Terrace in a water depth of ~3900 m (Figure 2.1b and c) [*Krastel et al.*, 2011].

Recently, *Voigt et al.* [2013] have shown that the upper part of the Mar del Plata Canyon interacts with an intermediate-depth nepheloid layer generated by the northward-flowing AAIW. The deposits inside the upper canyon reveal sediment characteristics similar to drift deposits. More precisely, the dominance of the sortable silt fraction over other particle sizes in the canyon [*Voigt et al.*, 2013] indicates that deposition responds to current-controlled hydrodynamic processes [*McCave et al.*, 1995]. Furthermore, sortable silt reconstructions [*Voigt et al.*, 2016] show a good correspondence with abrupt variations in the Atlantic Meridional Overturning Circulation (AMOC) with enhanced (reduced) northward advection of AAIW during periods of reduced (enhanced) NADW circulation during the Holocene.

Here we focus on variations in deep SCW variability using sediments from the distal part of the Mar del Plata Canyon and the Necochea Terrace (Figure 2.1a to c). Modern log optical measurements from the world ocean nepheloid layer composition data base of the Lamont-Doherty Earth Observatory performed to the north and south of the Mar del Plata Canyon revealed high turbidity, to testify strong current activity in the range of the LCDW/AABW (Figure 2.1d).

Seismic investigations suggest continuous elongated drift deposits on the Necochea Terrace [*Hernandez-Molina et al.*, 2009; *Preu et al.*, 2013]. The corresponding sediments are proposed to be delivered by the northward-flowing LCDW/AABW nepheloid-layer [*Preu et al.*, 2013]. The modern LCDW/AABW interface is located below the Necochea Terrace at about 4000 m water depth [*Stramma and England*, 1999] (Figure 2.1c). This water mass interface is suggested to represent pycnoclines affected by several baroclinic activities and zones dominated by turbulent and intense bottom currents (e.g. internal tides) [*Arhan et al.*, 2002a; *Cacchione et al.*, 2002; *Reid et al.*, 1977]. Such interfaces of two water masses moving in the same direction are particu-

larly susceptible to vertical mixing and the generation and propagation of turbulence and enhanced current strength [Pomar *et al.*, 2012; Preu *et al.*, 2013]. The resulting contourite deposits thus potentially constitute an important and continuous paleoceanographic archive for variations of the deep-water mass.

2.2.2 Clay mineral provenances

Clay mineral assemblages in marine sediments are strongly controlled by source rock compositions, physico-chemical weathering mechanisms, and sedimentary processes [Biscaye, 1965; Ehrmann *et al.*, 1992; Petschick *et al.*, 1996; Diekmann and Kuhn, 1999]. The Argentine continental margin is most effectively controlled by deep- and bottom water advection [Biscaye and Eittrheim, 1977]. Current transport and depositional mechanisms determine a selective enrichment of diverse clay minerals [Petschick *et al.*, 1996] which favor the use of clay minerals as water mass tracers [Diekmann *et al.*, 1996].

Northward-flowing LCDW and AABW deliver illite, chlorite and smectite to the deep Southwest Atlantic Ocean (Figure 2.1a) [Petschick *et al.*, 1996]. Southern sourced illites are generally well crystallized and highly muscovitic. These Al-illites (and chlorite) are indicative for granitoid batholiths, felsic igneous or low metamorphic rocks mainly found in the Andes of Antarctic Peninsula [Petschick *et al.*, 1996]. High chlorite amounts typically characterize sediments from the shelf off Dronning Maud Land [Petschick *et al.*, 1996] or from the Patagonian shelf through the Drake Passage and Scotia Sea [Diekmann *et al.*, 2000; Biscaye, 1965]. Submarine weathering or early diagenetic transformation of basaltic rocks and volcanic glass result in well-crystallized smectite enrichments. Well-crystallized smectite is connected to source areas with physical weathering of Si-poor rocks (i.e., southern South America, Antarctic Peninsula) and/or volcanic environments (i.e., the Pacific side of the Antarctic Peninsula, Scotia Sea) [Petschick *et al.*, 1996].

In contrast to the northward advection of illite, chlorite and smectite, intensive chemical weathering in the tropics supplies continentally derived kaolinite into the Atlantic (Figure 2.1a) which is typically resuspended by the southward-flowing NADW [Biscaye, 1965].

2.3 Materials and methods

We investigated one gravity core within the distal Mar del Plata Canyon (GeoB13861-1) and two gravity cores collected from the Necochea Terrace (GeoB13823-2 and GeoB13824-1). The sediment cores (Figure 2.1b, Table 2.1) were collected during RV Meteor Cruise M78/3 [Krastel and Wefer, 2012].

Table 2.1: Location and corresponding data of the sediment cores used in this study.

Cruise	Core	Latitude	Longitude	Water depth (m)	Recovery (cm)
M78/3b	GeoB13861-1	38°09.18'S	53°60.98'W	3715	668
M78/3a	GeoB13824-1	38°13.14'S	53°21.29'W	3821	1066
M78/3a	GeoB13823-2	38°08.68'S	53°20.64'W	3780	938

2.3.1 Visual core description and radiographs

Lithological investigations were carried out to define sediment characteristics and depositional processes. For an exact differentiation between homogenous silty background sedimentation and intercalated sandy or muddy layers, 1 cm thick vertical sediment slices were taken for radiographic imaging. All three sediment cores are undisturbed and reveal a complete sedimentary record required for a paleoceanographic study after removing down-slope delivered sediment sections (see supporting information, Figure 2.SI 1).

2.3.2 Age models

The stratigraphy of the studied sediment cores was determined using (i) six new AMS-¹⁴C ages performed on mixed planktonic foraminifera, and (ii) the correlation of Fe/K records of our three cores with the Fe/K record of the AMS-¹⁴C dated nearby core GeoB13862-1 [see supporting information Figure 2.SI 2; Voigt *et al.*, 2013]. Due to low carbonate contents in deep South Atlantic areas [e.g., Volbers and Henrich, 2002] mixed species assemblages were selected in 1.5 cm-thick samples in order to obtain sufficient carbonate for dating. The dominant species were *Globorotalia inflata* and *Globigerina bulloides*. In case of very low carbonate contents (< 1 %) two samples were collected over a 5 cm-thick interval. The corresponding radiocarbon ages are displayed as the median age. Conventional radiocarbon ages were determined in the Poznan Radiocarbon Laboratory (Poland) and ETH Zürich, Switzerland [Bard *et al.*, 2015]. Radiocarbon ages (Table 2.2) were converted to calibrated ages (cal ka BP) using the CALIB 7.0.0 radiocarbon calibration program applying the Marine13 calibration curve with a standard reservoir age of 405 years [Reimer *et al.*, 2013].

Table 2.2: Accelerator mass spectrometry radiocarbon dates and calibrated ages.

Lab Sample Code	Depth (cm)	Species	Radiocarbon age $\pm 1\sigma$ error	1 σ calibrated age range (cal ka BP)	Calibrated age from 1 σ range (cal ka BP)
GeoB13861-1					
Poz-68951	139	<i>G. inflata</i> , <i>G. bulloides</i>	8930 \pm 50	9.52-9.64	9.58
Poz-68952	250	<i>G. inflata</i> , <i>G. bulloides</i> mixed foraminifera	10880 \pm 60	12.30-12.54	12.43
Poz-73049	505	*	15120 \pm 80	17.8-18.02	17.91
GeoB13823-2					
Poz-38953	120	<i>G. inflata</i> , <i>G. bulloides</i> mixed foraminifera	10990 \pm 60	12.49-12.61	12.55
Poz-68954	454-470	*	13570 \pm 190	15.50-16.08	15.79
**ETH-66208	627-631	<i>G. inflata</i> , <i>G. bulloides</i> , shell frag- ments	12490 \pm 120		
ETH-66209	850-854,5	<i>G. inflata</i> , <i>G. bulloides</i>	15780 \pm 160	16.85-16.52	16.69

*Mixed foraminifera consist of *Globorotalia inflata*, *Globigerina bulloides*, *Bolivina inflata* and *Globolumnia affinis*.

** We decided not to use the age obtained for sample **ETH-66208, because the sample had surface contamination and suffered partial loss during the leaching process. Additionally, the presence of benthic shell fragments might also have biased the radiocarbon age

2.3.3 XRF core scanning

X-ray fluorescence (XRF) scans of the sediment cores were performed at 1 cm intervals. We applied generator settings of 10kV, a current of 0.2 mA directly at the split core surface of the archive halves using the AVAATECH XRF Core Scanner II (AVAATECH Serial No. 2) at the MARUM - University of Bremen. Element intensities are given in counts per second (cps). We focused on elemental distributions of iron and potassium for stratigraphic correlation.

2.3.4 Biogenic opal, carbonate and organic carbon content

Biogenic opal content was determined with the sequential leaching technique described in Müller and Schneider [1993]. Total carbon (TC) and total organic carbon (TOC) were determined using freeze dried and homogenized bulk sub-samples of cores GeoB13861-1 and GeoB13823-2 and were measured with the LECO CS200 element analyzer [Bernard et al., 1995]. For a second

run, calcium carbonate was removed in advance by adding some aliquots of 0.25 N HCl to determine organic carbon content. The carbonate content was calculated from the difference between TC and TOC [$\text{CaCO}_3 = (\text{TC} - \text{TOC}) * 8.33$].

2.3.5 Grain-size determination

Following *McCave* [2008], *McCave et al.* [1995] and *Robinson and McCave* [1994], sortable silt (10 - 63 μm) arithmetical mean size (SS_{mean} in μm) and percentage ($\text{SS}_{\%}$) values can be tightly linked to hydrodynamic processes and can be used as a relative flow-strength indicator. Thus, sortable silt proxies give evidence for shifts in water mass circulations strength with low (high) SS_{mean} and $\text{SS}_{\%}$ indicative for weak (strong) current strength [*McCave*, 2008].

Prior to sortable silt measurements, bulk grain-size analyses were performed with sample interval of 10 cm. Wet sieving of 10-14 g freeze dried samples through a 63 μm mesh sieve enabled to separate the sand size fraction from the silt/mud fraction. Sand fraction were subdivided (63-125 μm , 125-250 μm , 250-500 μm , 500-1000 μm and >1000 μm fractions) with an ATM-Sonic-Sifter. Dispersive agent $\text{Na}_4\text{P}_2\text{O}_7 * 10 \text{H}_2\text{O}$ was added to the < 63 μm fraction to minimize clay content to < 5 % using settling tubes (10-20 times) according to Stoke's Law. Since biogenic opal content is negligible (< 5 %) < 63 μm -fraction was measured with the Sedigraph D5000 after carbonate removal (for method see *Mulitza et al.* [2008]). All glacial sediments were barren of biogenic carbonate, we therefore decided that samples with less than 1 % carbonate are carbonate-free.

2.3.6 Clay mineral analyses

The clay-size fraction (< 2 μm) was analyzed using X-ray diffraction (XRD). XRD measurements were conducted on a PANalytical EMPYREAN device (Alfred-Wegener-Institute, Helmholtz Centre for Marine Polar Research, Bremerhaven) using $\text{CuK}\alpha$ radiation (40 kV, 40 mA; high resolution theta-theta goniometer, fixed divergence, PIXEL^{3D} detector). Each sample was analyzed between 2.5° and 29° 2 θ , with a step size of 0.013° in the air-dried state and after ethylene glycol solvation. X-ray diffraction measurements were performed on organic and carbonate-free, preferentially oriented clay-size filter cakes with molybdenite as an internal standard. Further details of sample preparation techniques are described in *Petschick et al.* [1996] and *Diekmann and Kuhn* [1999]. Diffractograms were evaluated using the "MacDiff 4.2.5" software [*Petschick et al.*, 1996] without using a weighted average smoothing but applying a molybdenite (006) peak correction.

Abundance of individual clay mineral groups (chlorite, illite, kaolinite, smectite) were semi-quantitatively estimated by using ratios of integrated peak areas of their main basal reflections [Petschick *et al.*, 1996]. Percentages of each clay mineral were computed using empirically estimated weighting factors [Biscaye, 1965]. The composition of kaolinite and chlorite were estimated by peak fit deconvolution of their doublet at 24.8 and 25.2 ° 2 θ . Integral breadth-values (IB in $\Delta^{\circ}2\theta$) were calculated using the glycolated 17 Å-smectite (IB < 1.5 well crystalline, IB > 2.0 poorly crystalline) and 10 Å-illite peaks (IB < 0.4 very well crystalline, IB 0.4-0.8 well to moderately crystalline) as described in Petschick *et al.* [1996] and Diekmann *et al.* [1996]. The illite 5 Å/10 Å peak intensity ratios (> 0.4 Al-rich, < 0.15 Mg- and Fe-rich) were used to approximate the octahedral character [Esquevin, 1969].

2.4 Results

2.4.1 Age models and linear sedimentation rates

All three sediment cores reveal undisturbed tops and no loss of recovery. The background sediment record mainly consist of hemipelagic sediments. All thin-bedded and fine-grained turbidites were identified from color, grain-size data, and radiographic images [Bouma *et al.*, 1962, Shanmugam, 1997]. Hence, turbidite beds were cut and a new down-core depth scale was calculated (supporting information), following the methodological approach described in Henrich *et al.* [2010]. The new down-core depth scale was used to establish the age models and to calculate the corresponding linear sedimentation rates (LSR) (Figure 2.2).

GeoB13861-1 shows sedimentation rates of 21 cm/ka until 12.5 cal ka BP, followed by an increase to 31 cm/ka from ~ 12.5 to 9 cal ka BP (Figure 2.2). The Holocene reveals an average rate of 21 cm/ka with a slight increase from 5 to 1 cal ka BP.

In contrast, GeoB13823-2 and GeoB13824-1 from the Necochea Terrace indicate thick glacial/deglacial deposits until 12.5 cal ka BP with extraordinary high values of 230 and 360 cm/ka, respectively (Figure 2.2). In the glacial section, we are considering a constrained age model due to the lack of carbonate. Nevertheless, these high LSR are based on filtered background sediment sequences since turbidite deposits were clearly cut out (Figure 2.3 and supporting information). Sedimentation rates decreased to ~30 cm/ka between 12.5 and 9 cal ka BP, followed by continuous LSR of 17 cm/ka lacking any significant variability during the Holocene.

The Holocene sections reveal no turbidite beds. Turbidite deposition was restricted to the glacial/deglacial period and was accompanied by very high sedimentation rates of background sediments.

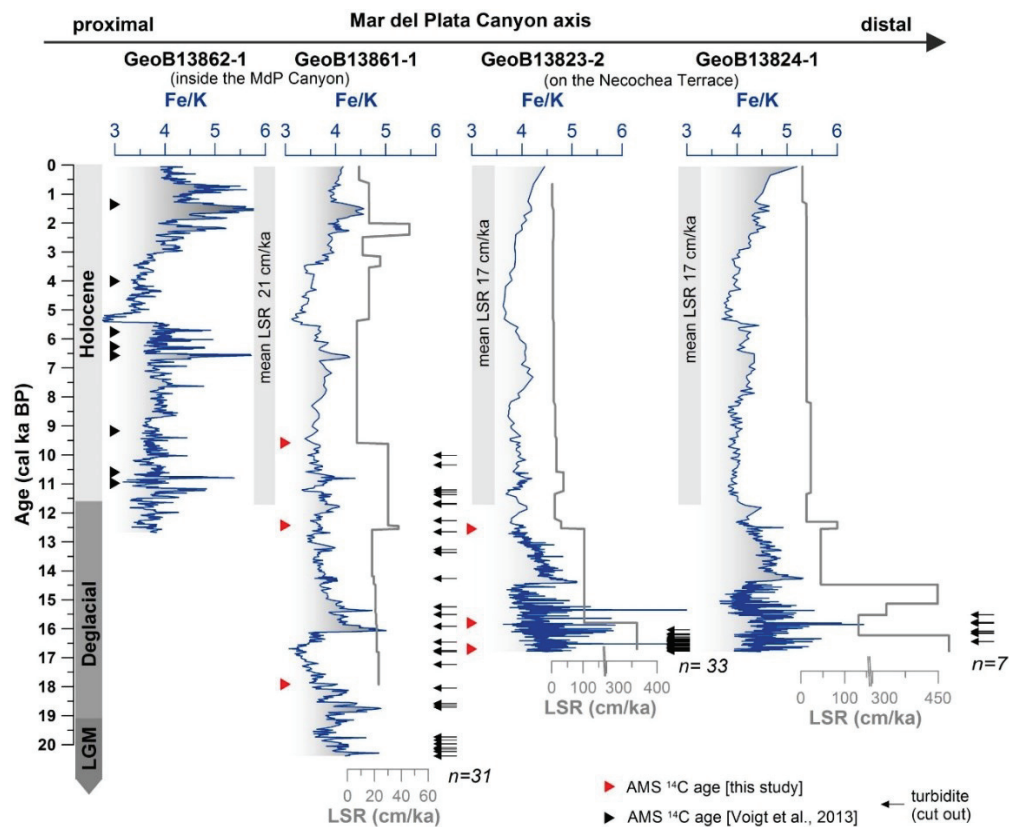


Figure 2.2: Stratigraphic correlation based on both calibrated AMS ^{14}C ages and down-core Fe/K records. Black and red triangles mark AMS ^{14}C ages (see legend). Note the different scales of the linear sedimentation rates (LSR). Grey dashed arrows imply the decreasing glacial to Holocene LSR trend. Turbidite beds (black arrows) were subtracted to reveal net background sedimentation, (n = total number of turbidites within investigated time period). Fe/K record from GeoB13862-1 from Voigt *et al.* [2013].

2.4.2 Sedimentological classification

All investigated sediment cores show consistent lithologies ranging from olive-brown muddy to sandy silt. Glacial sediments are stiff and compact. Microfossils are very rare to absent in glacial/deglacial sediments. Radiographs of the Holocene sections show enhanced bioturbation relative to glacial/deglacial sections.

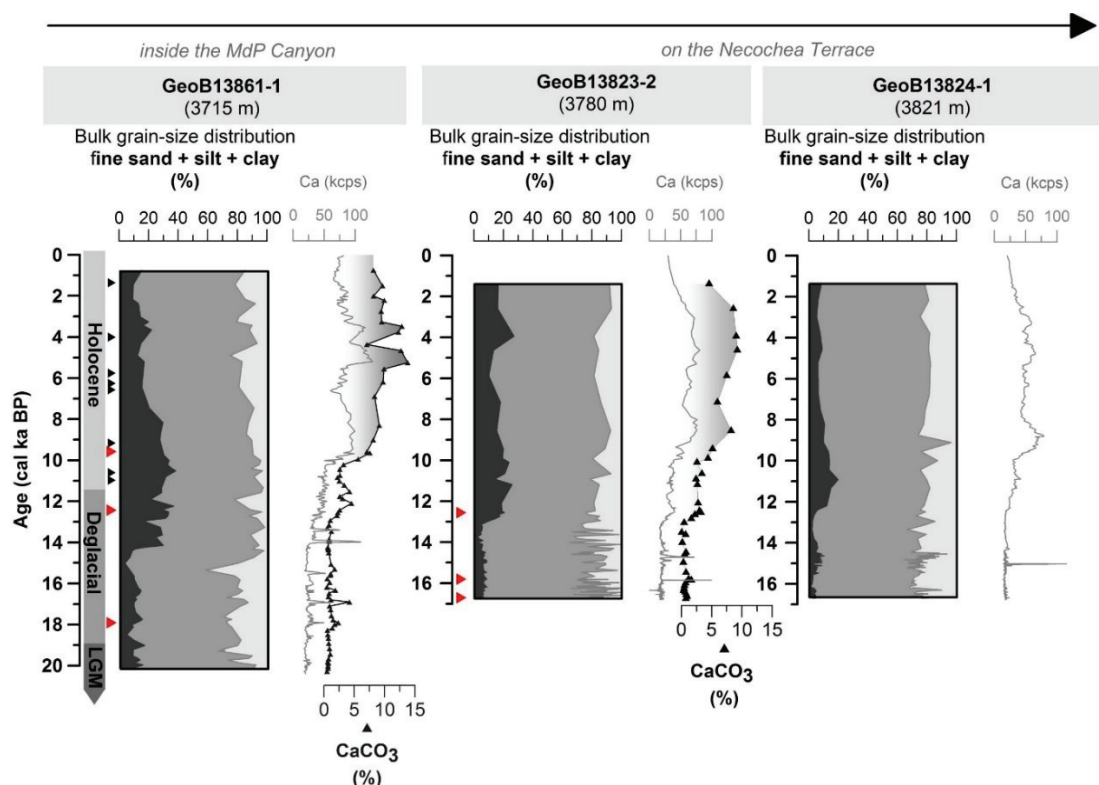


Figure 2.3: Bulk grain size distribution GeoB13861-1, GeoB13823-2 and GeoB13824-1, subcategorized in clay (< 2 μm), silt (2-63 μm) and fine sand (63-125 μm). AMS ^{14}C ages are labeled as triangles - red triangles: this study; black triangles were used to constrain all age models [Voigt *et al.*, 2013]. Calcium carbonate contents are plotted together with X-Ray Fluorescence Ca peak intensities (in thousand counts per second - kcps).

Core GeoB13861-1 (from the Mar del Plata Canyon) reveals lowest fine sand (63-125 μm) contents of about 11 % (69 % silt, 19 % clay) from 20 to 14 cal ka BP (Figure 2.3). The interval from 14 to 8 cal ka BP shows an increased fine sand content of ~ 30 % (62 % silt, 8 % clay) whereas the Holocene displays a decreased average value of 15 % fine sand (70 % silt, 15 % clay). Carbonate contents are less than 1 % (TOC 0.6-0.9 %) until 13 cal ka BP, increase from 13 to 10 cal ka BP, and reach 10-15 % carbonate (TOC 1.5 %) during the Holocene.

Grain-size composition of both cores from the Necochea Terrace (GeoB13823-2 and GeoB13824-1) show ~ 6 % fine sand (76 % silt, 17 % clay) from 17 to 13 cal ka BP (Figure 2.3). From ~ 13 to 8 cal ka BP we observed an abrupt increase of fine sand contents (18 % fine sand, 65 % silt and 16 % clay). The Holocene period is defined by a gradual reduction to 16 % fine sand content (69 % silt, 13 % clay). Between 17 and 13 cal ka BP, carbonate contents reach 0.9 % accompanied by 0.9 % TOC. Sediments from 13 cal ka BP to present reveal increased carbonate contents of ~ 10 %.

The sediments from the Necochea Terrace are generally finer (Figure 2.3) and show lower carbonate contents relative to the Mar del Plata Canyon core (i.e., GeoB13861-1). Measured biogenic opal contents constitute less than 5 % in all cores (not shown here).

2.4.3 Sortable silt

Sortable silt constitute 54-80 % of the total silt fraction in the cores (Figure 2.4a). From 20 to 14 cal ka BP (early deglacial) SS_{mean} and $SS\%$ data display millennial-scale variations. Calculated average SS_{mean} for this period is 25 μm for GeoB13861-1 and 22 μm for GeoB13823-2 and GeoB13824-1. In particular, from ~ 14 to 10 cal ka BP (late deglacial), all sediment cores reveal a remarkable increase in SS_{mean} values (Figure 2.4a). While the Mar del Plata Canyon core (GeoB13861-1) shows SS_{mean} values of 31 μm , both cores from the Necochea Terrace (GeoB13823-2 and GeoB13824-1) depict SS_{mean} values of 25 μm during that time period (Figure 2.4a). Hence, SS_{mean} maxima are more pronounced during the late deglacial than during the early deglacial. The Holocene sortable silt spectra at all sites reveal unimodal distributions and SS_{mean} values reveal smaller variations. Holocene SS_{mean} are 26 μm for GeoB13861-1 and 24 μm for GeoB13823-2 and GeoB13824-1. All cores show a positive $SS\%$ and SS_{mean} correlation coefficient (Figure 2.4b; GeoB13861-1, $R^2 = 0.75$; GeoB13824-1, $R^2 = 0.6$; GeoB13823-2, $R^2 = 0.2$).

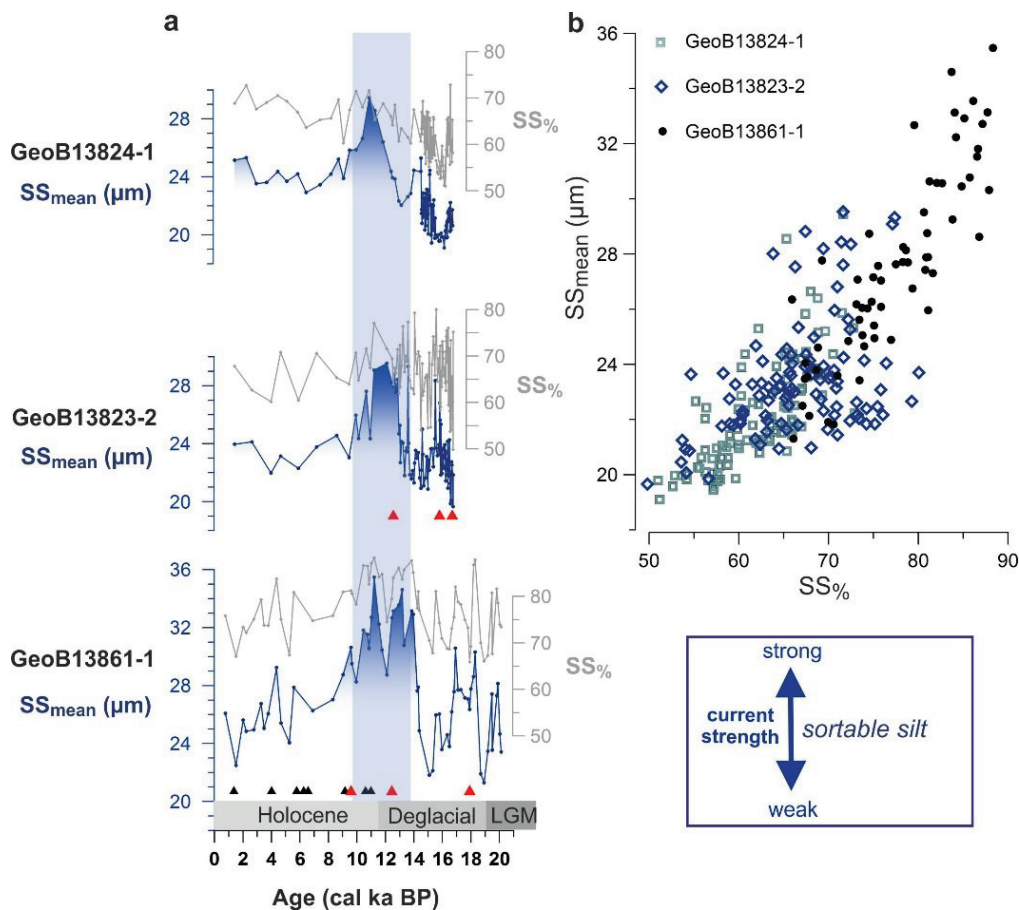


Figure 2.4: (a) Sortable silt grain-size data of GeoB13861-1, GeoB13823-2 and GeoB13824-1 for the last 20 ka. Red (this study) and black triangles [Voigt *et al.*, 2013] indicate AMS ^{14}C ages. Blue shaded vertical bar highlights last glacial/interglacial transition with rapid and steep increased sortable silt values in all three cores. (b) Scatterplot of sortable silt mean (SS_{mean}) and sortable silt percentage ($SS\%$).

2.4.4 Clay mineral assemblages

Cores GeoB13861-1 and GeoB13823-2 show ~ 10-20 % smectite, ~ 11-16 % kaolinite and ~ 25-35 % chlorite without remarkable glacial/interglacial variations (Figure 2.5a). Normalized kaolinite/chlorite peak area ratios (Kao/Chl) display values of ~ 0.2-0.5 and present no variations within the investigated interval (Figure 2.5b). Only from 10 to 5 cal ka BP GeoB13823-2 reveals minor variations, with slightly higher Kao/Chl values. Since 5 cal ka BP both data sets stabilize at a Kao/Chl ratio of 0.3. Illite is the main component with ~ 35-45 % recording a slight increase from the late LGM to the present (Figure 2.5a). Illite 5 Å/10 Å parameter reaches values of ~ 0.4 which represents a muscovite type, enriched in aluminum (i.e., Al-rich illite, Figure 2.5d). Illite integral breadths (IB) are characterized by 0.2-0.35 during the deglacial period which decrease to ~ 0.3 (GeoB13861-1) and ~ 0.35 (GeoB13823-2) in the Holocene sections (Figure 2.5c). Hence, the IB represents well crystallized illite. Smectite IBs reach ~1 displaying well crystallized smectite (Figure 2.5e).

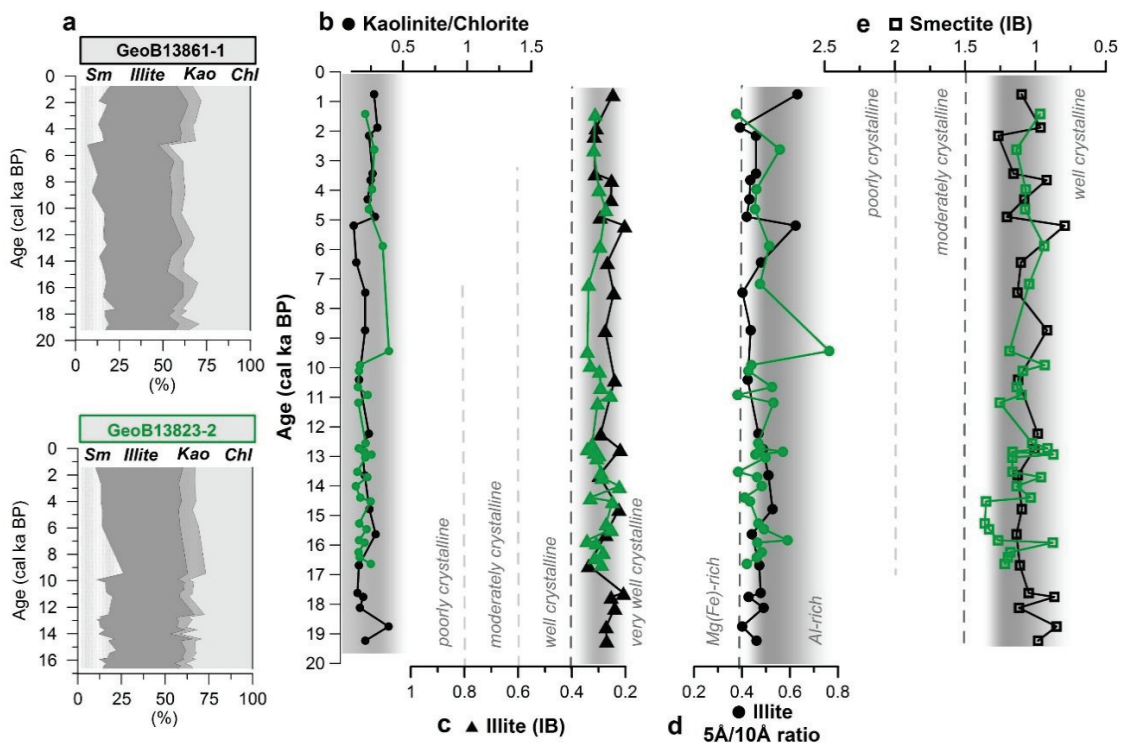


Figure 2.5: Clay mineralogy of sediment cores GeoB13861-1 (black) and GeoB13823-2 (green). **(a)** Percentages of smectite (Sm), illite, kaolinite (Kao), and chlorite (Chl). **(b)** Kaolinite/chlorite peak area ratio. **(c)** Illite crystallinity after *Diekmann et al.* [1996] (IB - integral breadth in $\Delta^2\theta$). **(d)** Illite 5 Å/10 Å peak intensity ratio after Esquevin [1969]. **(e)** Smectite crystallinity (IB) after Diekmann et al. [1996]. Vertical grey dashed lines indicate compositional intervals and vertical grey bars depict basic distribution.

2.5 Discussion

2.5.1 Sediment input along the deep Argentine continental margin

The detrital clay mineral composition of GeoB13861-1 and GeoB13823-2 show a dominance of Al-rich illite and chlorite (Figure 2.5) which according to *Diekmann and Kuhn* [1999] and *Walter et al.* [2000] indicate a persistent southern-sourced sediment input to our core sites over the last 20 ka. In addition, low and remarkably constant amounts of smectite and kaolinite are reported with comparable values at both core locations (Figure 2.5a). Low and constant Kao/Chl ratios (Figure 2.5b) are a result of only minor kaolinite supply from the equatorial regions (Figure 2.1a) [*Petschick et al.*, 1996]. Illite IBs and elemental compositions show minor variations during the deglacial period and the Holocene. Overall superior crystallinity of illite is indicative for low intensities of chemical weathering. Illite is structurally considered as Al-rich (muscovitic) and indicates a source located in the circumantarctic area, southernmost South America or the southern Pacific delivered through the Drake Passage via the ACC [*Diekmann et al.*, 1996; *Petschick et al.*, 1996]. Hence, we suggest a direct and strong influence of deep SCW and a nearly persistent terrigenous sediment supply along the Argentine continental margin. A slightly decreased SCW influence (or a slightly increased NCW influence) may have occurred since the early Holocene for the distal core and for both cores since the late Holocene (Figure 2.5b and 2.5d).

Lantzsch et al. [2014] also referred to the southern sourced delivery along the Necochea Terrace using bulk sediment neodymium isotope (ϵ_{Nd}) measurements from sediment core GeoB6308-3 at about 3600 m water depth as a source proxy. Here, bulk ϵ_{Nd} values (-2.7 to -4.2) are characteristic for the Argentine margin signal and contrast with the southern Brazilian margin signal (-9.3) [*Mahiques et al.*, 2008]. Thus, ϵ_{Nd} bulk measurements [*Lantzsch et al.*, 2014] and clay mineral assemblages (this study, Figure 2.5) support the persistent northward transport of terrigenous sediments by LCDW and AABW along the Necochea Terrace at the deep Argentine continental margin.

A glacial expansion of deep SCW [e.g., *Freeman et al.*, 2016; *Lund et al.*, 2015] and corresponding upward shift of the LCDW/AABW interface above our core sites may have caused a glacial decline in the flow regime at about 3750 m water depth. A subsequent deepening of the high energetic LCDW/AABW interface to the depth range of our core sites during the late deglacial would have resulted in increased flow strength (*Preu et al.*, 2013), accompanied by a reduction of sediment deposition (Figure 2.2). During the Holocene decreased grain size (Figure 2.3) indicate the downward migration of the NCW/SCW as well as the LCDW/AABW interface due to the re-initiation and the slightly enhanced influence of the modern NADW [e.g., *Böhm et al.*, 2015;

Lynch-Stieglitz et al., 2007]. This downward migration was accompanied by a relatively weak deep SCW flow (Figure 2.4a). Such a slightly enhanced NCW influence is supported by increased Kao/Chl values in GeoB13823-2 during the early Holocene and more balanced Kao/Chl and Illite IBs in both cores during the late Holocene (Figure 2.5). However, the Holocene changes in the Kao/Chl and Illite IBs values are rather small and still support a predominant SCW influence.

The proposed changes in the vertical water mass structure support the construction of contourite terraces at the Argentine continental margin suggested by *Hernandez-Molina et al.* [2009] and *Preu et al.* [2013]. They indicate that the interplay between the margin physiography and the local bottom current regime plays an essential role for terrace formation and argue that locally confined velocity maxima might lead to enhanced erosion forming a contour channel at the transition between steep slope and terrace. The resultant resuspended material is transported along the terrace. Once the terrace reaches a certain extent, sediment deposition at the seaward limit becomes possible to set up elongated drifts [*Preu et al.*, 2013]. *Preu et al.* [2013] suggested an upward displacement of the LCDW/AABW interface by glacial AABW thickening close to the Necochea Terrace and thus, propose contourite terrace formation processes acting during glacial periods.

2.5.2 Carbonate content and preservation – Hints for spatial and temporal variations in Southwest Atlantic deep-water mass structure?

The lack of carbonate in most of the studied samples from the late LGM and early deglacial sections (Figure 2.3 and 2.6c), may be related to strong corrosion of carbonate and/or very low carbonate production in surface waters. The increase of carbonate contents (from less than 1 % to up to ~10 %, GeoB13823-2) in the sediment sections of all three cores starts at 13 cal ka BP (Figure 2.6c). The carbonate enrichment might be due to increased preservation and/or supply of carbonate during the past 13 cal ka BP.

The extraordinary low carbonate content at the late LGM and early deglacial sections of our cores (Figures 2.3 and 2.6c) is consistent with a considerably shallow NCW that is not admixed in significant amounts deeper than 3750 m in the Southwest Atlantic. In this context, well-ventilated and CO_3^{2-} saturated NADW allows for well-preserved carbonate records while deep SCW is undersaturated in CO_3^{2-} and displays signs of strong carbonate corrosion [*Henrich et al.*, 2003]. Hence, carbonate free sections from 20 to 13 cal ka BP most likely reflect a weakened deep NCW contribution. Furthermore, the high LSR may point to a dilution of carbonate due to increased terrigenous supply during the glacial period.

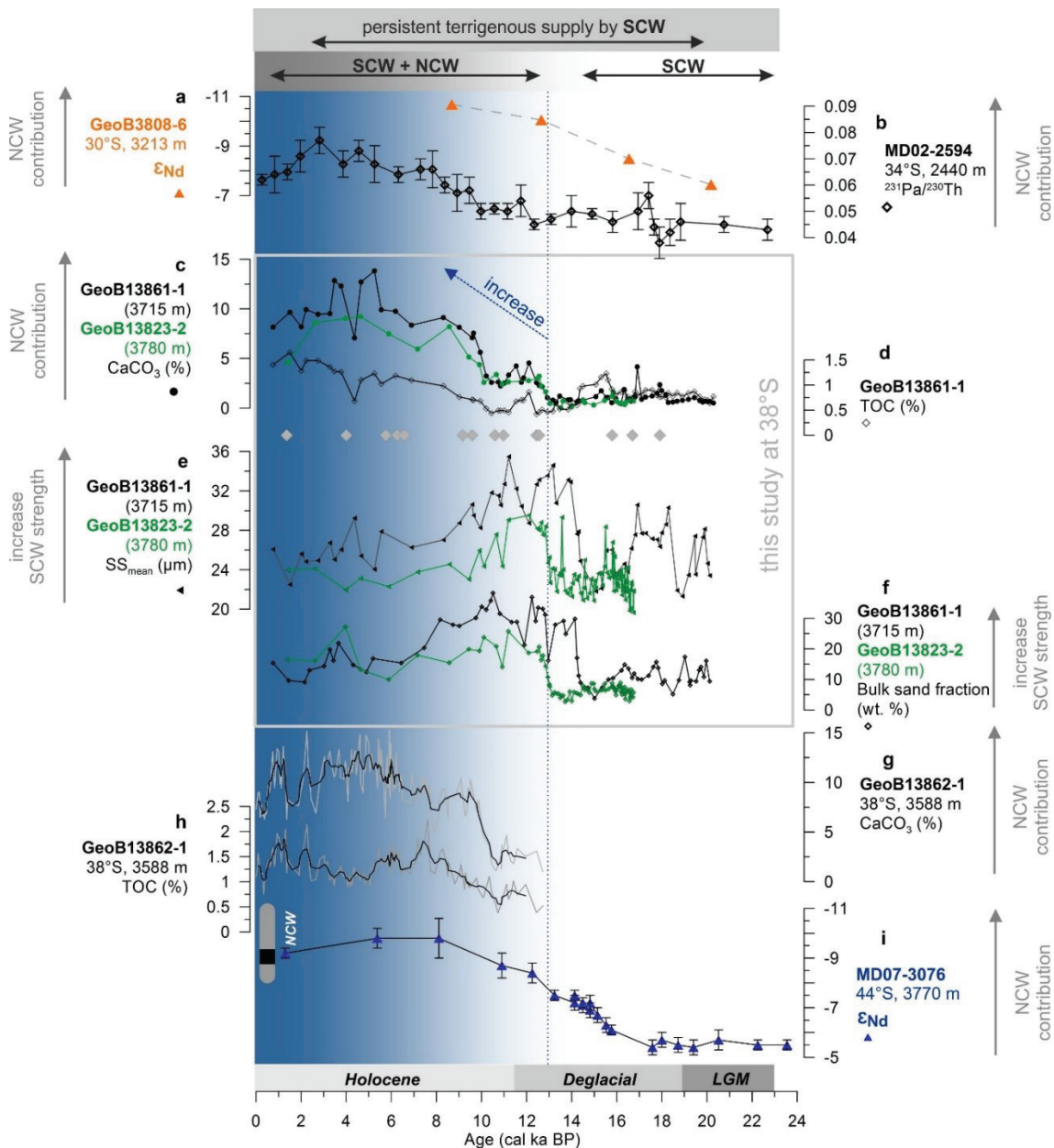


Figure 2.6: Multi-proxy records from the Southwest Atlantic. **(a)** Leachate ϵ_{Nd} from GeoB3808-6 on the mid-Atlantic Ridge in the South Atlantic [Jonkers *et al.*, 2015]. **(b)** $^{231}\text{Pa}/^{230}\text{Th}$ from core MD02-2594 from Cape basin [Negre *et al.*, 2010]. **(c)** Calcium carbonate (CaCO_3) and **(d)** total organic (TOC) content from cores GeoB13823-2 and GeoB13861-1 (this study). Grey rhombuses indicate AMS ^{14}C ages. **(e)** Sortable silt mean (SS_{mean}) and **(f)** bulk sand fraction from cores GeoB13861-1 and GeoB13823-2 (this study). **(g)** CaCO_3 and **(h)** TOC content from GeoB13862-1, also located within the Mar del Plata Canyon, but slightly shallower than our cores [Voigt *et al.*, 2013]. **(i)** Benthic foraminifera ϵ_{Nd} with 2σ uncertainties [Skinner *et al.*, 2013] from core MD07-3076, located on the eastern flank of the Mid-Atlantic Ridge in the sub-Antarctic South Atlantic. Vertical grey bar (left side) shows modern ϵ_{Nd} water mass composition in > 3000 m water depth [Stichel *et al.*, 2012]. Periods of deep Southern Component Water (SCW) and deep SCW + Northern Component Water (NCW) influences in our core sites are indicated in the top of the panel. The blue arrow implies a rise of NCW contribution reflected in enhanced CaCO_3 content in our cores (c) and supported by other proxy data (a, b, g).

However, changes in primary production are an additional factor controlling carbonate contents. Where primary production is high, it is expected that larger proportions of organic carbon produced by photosynthesis settle down from surface layer and bottom respiration takes up oxygen [Berger *et al.*, 1989]. However, our deep core sites in the Mar del Plata Canyon are not directly influenced by high-productivity regions, i.e., upwelling areas in the eastern Atlantic, where nutrient-enriched waters create a significant high productivity regime [Fischer *et al.*, 2000]. In addition, the La Plata River derived waters are shifted to the north along the continental shelf, fertilizing the Uruguayan and Brazilian shelf waters [i.e., Voigt *et al.*, 2013]. The low total organic carbon content at our core sites (Figure 2.6d and h) presents a significant increase of 0.5 (glacial) to 1.0 (interglacial). Thus, surface productivity driven changes in carbonate contents are not negligible, but subordinate compared to the high corrosion potential of deep SCW.

Reduced carbonate contents could also be a result of a sluggish deep SCW flow during the late LGM/early deglacial, rendering deep SCW more corrosive due to enhanced remineralization of organic matter. However, Howe *et al.* [2016] also suggested that there was a greater proportion of southern-sourced waters in the deep Atlantic (below 2500 m water depth) during the LGM relative to the Holocene. Our data also point to a reduced proportion of glacial deep NCW in the study area and a deep SCW dominance in agreement with other studies [Böhm *et al.*, 2015; Howe *et al.*, 2016; Lippold *et al.*, 2016; Rutberg *et al.*, 2000]. Indeed, Howe *et al.* [2016] calculated ~15 % (~25 %) NCW contribution at 3700 m water depth during the LGM (Holocene).

Importantly, our records suggest that the increase in carbonate contents (and enhanced NCW influence) already started during the late deglacial. In turn, the carbonate increase testifies to enhanced water mass ventilation that reduces water mass corrosiveness at 3750 m water depth (Figures 2.3 and 2.6c to 6g). Hence, we assume that increased carbonate contents in the Holocene sections of our cores reflect a mixture of deep SCW and well-ventilated, nutrient-depleted NADW rather than a major rise in surface primary productivity.

Since 13 cal ka BP, the increased contribution of NCW to the bottom of the water column at our core sites (~ 3750 m) enhances the preservation of planktonic foraminifera (e.g. *G. inflata*, *G. bulloides*), which settle down from surface waters. Because of their rather large sizes they are less susceptible to lateral transport [Mollenhauer *et al.*, 2006]. Consequently, the enhanced contribution of well-ventilated NCW may keep carbonate contents relatively high (Figure 2.6c and g). In addition, advection of terrigenous material by Holocene deep SCW flow was reduced accounting for a decreased dilution of carbonates.

Our findings of a dominant deep SCW flow during the late LGM and early deglacial period and an enhanced influence of NCW since 13 cal ka BP (Figure 2.6c), which persisted during the Holocene, are coherent with results from studies using ϵ_{Nd} from South Atlantic sites [Jonkers *et al.*, 2015; Negre *et al.*, 2010; Skinner *et al.*, 2013]. ϵ_{Nd} are suggested to be quasi-conservative water mass tracers since the values reflect changes in the spatial distribution of distinct water masses [Goldstein and Hemming, 2003]. ϵ_{Nd} values separate the ocean into two broad geochemical end members [Skinner *et al.*, 2013].

A core (GeoB3808-6) collected at 30°S and 3213 m water depth is currently under the influence of NADW, being situated just above the deep SCW [Jonkers *et al.*, 2015; Figure 2.6a]. However, glacial ϵ_{Nd} (-8 to -7) data based on sediment leachates, show modern AABW values [Jonkers *et al.*, 2015] and indicate deep SCW dominance as a basin-scale predominance in the abyssal glacial Southwest Atlantic [Duplessy *et al.*, 1988; Sarnthein *et al.*, 1994]. At the beginning of the Holocene, ϵ_{Nd} leachate values indicate a more pronounced, but not entirely dominated presence of NCW (-10.5) at this location [Jonkers *et al.*, 2015; Figure 2.6a]. Generally, pure NADW ϵ_{Nd} in the North Atlantic ranges around -13.5 [Jeandel, 1993].

The down-core ϵ_{Nd} record based on benthic foraminifera of MD07-3076 from 44°S and 3770 m water depth [Skinner *et al.*, 2013] also implies a deep SCW composition during the early deglacial period (Figure 2.6i). Starting at ~ 17 cal ka BP, ϵ_{Nd} values gradually decrease pointing toward a deglacial increase in the presence of NCW at 3770 m water depth. Although our data reveal that carbonate contents increase starting at 13 cal ka BP with a second rise at 10 cal ka BP, Skinner *et al.* [2013] suggest an increased NCW contribution already at ~ 17 cal ka BP (Figure 2.6i). An approximate 4 ka - delay is interpreted as a result of a successive change in deep water properties, i.e., water mass adjustment, caused by a NCW influence on water mass chemistry at about 3750 m water depth. Furthermore, MD07-3076 is located in the centre of the basin at the eastern flank of the Mid-Atlantic Ridge, where the western boundary current is absent. In the centre of the basin, the NCW might affect carbonate preservation first and then spreads out. Hence, CO_3^{2-} enrichment justified by NCW contribution would lead to enhanced carbonate preservation at our core sites at the Argentine continental margin with a delay of ~4 ka.

However, this delay is not represented by the $^{231}\text{Pa}/^{230}\text{Th}$ data from Negre *et al.* [2010], but the data support our hypothesis that the dominance of glacial deep SCW flow increased carbonate dissolution in the deep South Atlantic. This $^{231}\text{Pa}/^{230}\text{Th}$ record (Figure 2.6b) reflects the presence of abyssal waters depleted in ^{231}Pa owing to opal scavenging and leaving the Southern Ocean to ventilate the deep Atlantic. The glacial values are below production ratios at other North Atlantic sites which were hitherto interpreted to reflect vigorous flow from North Atlantic sources

[McManus *et al.*, 2004; Roberts *et al.*, 2010]. Thus, low glacial ratios are a result of a northward flow of low ^{231}Pa waters [Negre *et al.*, 2010] and confirms $\delta^{13}\text{C}$ and Cd/Ca data reflecting nutrient-rich bottom waters at deep core sites in the South and North Atlantic during the LGM [Curry and Oppo, 2005; Marchitto and Broecker, 2006; Lynch-Styglitz *et al.*, 2007]. This is a new approach since previous interpretations did not consider that ^{231}Pa scavenging in the Southern Ocean affects the ^{231}Pa imprint of SCW [Keigwin and Boyle, 2008; McManus *et al.*, 2004]. Consequently, this glacial deep SCW flow increased carbonate dissolution in the deep South Atlantic until NCW was re-initiated enhancing $^{231}\text{Pa}/^{230}\text{Th}$ ratios as well as carbonate content (Figure 2.6b and c).

2.5.3 Changes in deep SCW strength since the Last Glacial Maximum

Given that the terrigenous input to our core sites is predominantly influenced by deep SCW, we are able to reconstruct relative changes in deep SCW flow strength (Figure 2.4a) using the sortable silt paleo-current proxies [McCave, 2008]. Terrigenous SS_{mean} and $SS_{\%}$ are positively correlated (Figure 2.4b), which is a strong argument for primarily current-controlled grain size changes [McCave *et al.*, 2014].

Early deglacial sortable silt values are generally lower than late deglacial values and show only minor variability, even in core sections that are influenced by turbidites (note that the turbidite beds were excluded from the records, as described in section 2.4.1 and the supporting information). This period is accompanied by very low (< 10 %) sand content (Figure 2.6f) implying weaker current strength and thus, enhanced deposition of fine sediments (Figure 2.4a). During this period the glacial deep SCW is generally formed through widespread occurrence of polynyas along the Antarctic continental margin and accompanied brine rejection [Smith *et al.*, 2010], since lowered sea levels and grounded ice shelf lead to a reduction of the Antarctic ice shelf. The reduction in dense ISW export further implies a decline in SCW formation [Marshall *et al.*, 2007].

An event-like, rapid and steep increase in SS_{mean} and $SS_{\%}$ occurred at ca. 14 cal ka BP and lasted until 10 cal ka BP (Figures 2.4 and 2.6e). The increase indicates relatively enhanced current strength and thus, a strong deep SCW flow along the Necochea Terrace during this time interval (Figure 2.7a) which resulted in enhanced sand transport (Figure 2.6f). The sortable silt proxies show low values during the early deglacial, and high values during the late deglacial period, suggesting an unstable and fluctuating glacial deep-water flow [Howe and Pudsey, 1999] due to differences in SCW spreading.

This feature is pervasive to all our cores and suggests a considerable increase in deep SCW flow during the late deglacial. Our data is supported by low $^{231}\text{Pa}/^{230}\text{Th}$ values in the South Atlantic indicating northward flow of low ^{231}Pa waters from the Southern Ocean [Negre *et al.*, 2010; Figure 2.6b]. On the one hand, a global sea level rise during the last deglacial period would effectively enhance the ISW Mode (i.e., expansion of Antarctic ice shelves) contribution to deep SCW formation [Krueger *et al.*, 2012], leading to a late deglacial increase in deep SCW flow strength.

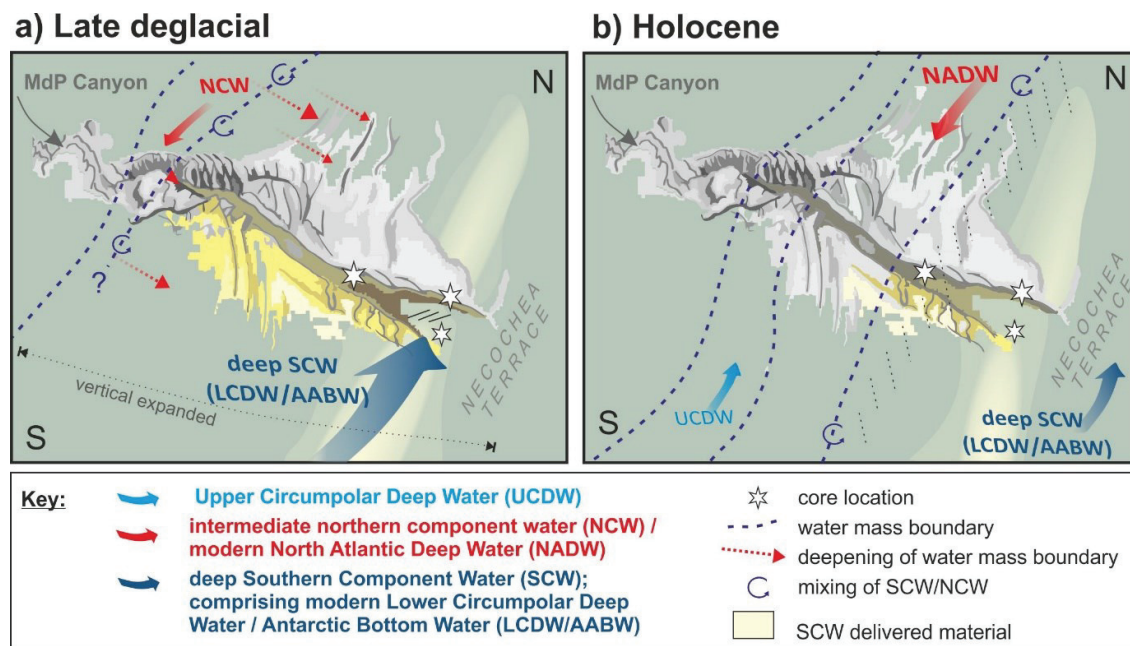


Figure 2.7: Block diagrams showing the spatial distribution and flow strength of southern component water (SCW) at the distal Mar del Plata (MdP) Canyon and along the Necochea Terrace during the late glacial (a) and the Holocene (b). Arrow sizes illustrate current strength. White stars indicate the location of the investigated cores inside the MdP Canyon and on the Necochea Terrace. **(a)** Late deglacial period with enhanced deep SCW current strength resulting in a general grain-size increase and low linear sedimentation rates at our core sites. Deep SCW current strength may increase due to the transition of an intermediate to a deep northern component water leading to a reduction of deep SCW expansion. We also suggest that the Lower Circumpolar Deep Water/Antarctic Bottom Water (LCDW/AABW) interface migrated downward during the early deglacial. Hence, it was located close to our core sites during the late deglacial and caused increased sortable silt values associated to increased current strength. **(b)** Holocene with moderate and stable deep SCW flow. Deepened CO_3^{2-} -saturated NADW (2000-3000m, Stramma and England [1999]) may have resulted in changing deep-water properties and thus, in increased carbonate contents at our core sites (3750 m).

On the other hand, enhanced deep SCW flow strength could have been triggered by re-initiation of the modern NADW [e.g., Lynch-Stieglitz *et al.*, 2007] at 2000-3000 m water depth [Stramma and England, 1999] narrowing vertically the deep SCW spatial distribution. This would have shifted the LCDW/AABW interface, a high energetic zone of increased current strength, downward in the water column (Figure 2.7a). We suggest that the LCDW/AABW interface was placed

above our core sites during the early deglacial, in the range of our core sites during the late deglacial and below our core sites during the Holocene (Figure 2.7a and 2.7b).

Since approximately 10 cal ka BP, decreased but stable SS_{mean} values and a decline in fine sand contents (Figure 2.6f) indicate a stabilized and weakened deep SCW circulation which became less vigorous along the Necochea Terrace. In addition, *Negre et al.* [2010] have shown that increased Holocene $^{231}\text{Pa}/^{230}\text{Th}$ values (Figure 2.6b) are a result of a decreased northward flow of low ^{231}Pa waters. Decreased flow strength also implies a deepened LCDW/AABW interface below our core sites and deep SCW production without large fluctuations (Figure 2.6e and 2.7b). Additionally, a contribution of NADW to the core sites at the deep Argentine continental margin was larger during the Holocene than during the glacial/early deglacial [*Curry and Oppo, 2005; Freeman et al., 2016; Menviel et al., 2016; Oppo and Curry, 2012; Skinner et al., 2013*]. Thus, slightly enhanced NCW contribution influencing water mass properties around 3750 m water depth at the Argentine continental margin found in recent times were first observed around 10 cal ka BP.

2.6 Conclusions

Here we present for the first time AMS ^{14}C based age models going back to the LGM for three sediment cores in the range of the deep SCW (comprising the LCDW/AABW) at the deep Argentine continental margin.

Based on clay mineral compositions we propose that the terrigenous sediments along the Necochea Terrace were exclusively delivered by a persistent northward-flowing deep SCW nepheloid layer that set up continuous contourite drift deposits.

Coherent changes in sortable silt and bulk grain-size data for the three cores offer systematic information about deep SCW circulation and flow strength during the last 20 cal ka BP. Our data suggest increased deep SCW flow strength from 14 to 10 cal ka BP, but no remarkable glacial/interglacial change. Thus, we propose an increased deep SCW flow as a response to enhanced production rate of AABW or, more probable, as a result of modern (deep) NADW reinitiation narrowing the deep SCW spreading. This was accompanied by a vertical migration of the LCDW/AABW interface, which was in the range (above) of our core sites during the late deglacial (early deglacial), and shifted further downwards during the Holocene influencing drift deposition.

Taking advantage of corrosive deep SCW, we propose that very low to absent carbonate contents during the glacial and early deglacial as well as increased carbonate contents during the

late deglacial and Holocene, give evidence for a downward shift of the deep SCW/NCW interface. Between 20 and 13 cal ka BP, we suggest the presence of an intermediate NCW that left space for deep SCW expansion reducing carbonate preservation at our core sites. Only from 13 cal ka BP on, the deep SCW/NCW interface migrated downward in the water column. This shift changed deep-water chemistry enhancing carbonate preservation around our core sites (~ 3750 m water depth).

Acknowledgments

We acknowledge Rainer Petschick, an anonymous reviewer and Associate Editor Helen Bostock for their helpful comments which significantly improved the content of this manuscript. This study was funded through the DFG-Research Center/Cluster of Excellence “The Ocean in the Earth System” (MARUM) and was supported by GLOMAR – Bremen International Graduate School for Marine Sciences. We acknowledge T. Schwenk for re-processing the bathymetric data and S. Krastel for comments and discussion which improved the content of this manuscript. We thank B. Kockisch, J. Marquardt and J. Klinckradt for lab assistance. We thank S. Wiebe and R. Fröhlking (AWI Bremerhaven) for assistance during sample preparation and supply of clay mineral XRD measurements. This research used data acquired at the XRF Core Scanner Lab at the MARUM – Center for Marine Environmental Sciences, University of Bremen. In this respect we thank U. Röhl and her team for assistance. We thank the ETH Zürich for AMS radiocarbon dating of small samples and in particular L. Wacker for collaboration. C. M. Chiessi acknowledges the financial support from FAPESP (grant 2012/17517-3), CAPES (grants 1976/2014 and 564/2015) and CNPq (grants 302607/2016-1 and 422255/2016-5). G. Kuhn acknowledges the Alfred Wegener Institute (AWI) Helmholtz Center for Polar and Marine Research program “Polar Regions and Coasts in the changing Earth System” (PACES II). Special thanks go to Captain and crew of RV Meteor during cruise M78/3. The new data reported in this paper are archived in PANGAEA (doi:10.1594/PANGAEA.874957).

Supporting information

Turbidite Identification and Age Model Preparation

Turbidite beds were identified intersecting the background sedimentary record in the three investigated cores GeoB13861-1, GeoB13824-1 and GeoB13823-2 based on structural features, colour, grain-size distribution and composition. The investigated sediments and corresponding radiographic images reveal clear contacts between the bottom of dark grey sandy turbidite deposits and the bioturbated to homogenous and structureless olive-brown sandy-, coarse- and muddy background sediments (Figure 2.SI 1). Above the contact, we observed a systematic increase in percentage of fine sand (63-250 μm). The top of the turbidite beds is either gradual or sharp, and in both cases identifiable from radiographic images.

Based on careful assessment of radiographs, the following standard sedimentary sequence was observed within turbidite beds: (1) grey to dark grey micro-cross bedded (mc) or sub-mm sized parallel-laminated (ml) very fine sand, (2) overlain by laminated very fine sands and silts, which are occasionally modified by convolute lamination (cl) and (3) sporadically homogenous mud layer (Figure 2. SI 1). Thus, specific units [Bouma *et al.*, 1962] can be characterized and classified as T_C , T_D and T_E divisions, respectively (Figure 2.SI 1). Coarser units of the lower Bouma-Sequence [Bouma *et al.*, 1962; Shanmugam, 1997] are not present. Exceptionally, several turbidite beds are coupled. The thickness of individual turbidite beds varies from a few to 10 cm. Thus, a specific decoupling of turbidite and background sediment distribution was possible, since the background sediment succession is essential to generate an age model. The comparison between turbidite beds with background sediment grain-size composition (Figure 3, main text) allowed the distinction between along- and down-slope delivered sediments. Based on this, we subtracted 134 cm, 129 cm and 9 cm in total of down-slope derived material from cores GeoB13861-1, GeoB13823-2 and GeoB13824-1, respectively.

Age models for the three cores are based on the hemipelagic background sediments. All turbidite beds were cut out on their non-erosive base and their upper contact identified from grain-size data, color and internal structure in radiographs, as described above. Hence, AMS ^{14}C age points were transferred into the resulting new (net) core depth records [Henrich *et al.*, 2010]. GeoB13862-1 (8 AMS ^{14}C ages) serves as a detailed stratigraphic reference site. Thus, the GeoB13862-1 X-Ray Fluorescence Fe/K record of hemipelagic background sediments was used to correlate specific Fe/K tie points with GeoB13861-1, GeoB13823-2 and GeoB13824-1 until 11 cal ka BP (Figure 2.SI 2). Because sediment sections older than 11 cal ka BP are almost void of carbonate due to the corrosion of deep southern component water masses in all cores [Volbers

and Henrich, 2002], all deeper sections were correlated using Fe/K background sediment records of all three cores investigated in this study constrained by five AMS ¹⁴C ages (Figure 2.SI 2).

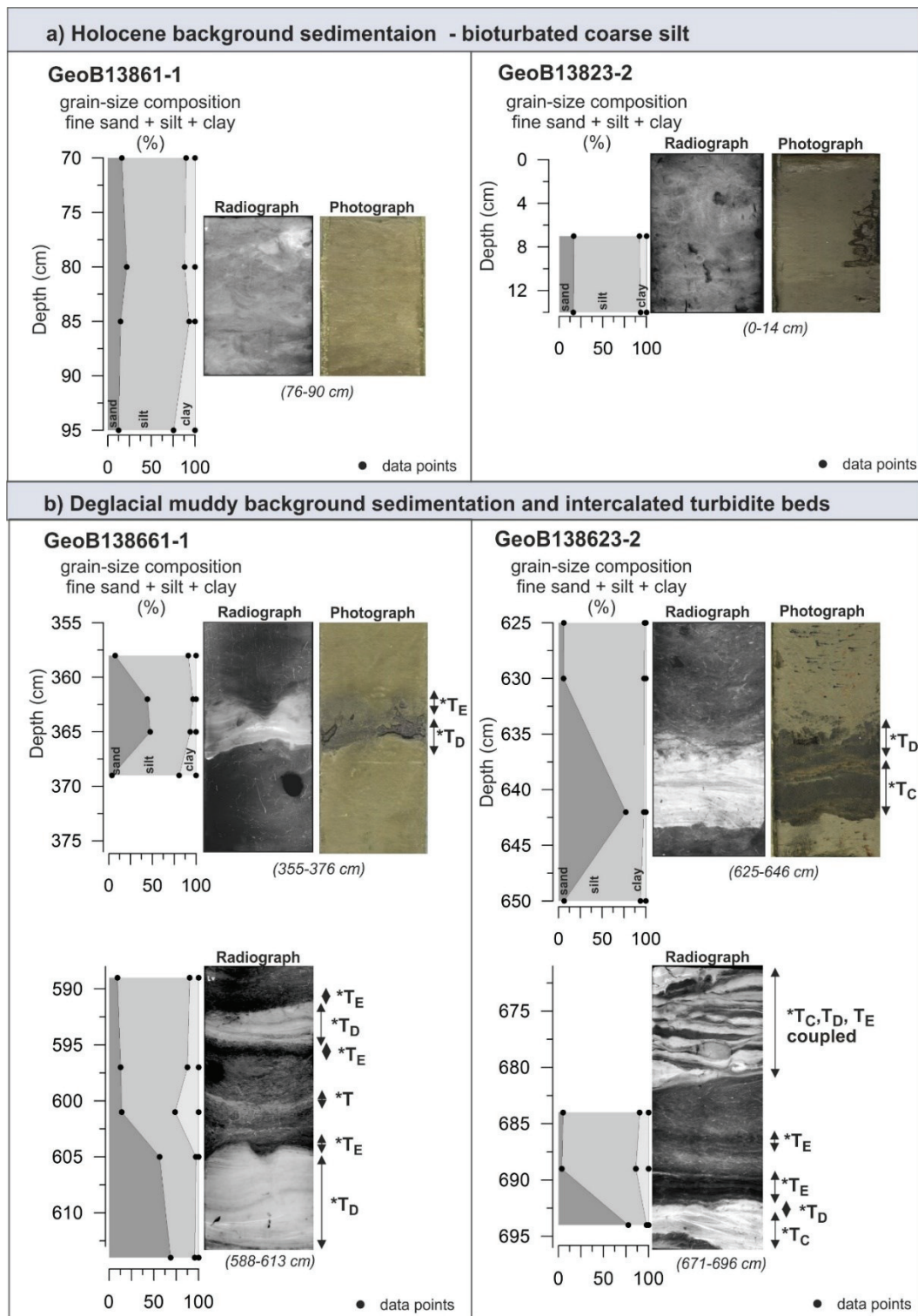
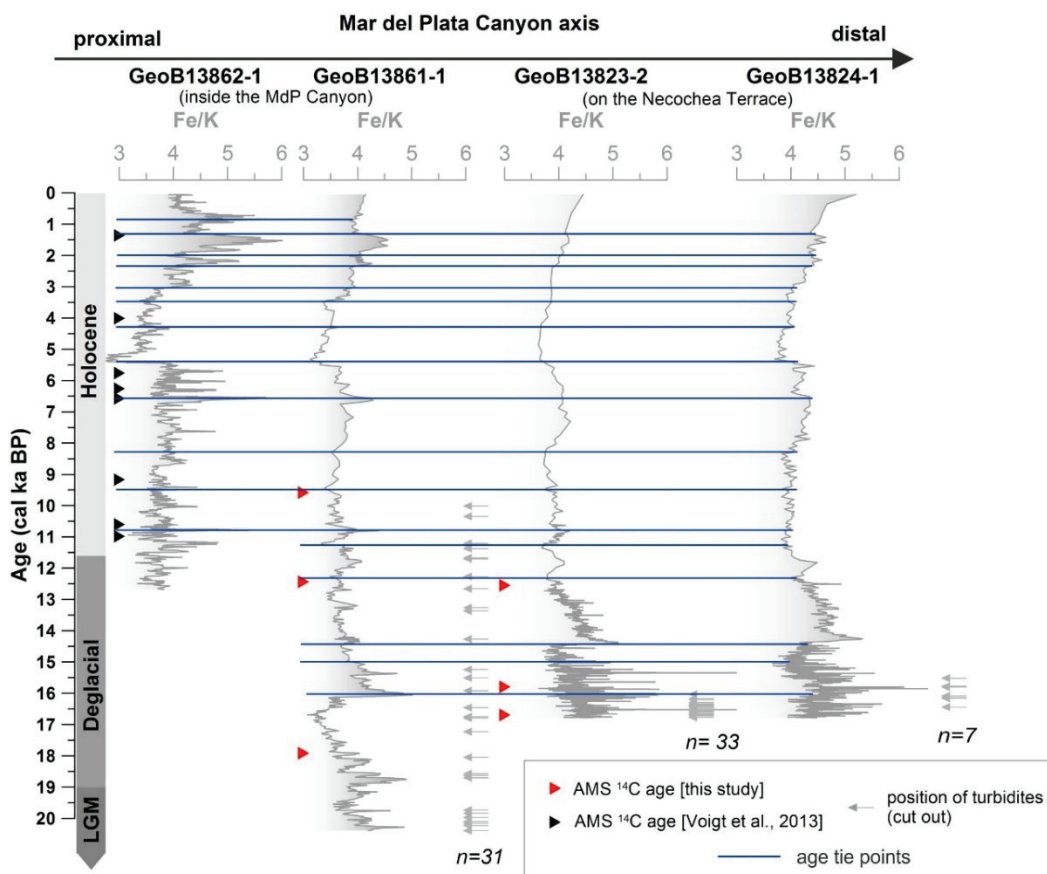


Figure 2.SI 1: Examples for classification of homogenous background sediments and turbidite beds showing specific internal structures based on grain-size data, radiographs and core photographs (T_C, T_D, T_E



classification based on *Bouma et al.* [1962]). Based on this classification turbidites were defined and cut out of the sedimentary record.

Figure 2.SI 2: Age model reconstruction based on eight AMS ¹⁴C ages of GeoB13862-2 [*Voigt et al.*, 2013; black triangles], as a reference site, and six AMS ¹⁴C ages of GeoB13861-1 and GeoB13823-2 (red triangles). Turbidite beds were cut out of the records, but their temporal distribution is depicted with grey arrows in the Fe/K record used for tie point correlation (blue lines).

Chapter 3

Interaction of a deep-sea current with a blind submarine canyon (Mar del Plata Canyon, Argentina)

**Grit Warratz¹, Tilmann Schwenk¹, Ines Voigt¹, Graziella Bozzano², Rüdiger Henrich¹, Roberto
Violante², Hendrik Lantzsch¹**

¹ University of Bremen, MARUM – Center for Marine Environmental Sciences and Faculty of Geosciences,
Klagenfurter Straße 4, D-28359 Bremen, Germany

² División Geología y Geofísica Marina, Departamento Oceanografía, Servicio de Hidrografía Naval, Montes de Oca
2124, C1270ABV Buenos Aires, Argentina

- Manuscript submitted to Sedimentology (02 August 2017)-

Abstract

The Mar del Plata (MdP) Canyon at the Argentine continental margin is incorporated into a major contourite depositional system, built by the incursion of southern-sourced water masses affecting the seafloor at different water depths. This study gives new insights into contourite-turbidite interactions in mid-slope (blind) canyons, which do not have a connection to the shelf or an onshore river system. Three sediment cores were obtained along the MdP Canyon thalweg and from the distal northern flank covering the last 20,000 years. Turbidity-current activity within the MdP Canyon was limited to the Last Glacial Maximum (LGM) until the late deglacial, whereas it was totally absent during the Holocene. During the LGM and early deglacial, turbidites reached both the proximal sector and the distal northern flank. During the late deglacial only the proximal sector was covered by turbidite deposition. Slope morphology and similarities in mineralogy and grain-size data between turbidite sands and contouritic sediments from the mid-slope Ewing Terrace indicate that turbidity currents originated from the mid-slope region. Furthermore, specific knickpoints observed in the uppermost thalweg acted as hydraulic jumps to accelerate turbidity currents. Thus, glacial turbidity-current activity resulted from instabilities due to increased sedimentation along the Ewing Terrace that was most probably favored by a shallowed and/or enhanced glacial Antarctic Intermediate Water (AAIW) nepheloid layer. During the late deglacial, a displacement or limited AAIW nepheloid layer resulted in less sedimentation along the Ewing Terrace restricting turbidite deposition to the proximal sector. In conclusion, contourite-turbidite interactions provide valuable information on variations in thermohaline circulation, i.e., AAIW distribution and strength, and highlight its impact on slope stability.

3.1 Introduction

Submarine canyons are incised into the continental shelf and/or slope and act as conduits for sediment transfer from continents to the deep sea [Nittrouer and Wright, 1994]. Thus, canyons give insights into the geological evolution of continental margins [Piper, 2005; Harris and Whiteway, 2011]. Harris and Whiteway [2011] recently discussed that largest canyons are commonly incised into the continental shelf or may even have a direct connection to modern terrestrial fluvial systems, but that some canyons terminate on the slope, defined as so-called “blind” canyons.

Mass wasting events and turbidity currents within shelf-incising and river-connected canyons are most commonly triggered by sea level changes [Wien et al., 2006; Liu et al., 2016]. These gravity-driven processes are suggested during sea-level lowstand and rise when gullies on the uppermost slope were rapidly filled and released turbidity currents [e.g., Wien et al., 2006; Henrich et al., 2010; Pierau et al., 2010]. Controversy, also distinct periods of sea-level highstand display turbidity current activity, i.e., due to high sediment supply by undercurrents moving sediments toward the shelf [Bernhardt et al., 2016]. However, only 26% of all submarine canyons at the Southeast American continental margin are shelf-incising canyons [Harris and Whiteway, 2011].

The majority of all submarine canyons at the Southeast American continental margin are blind canyons [74%; Harris and Whiteway, 2011]. Due to the limitation of blind canyons to the continental slope [Harris and Whiteway, 2011], the classical view, where sediment transfer from the shallow to the deep sea is controlled by the sea level variations [Puig et al., 2014], is challenged. The formation of these slope-confined canyons have been explained by a combination of repeated slope failures and retrogressive erosion acknowledged as the upslope erosion model [Twichell and Roberts, 1982; Pratson and Coakley, 1996]. Orange and Breen [1992] relate the formation of some blind canyons to fluid seepage-induced slope failure. However, recent studies suggest the interplay of down-slope processes and along-slope currents with associated drift deposition as an important process [e.g., Mulder et al., 2006; Voigt et al., 2013]. Despite the frequent occurrences of such interactive depositional systems affected by ocean currents at continental margins [Hernández-Molina et al., 2009; Brackenkridge et al., 2013; Preu et al., 2013; Rebesco, 2014], down-slope processes are still poorly documented. Understanding the relationship between contourite depositional systems (CDS) and downslope sedimentary successions seems to be the key to estimating past fluxes of sediments in blind canyon systems. Thus, more efforts are needed to assess these ancient depositional systems, to evaluate timing of turbidite

successions and to use these sedimentary records as an indicator for the oceanographic variations.

The Mar del Plata Canyon at the Argentine continental margin represents a well suited example of such a blind, slope-confined canyon system incorporated into a CDS [Hernández-Molina *et al.*, 2009]. The canyon head originates on the Ewing Terrace at about 1000 m water depth without any upslope continuation, and is therefore located in the range of the Antarctic Intermediate Water (AAIW) [Preu *et al.*, 2013; Voigt *et al.*, 2013]. Voigt *et al.* [2013] have recently proposed that the modern AAIW nepheloid layer, flowing along the seaward boundary of the Ewing Terrace, interacts with the MdP Canyon and results in rapid and continuous deposition of coarse-silt sediments into the canyon. Now, three radiocarbon dated sediment cores were used to investigate turbidity current activity in the MdP Canyon area during the last 20 ka. These sediment records provide insight into: 1) the turbidite bed characteristics; 2) the temporal and spatial distribution of turbidity currents since the late Last Glacial Maximum (LGM); 3) the source of turbidity currents within a blind canyon system; and 4) the trigger mechanisms for turbidity-current initiation.

3.2 Background information

3.2.1 Oceanography and related sedimentary regimes

The Southwest Atlantic is an oceanographic key location in the global conveyor belt, where intermediate and deep-water masses formed in remote areas of the world interact [Figure 3.1a; Gordon, 1981; Piola and Gordon, 1989]. The intermediate and deep water circulation in the Southwest Atlantic is dominated by the Antarctic Intermediate Water (AAIW, ~500-1000 m), Circumpolar Deep Water (CDW, ~1000-4000 m) and the Antarctic Bottom Water (AABW, >4000 m) [Reid *et al.*, 1977; Stramma and England, 1999] flowing along the Southeast American continental margin. In addition, the southward-flowing North Atlantic Deep Water (NADW; ~2000 - 3000 m) vertically divides the CDW into the Upper and Lower CDW (Figure 3.1c; Stramma and England, 1999; Piola and Matano, 2001; Arhan *et al.*, 2003).

These contour following bottom currents significantly shape the Argentine continental margin by eroding, transporting and depositing sediments at the sea floor, leading to the generation of a complex CDS [Hernández-Molina *et al.*, 2009; Preu *et al.*, 2013]. Preu *et al.* [2013] proposed contourite terrace formation related to the interplay between margin physiography and the local bottom water regime. According to Preu *et al.* [2013] water mass interfaces and their associated turbulent energy patterns (i.e., high-velocity zone) induce erosion as an initial mechanism for terrace formation along the regular shaped margins. When the seaward boundary of the

terrace is outside this high velocity zone, contouritic sediments are accumulated out of the nepheloid layer (Figure 3.2). Such contouritic sediments are considered to be fairly continuous [Rebesco, 2014] and present a basis for paleoceanographic reconstructions. Consequently, erosional (terraces) and depositional (contourite deposits) features correspond to the depths of water mass interfaces [Preu *et al.*, 2013]. Preu *et al.* [2013] therefore suggest that the Ewing Terrace at around 1300 m water depth is influenced by the AAIW/UCDW transition, while the Necochea Terrace at around 3500 m water is related to the presence of the LCDW/AABW interface (Figures 3.1c and 3.2).

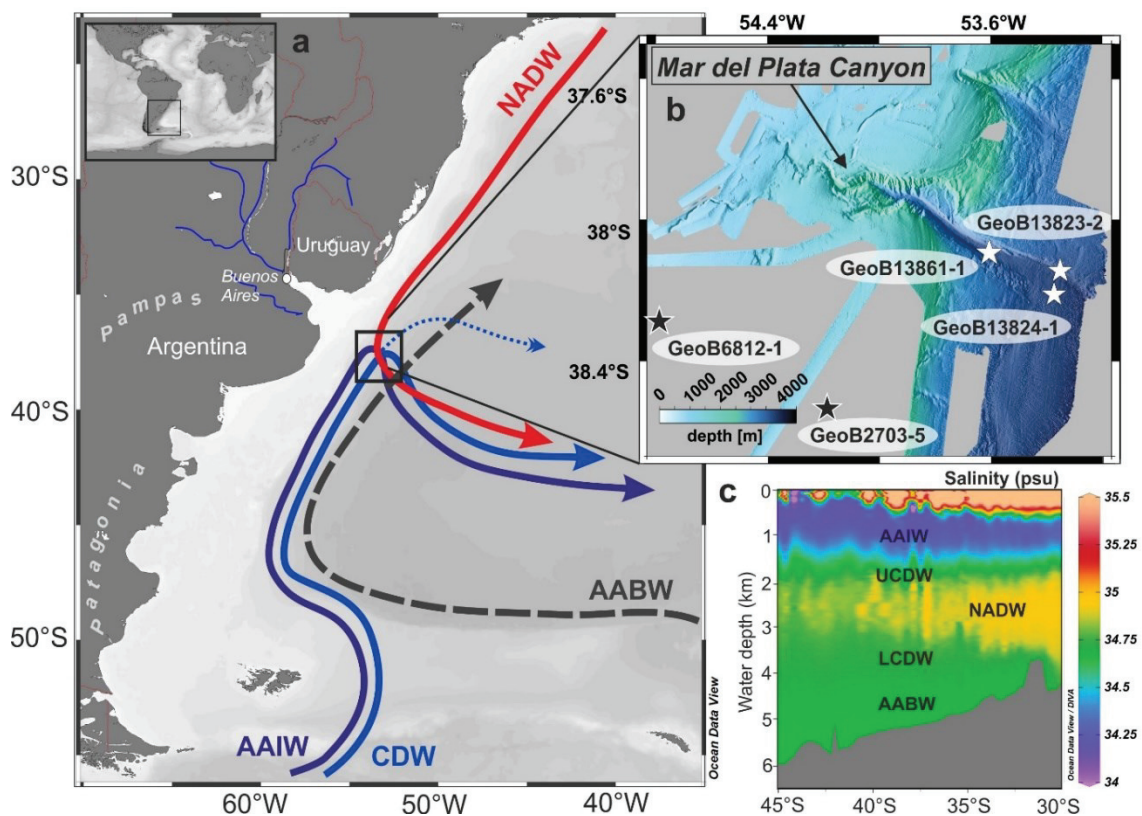


Figure 3.1: (a) Schematic intermediate and deep water circulation in the Southwest Atlantic after Stramma and England (1999). (b) Bathymetric map of the Mar del Plata Canyon including the location of the gravity cores used in this study are indicated by white (this study) and black (published cores) stars. (c) Along-slope salinity section (WOA) showing modern vertical water mass distribution between 45°S and 30°S (AABW – Antarctic Bottom Water, AAIW – Antarctic Intermediate Water, LCDW – Lower Circumpolar Water, NADW – North Atlantic Deep Water, UCDW – Upper Circumpolar Deep Water). Figure was prepared using Ocean Data View [Schlitzer, R., 2015; odv.awi.de].

The sedimentary facies on the Ewing Terrace were initially defined by Bozzano *et al.* [2011] (Figure 3.2) characterizing dark grey and homogenous sandy-silty contourite deposits. These contourite sands mainly consist of quartz and feldspar and originate from feldspar-rich sandstones or silica-rich intrusive rocks [Bozzano *et al.*, 2011], also reflected by the high magnetic susceptibility [$MS > 3000 \cdot 10^{-6} \text{ SI}$; Bozzano *et al.*, 2011]. According to Bozzano *et al.* [2011], the

Ewing Terrace sediments were mainly delivered from the shelf off northern Patagonia and/or the southern Pampa, and Buenos Aires province (Figure 3.1a), thus representing relict sands of the south Argentine continental shelf where volcanoclastic source rocks (i.e., arkosic arenites) are present [Blasi and Manassero, 1990].

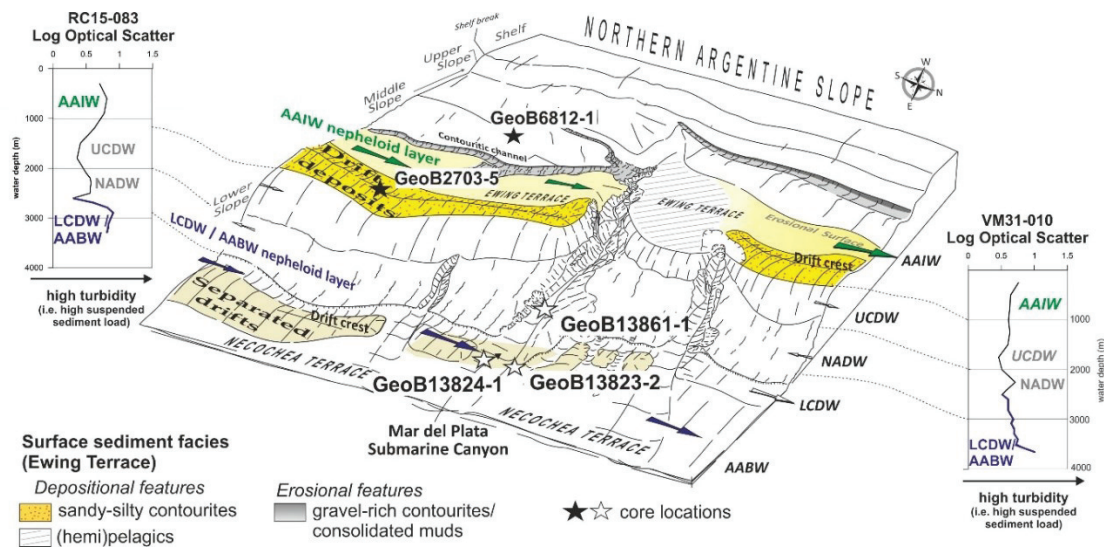


Figure 3.2: Morpho-sedimentary map of the NE Argentine continental margin indicating the erosional and depositional features along the middle, lower slope and continental rise adjacent to the Mar del Plata Canyon [modified from *Preu et al.*, 2013; *Voigt et al.*, 2016; *Voigt et al.*, 2013]. Surface sediments on the Ewing Terrace according to *Bozzano et al.* [2011]. White and black stars indicate cores used in this work and the location of published records, respectively. Measurements of high turbidity south (RC15-083) and north (VM31-010) of the studied canyon [world ocean nepheloid layer composition data base assembled by Lamont-Doherty Earth Observatory; *GeoMapApp.org*] suggest two pronounced nepheloid layer testifying strong AAIW and LCDW/AABW current activity [*Preu et al.*, 2013, *Voigt et al.*, 2013].

3.2.2 Mar del Plata Canyon

The complex CDS at the Argentine continental margin is interrupted by numerous incisions of blind submarine canyons [*Hernández-Molina et al.*, 2010] which act as downslope sediment transport path ways. One of these incisions is the blind and deeply incised Mar del Plata Canyon that is suited at a mid-slope position at 38°S (Figure 3.1). The canyon head originates on the Ewing Terrace at about 1000 m water depth without any upslope continuation. Based on seismic investigations, *Krastel et al.* [2011] excluded a connection to the shelf or the La Plata River system. The V-shaped canyon cross section contains steep canyon flanks with inclinations of 30° in places. Since the canyon extends 110 km down to the Necochea Terrace in a water depth of 3500m [*Krastel et al.*, 2011], the downslope track crosses all intermediate and deep water masses shaping the continental slope off Argentina [*Preu et al.*, 2013, Figures 3.1 and 3.2].

Voigt et al. [2013] have recently shown that an interaction of the Mar del Plata Canyon with the intermediate nepheloid layer of the AAIW along the Ewing Terrace results in rapid and continuous deposition of coarse-silt material in the canyon and presented remarkably high sedimentation rates (up to 160 cm/ka) during the Holocene (Figure 3.2). Thus, the sedimentary load responds to changes in contour current strength of the AAIW and acts as a sink for enhanced accumulation of contouritic sediments. Although turbidity currents were observed to occur during the glacial-deglacial period, during the entire Holocene no down-canyon transport deposits took place within the canyon [*Voigt et al.*, 2013].

3.3 Material and methods

3.3.1 Hydroacoustics

Bathymetric data obtained during RV Meteor Cruise M78/3 [*Krastel et al.*, 2012] were acquired utilizing the hull-mounted swath-sounder Kongsberg EM 120 (Simrad). The data were processed, visualized and analyzed by means of the open source software "MB systems" and the software package "Fledermaus" (QPS) to create a map with a spatial resolution of 75 m and a canyon axis profile following the deepest path along the thalweg with automatically generated slope angles.

Subbottom profiles were obtained with the hull-mounted parametric sediment echosounder ParaSound (Teledyne Reson). The parametric frequency was set to 4 kHz, therefore the data provide a vertical resolution of decimal scale. Data processing and interpretation of the profiles were done using the in-house software "PS32SGY" (H. Keil) and "The Kingdom software" (IHS).

3.3.2 Core locations and recovery

The study focuses on three gravity cores which were collected in the Mar del Plata Canyon area (Figure 3.2 and Table 3.1) during RV Meteor Cruise M78/3 [*Krastel et al.*, 2012]. GeoB13861-1 is located inside the canyon. Cores GeoB13823-2 and GeoB13824-1 are located on the Necochea Terrace at the northern canyon flank and in prolongation of the canyon thalweg, respectively.

Additionally, two other gravity cores GeoB2703-5 [*Segl et al.*, 1994] and GeoB6812-3 [*Spieß et al.*, 2003] located at the Ewing Terrace, were used to estimate sediment provenance of turbidity currents by comparing sediment texture and composition.

Table 3.1: Core locations and recovery of sediment cores used in this study.

Gravity core location	Cruise	Core	Latitude	Longitude	Water depth (m)	Recovery (cm)
Mar del Plata Canyon and Necochea Terrace	M78/3b	GeoB13861-1	38°09.18'S	53°60.98'W	3715	668
	M78/3a	GeoB13824-1	38°13.14'S	53°21.29'W	3821	1066
	M78/3a	GeoB13823-2	38°08.68'S	53°20.64'W	3780	938
Ewing Terrace	M29/1	GeoB2703-5	38°30.6'S	54°12.1'W	1189	467
	M49/1	GeoB6812-3	38°18.2'S	54°47.7'W	734	186

3.3.3 Grain-size determination

Detailed grain-size analyses were performed on turbidite beds to characterize the turbidite facies for cores from the Mar del Plata Canyon area. The same strategy was applied to cores from the Ewing Terrace with the objective to characterize the contouritic facies. Accordingly, grain-size analyses were performed on 34 samples, 24 selected of turbidite beds from cores located in the MdP area (18 samples from core GeoB13861-1 plus 6 samples from core GeoB13823-2) and other 10 samples of the homogenous sediment record from cores located at the Ewing Terrace (6 samples from core GeoB2703-5 plus 4 samples from core GeoB6812-1). Generally, sand, silt and clay weight percentages of the hemipelagic background sediments was calculated after wet sieving of the coarse fraction (>63 µm) and splitting the fine fraction into silt and clay using Atterberg's settling tubes.

In order to obtain the grain size distribution of the terrigenous fraction, the biogenic and organic components were removed from the bulk sediment using specific pretreatment steps described in *Mulitza et al.* [2008]. Grain-size measurements were performed with a Beckmann Coulter LS 13 320 covering grain sizes from 0.04 to 2000 µm grouped into 116 size classes. Furthermore, total carbon (TC) and total organic carbon (TOC) were measured with LECO CS-300 element analyzer. Carbonate was calculated from the difference between TC and TOC, and expressed as calcite [$\text{CaCO}_3 = (\text{TC} - \text{TOC}) * 8.33$].

3.3.4 Magnetic susceptibility

Magnetic susceptibility (MS) of sediments is primarily controlled by concentration and composition of ferromagnetic minerals [e.g., *Oldfield*, 1991], followed by their crystal size and shape [*Dearing et al.*, 1996]. Continuous 2 cm-scans for cores GeoB13823-2 and GeoB13824-1 were carried out on-board (Meteor cruise M78/3) using the GEOTEK Multi Sensor Core Logger (MSCL, whole round). The logger is equipped with a MS coil sensor (Bartington MS2C, diameter 140

mm) and effective resolution of $2 \times 10E^{-6}$ SI. One cm-scans of core Geob13861-1 were carried out using a split core logging system (Bartington MS spot sensor, University of Bremen).

3.3.5 X-ray fluorescence core scanning

High resolution X-ray fluorescence scans were performed with an AVAATECH XRF core scanner. Element intensities were measured on the split cores at 1 cm intervals and values are given in counts per second (cps). From the whole set of elements measured, Fe/K ratios were used to obtain the age models.

3.3.6 Radiographic imaging

Radiographs are an effective method of obtaining information on fabric and structural features, caused by density differences of sediment assemblages [Bouma, 1978], which may be poorly macroscopically expressed in sediment cores. Thus, 1 cm thick horizontal sediment slices of the core halves were taken for radiographs to define sediment characteristics of fine- and coarse grained sediments and to evaluate corresponding depositional processes.

3.3.7 X-ray diffraction

X-ray diffraction (XRD) of bulk sediments is a common method used to compare and reconstruct sedimentary environments and sediment transport path ways [Vogt *et al.*, 2002]. For quantitative mineralogical comparison of investigated sediments, ten selected sub-samples were measured on a Philips X'Pert Pro multipurpose diffractometer (University of Bremen) equipped with a Cu-tube (α 1.541, 45 kV, 40 mA) as homogenized bulk random powder sub-samples from $3 - 82^\circ$ 2theta (step size 0.016° 2theta). The Quantitative Phase-Analysis with X-ray Powder Diffraction software (QUAX) has been used to determine and quantify mineral assemblages [Vogt *et al.*, 2002]. A standard deviation of $\pm 5\%$ can be considered [Moore and Reynolds, 1989]. The quartz/feldspar (Qz/Fsp) and kali-feldspar/plagioclase (Kfs/Pl) ratios were calculated from the quartz 4.26 Å, K-feldspar 3.24 Å and plagioclase 3.19 Å peak intensities. The quartz/phyllsilicate (Qz/Phyllo) ratio was based on the weight % proportions.

3.3.8 Stratigraphic framework

The stratigraphy was determined using six AMS- ^{14}C ages performed on planktonic foraminifera (*Globorotalia inflata* and *Globigerina bulloides*, supporting information Table 3.SI 1) from the hemipelagic facies of the cores. Conventional radiocarbon ages were determined in the Poznan Radiocarbon Laboratory (Poland) and ETH Zürich, Switzerland [Bard *et al.*, 2015]. Radiocarbon ages were converted to calibrated ages (cal ka BP) using CALIB 7.0.0 radiocarbon calibration program applying the Marine13 calibration curve [Reimer *et al.*, 2013]. Correlation between

cores GeoB13861-1, GeoB13823-2, and GeoB13824-1 and the AMS ^{14}C -dated core GeoB13862-1 [Voigt *et al.*, 2013] was established using Fe/K downcore records. The age models were already published in Warratz *et al.* [2017].

In order to build a solid age model, turbidite beds were removed from the hemipelagic sediment record. Turbidites, whose boundaries were identified from visual inspection and sedimentological analyses (i.e., color, radiographs and grain-size data) were cut out. Each turbidite was numbered according to its position within the sedimentary sequences with T1 at the top (most recent) and Tx at the base (see supporting information Table 3.SI 2). Correlation and assignment of ages to the background intervals of all cores were made by linear interpolation between tie points. Approximate ages of turbidite successions were derived from underlying background sediment age record after the method of Henrich *et al.* [2010]. Hence, the calculated age of the background sediment at the base of each turbidite bed was assessed to be the age of the turbidity current.

3.4 Results

3.4.1 Morphological analyses of the canyon thalweg

The seafloor morphology of the study area (Figure 3.3a) reveals that the MdP canyon has its head region at about 1000 m water depths with a narrow thalweg with incision of 100-120 m. In its middle sector (between 1200-1500 m) the canyon loses its morphological expression with very smooth flanks and a valley width that ranges from 15 to 25 km. Below 1500 m, the thalweg is again deeply incised with flanks that reach more than 400 m. Slope gradients along the canyon axis (Figure 3.3b), the occurrence of knickpoints and sinuosity of the thalweg allowed a definition of four distinct areas for further classification:

Area A1 (sinuous pattern) of the canyon thalweg ranges from 1200 to 1475 m water depth over smooth distance of ~ 16 km. The average slope gradient is 1.1° with a maximum slope gradient of $< 6^\circ$ (Figure 3.3b).

Area A2 (sinuous pattern) ranges from 1475 to 3020 m water depth over 31 km. The area shows most recent v-shaped and staircase-like pattern with terraces and five knickpoints along this section of the thalweg (a – 13° , b – 17° , c – 21° , d – 15° and e – 11° , Figure 3.3b). The average slope gradient of this area is 2.8° .

Area A3 (sinuous to almost straight pattern) ranges from 3020 to 3715 m water depth over 31 km. The average slope gradient of 1.5° with a maximum slope gradient of $< 8^\circ$ (Figure 3.3b).

Area A4 denotes a straight pattern. The lower part of the straight canyon thalweg ranges from 3715 to 3950 m water depth over a distance of ~ 32 km. The smooth thalweg has the lowest average slope angle of 0.35° with maximum inclinations of < 4° (Figure 3.3b). In addition, the southern distal canyon flanks change to a smooth and hummocky morphology. The three investigated cores (GeoB13861-1, GeoB13823-2, and GeoB13824-1) are located within area A4.

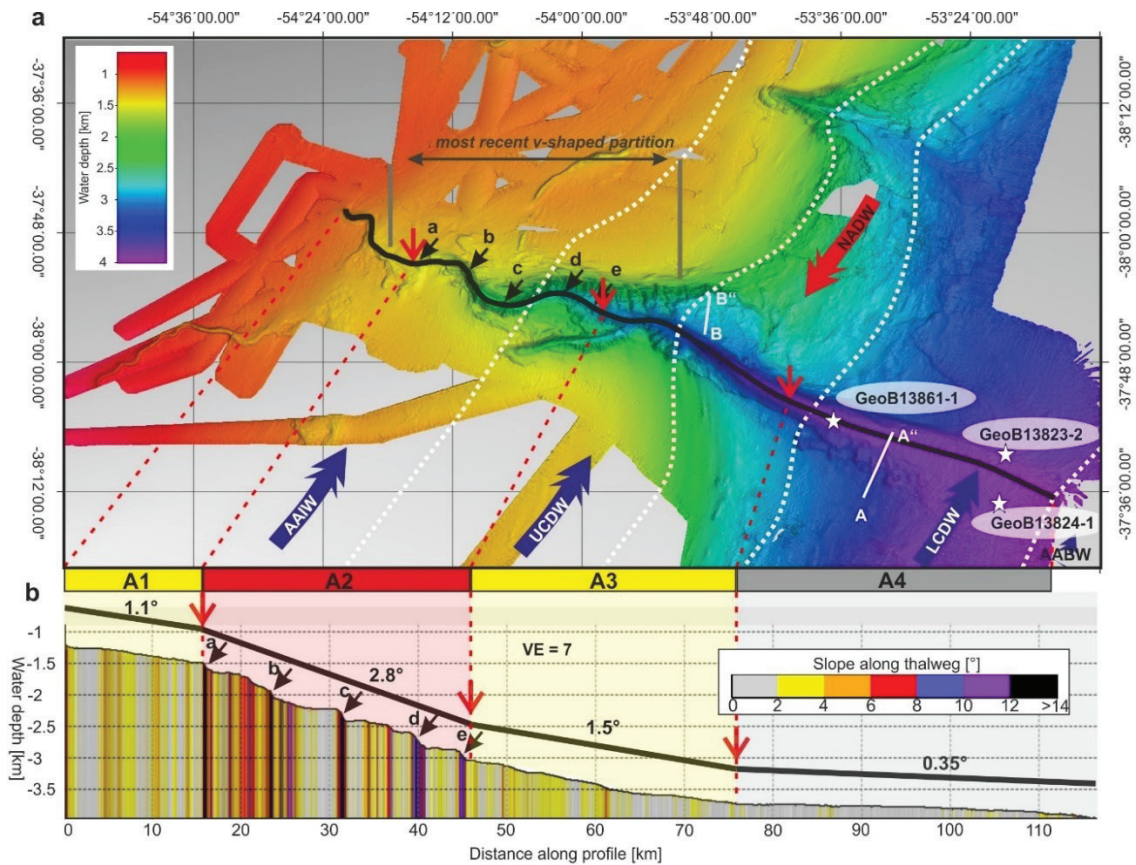


Figure 3.3: (a) Mar del Plata Canyon thalweg profile and corresponding morphological features. Grouping of four areas (A1, A2, A3 and A4) is depicted by red small arrows and red dashed lines. Knickpoints (black arrows: a=13°, b=17°, c=21°, d=15°, e=11°) are located within partition A2. Additional locations of cores (white stars) and ParaSound profiles A-A'' and B-B'' are depicted. Modern water mass stratification (Piola and Matano, 2001) is indicated by white dashed lines (key for abbreviations in Figure 1). (b) Axial canyon profile with corresponding average slope gradients of specific partitions and knickpoint positions (VE – vertical exaggeration).

3.4.2 Sedimentological and depositional characteristics

The three sediment cores collected within the MdP Canyon area denote two types of sediment (Figure 3.4). Sediment facies 1 consists in olive-brown silt with variable amounts of fine sand that range from 10% to 40%. Bioturbation is intense to moderate and microfossils are rare to absent. Sediment facies 2 consists of dark gray fine sands with undisturbed internal structures, i.e. micro cross-bedding. The sediment grain size shows fining upward trends (Figure 3.5). Sediment facies 2 is attributed to the “turbidite facies”.

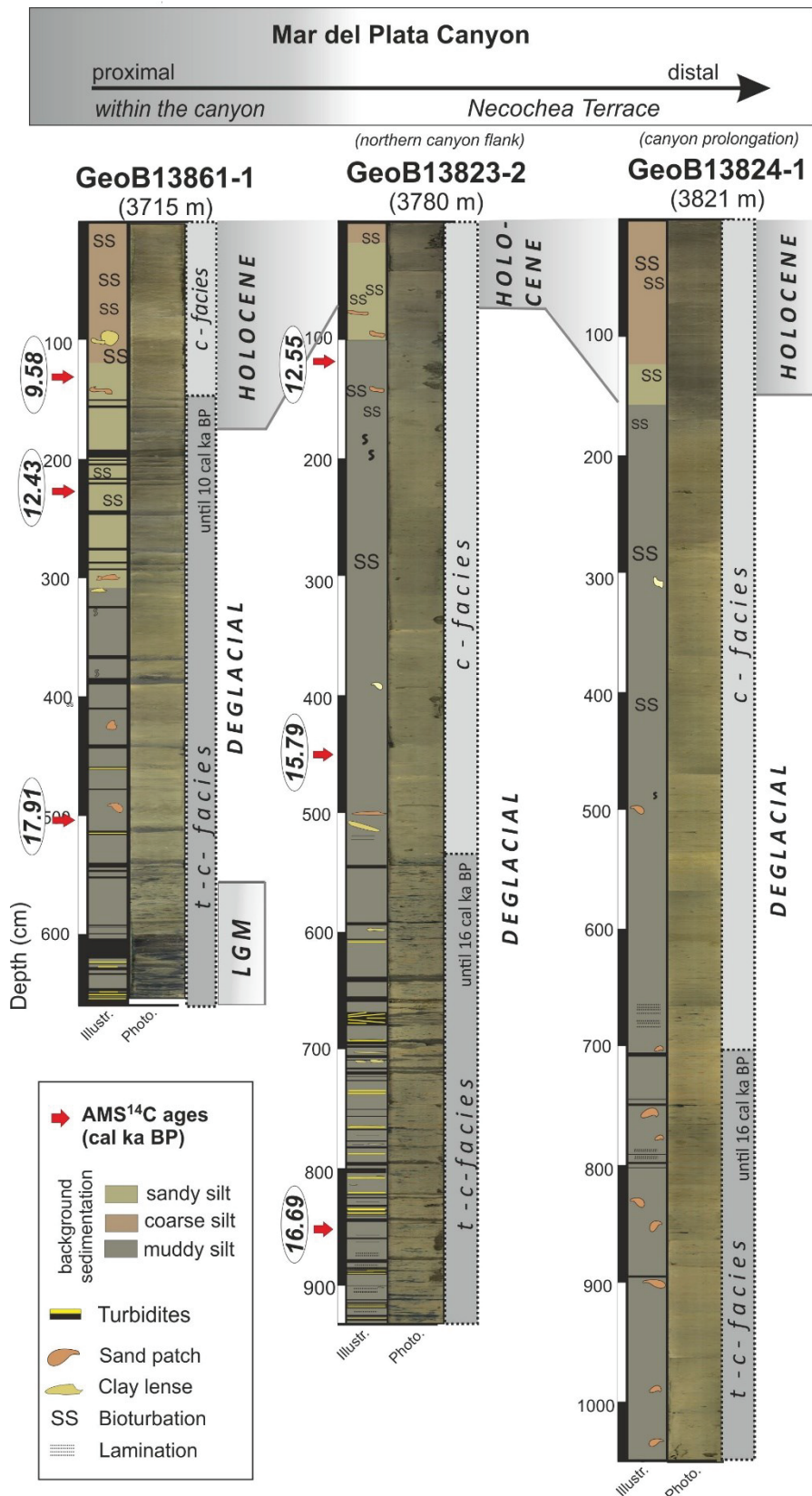


Figure 3.4: Simplified core descriptions of GeoB13861-1, GeoB13924-1 and GeoB13823-2 indicating different sedimentary facies of the background sedimentation and turbidite successions. Core photographs and facies classification are given (c-facies: contourite facies, c-t-facies: mixed contourite-turbidite facies).

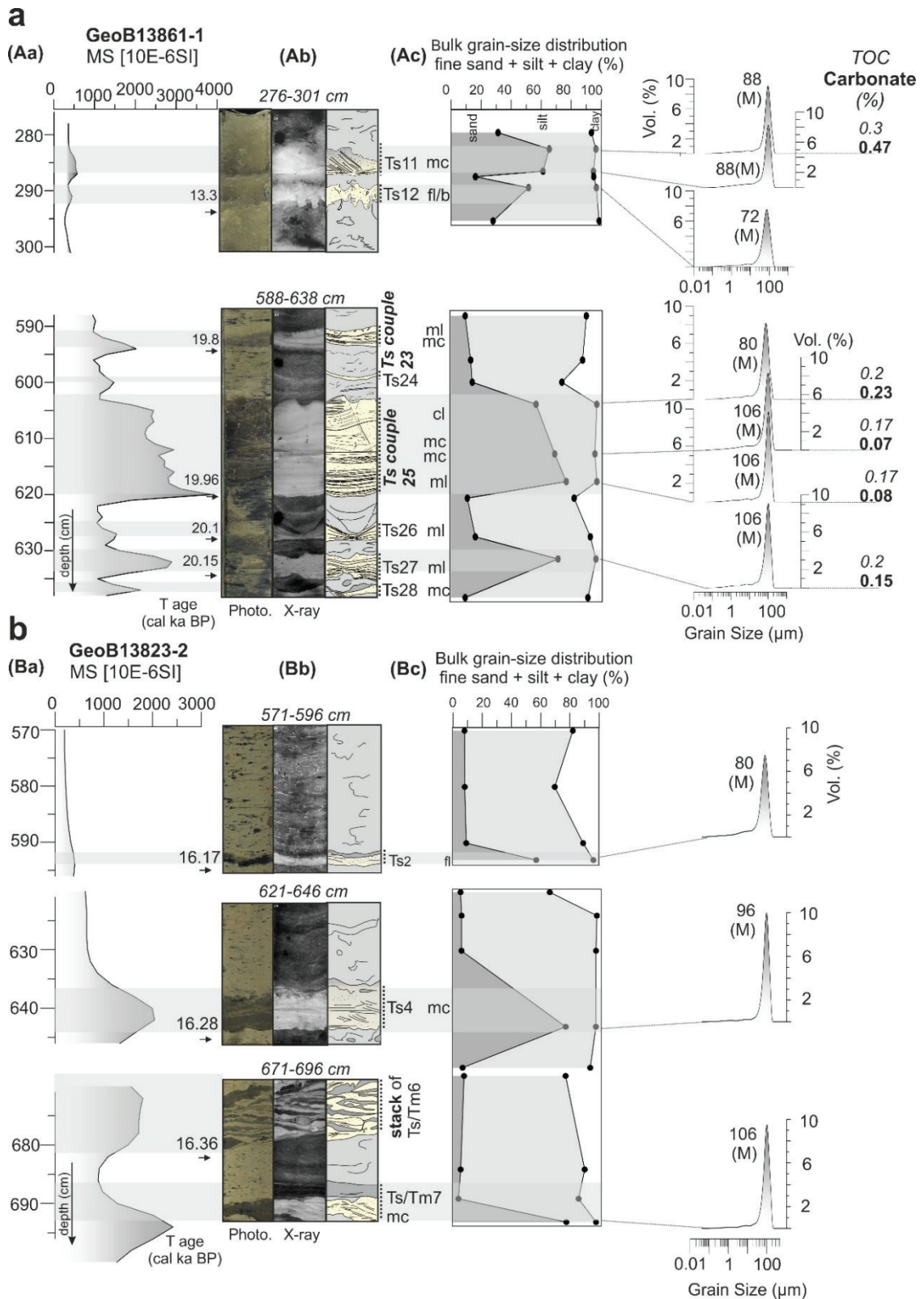


Figure 3.5: Sections of GeoB13861-1 (**a**) and GeoB13823-2 (**b**) to characterize turbidites (Ts, Tm), which are clearly distinguishable from the contourite facies. (Aa + Ba): Magnetic susceptibility (MS). Black arrows indicate ages of the turbidite beds based on background sediment age interpolation. (Ab + Bb): Core photographs, radiographs and graphic turbidite illustrations (b-bioturbated, cl-convolute lamination, fl: faintly laminated, mc: micro cross bedding, mm: sized lamination). (Ac+Bc): sand, silt and clay fractions of the contourite and turbidite facies in weight % and turbidite grain-size curve (M-mode), total organic carbon (TOC) and carbonate content of turbidites.

3.4.2.1 Sediment Facies 1

All three sediment cores show consistent hemipelagic/contouritic background lithology and can be divided into three sections based on grain-size texture (Figure 3.4). From 20 to 14 cal ka BP olive-brown muddy silt with less than 10 % very fine sand are observed. From 14 to 8 cal ka BP sediments can be defined as coarse to sandy silt with up to 40% very fine sand (Figure 3.4). Glacial sediments are stiff and compact. Microfossils are very rare to absent in glacial/deglacial sediments. From 8 cal ka BP until present, coarse silt is present with up to 20% very fine sand. Radiographs of these Holocene sections show higher bioturbation than glacial/deglacial sections.

3.4.2.2 Sediment Facies 2 - Identification of turbidite deposits

The turbidite facies within all gravity cores GeoB13861-1, GeoB13824-1 and GeoB13823-2 was identified based on structural features, colour, grain-size distribution and sediment texture (Figure 3.5).

The investigated sediments and corresponding radiographic images reveal clear contacts between the bottom of dark grey sandy turbidite deposits and the silty background sedimentation (Figure 3.5). A standard sedimentary sequence with sharp bases represented by a significant increase in percentage of fine sands (63-250 μm) and gradual tops can be structurally deciphered as follows: (1) grey to dark grey micro-cross bedded (mc) or sub-mm sized parallel-laminated (ml) very fine sands, (2) overlain by laminated very fine sands and silts, which are occasionally modified by convolute lamination (cl) and (3) sporadically homogenous mud layer (Figures 3.5Ab and 3.5Bb). The units can be characterized by *Bouma et al.* [1962] turbidite T_c , T_d and T_e units. Coarser units of the lower Bouma-Sequence [*Bouma et al.*, 1962; *Shanmugam*, 1997] are not observed. Several turbidite beds are coupled without background sediments in between (Figures 3.5Ab and 3.5Bb). Thickness of individual turbidite beds varies from a few centimeters to 10 cm (Figure 3.4 and supporting information Table 3.SI 2).

All deposits represent unimodal grain-size distribution (Figure 3.5Ac and 3.5Bc). Basal turbidite sediments of GeoB13861-1 represent modes of 96.5 μm and a negative skewness (-2.4) which slightly decrease upward to a mode of 73.3 μm with a comparable skewness (-2.35; Figures 3.5 and 3.9b). Turbidites of GeoB13823-2 report average modes of 96.5 μm and a more negative skewness (-3.1; Figure 3.9b). Coarser modes coincide with smaller skewness values (Figure 3.9c).

Turbidite successions in GeoB13861-1 are defined by high MS values, which generally exceed $1000 \cdot 10^{-6}$ SI with a maximum of $4200 \cdot 10^{-6}$ SI (Figures 3.5Aa and 3.5Ba). MS in GeoB13823-2 and

GeoB13824-1 are $> 1000 \times 10^{-6}$ SI and do not exceed 2500×10^{-6} SI. Fine grained background sediments, in contrast, represent MS values generally $< 500 \times 10^{-6}$ SI in all three cores (Figures 3.5Aa and 3.5Ba).

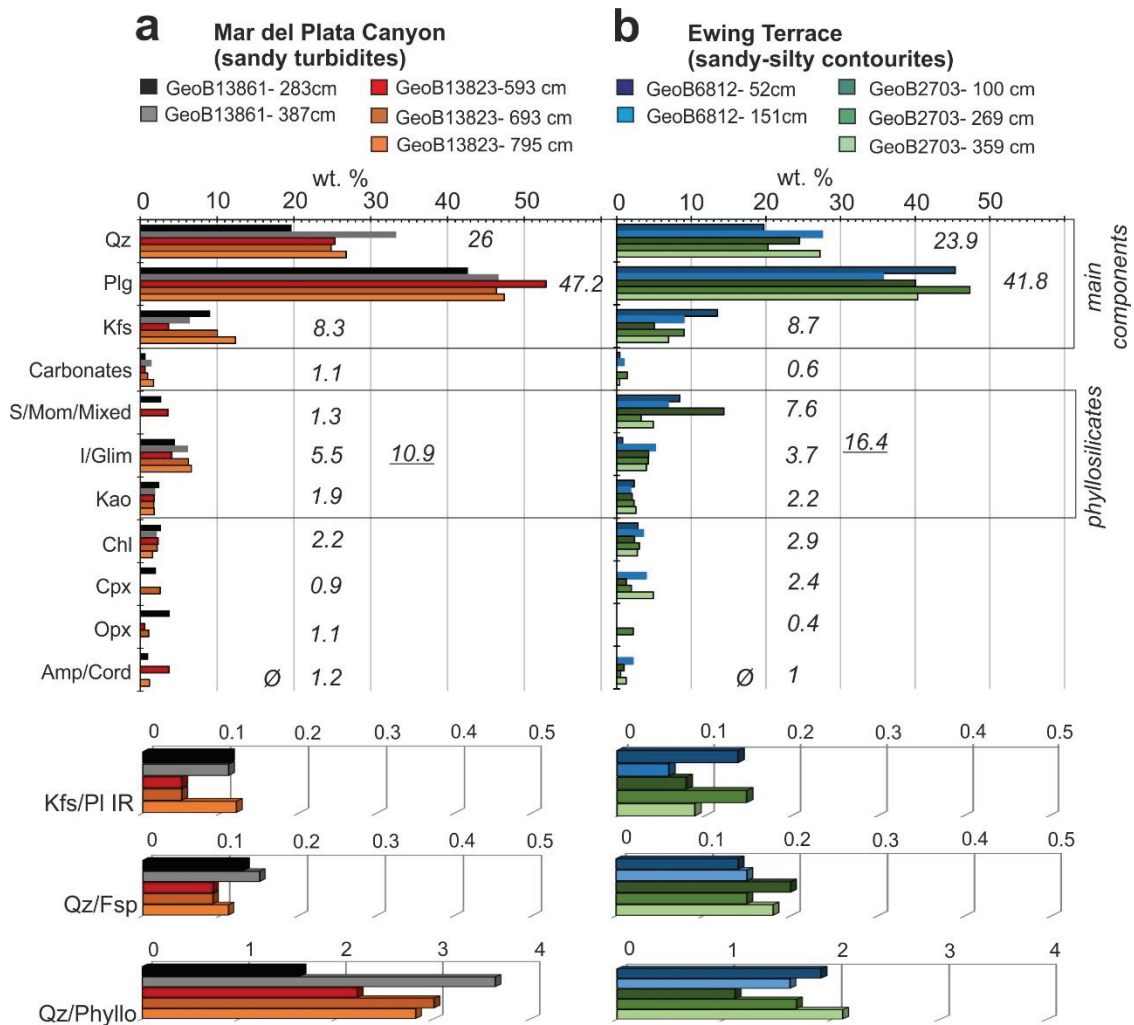


Figure 3.6: Mineralogical quantification, integrated K-feldspar/plagioclase intensity ratio, integrated quartz/feldspar intensity ratio and quartz/phyllisilicate ratio based on weight percentage of (a) turbidite beds (GeoB13823-2 – red, GeoB13861-1 – black) and (b) sandy-silty contouritic sediments from the Ewing Terrace (GeoB2703-5 – green, GeoB6812-1 – blue). Qz: quartz; Plg: plagioclase; Kfs: K-feldspar; S/Mom/Mixed: smectite, montmorillonite, mixed layer clay minerals; I/Glim: illite, muscovite, biotite, glauconite; Kao: kaolinite; Chl: chlorite; Cpx: clinopyroxene; Opx: orthopyroxene, Amp/Cord: amphibole, corundum.

Taken together, X-radiographs, grain-size data and MS values of the analyzed sediment cores show turbidite deposits with continuously fining upward sequences and missing coarse basal units, which is typical of the so-called base cut-out turbidites [Bouma et al., 1962].

All turbidite beds present low carbonate (< 0.5 %) and low total organic carbon contents (< 0.3 %, Figure 3.5), and thus consist almost exclusively of terrigenous material. XRD quantification of sandy layers (Figure 3.6a) reveals main compositional proportions of 47 weight % (wt. %) plagi-

clase, 26 wt. % quartz and 8 wt. % kali-feldspars (Figure 3.6a). Further components are phyllosilicates (< 11 wt. %), i.e. illite/mica (5.5 wt. %), chlorite (2.2 wt. %), kaolinite (1.9 wt. %) and smectite/montmorillonite (1.3 wt. %). Amphibole, calcite, corderite, clino- and orthopyroxene make up the minor fraction (< 2 wt. %). Further trace minerals (classified with < 1 wt. %) are olivine, corundum, Fe-oxides and serpentine. Based on this mineralogical quantification, quartz/phyllosilicate ratio is 3, integrated K-feldspar/plagioclase intensity ratio is 0.1, and integrated quartz/feldspar intensity ratio is 0.1 (Figure 3.6a).

3.4.3 Spatial and temporal turbidite distribution

Based on stratigraphic correlation, the proximal gravity core GeoB13861-1 within the canyon shows turbidites deposited from the LGM until the late deglacial at around 10 cal ka BP (Figure 3.4). The total thickness of turbidite beds per thousand years (cm/ka) ranges from 32 to 1 cm/ka between 20 to 10 cal ka BP and decreases during the late deglacial period. The approximate recurrence rates range from 8 to 1 turbidites per thousand years (T/ka; Figure 3.7).

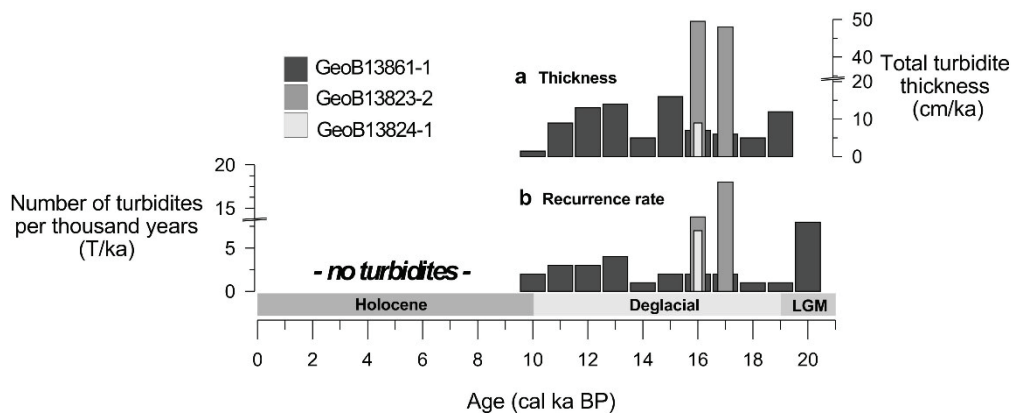


Figure 3.7: Time line of (a) total thickness per thousand years (cm/ka) and (b) turbidite recurrence rate in number per thousand years (T/ka). The Holocene sections of all cores reveal no turbidite deposits. Note: GeoB13861-1 covers the last 20 cal ka BP whereas GeoB13823-2 and GeoB13824-1 cover the last 17 cal ka BP.

Both distal sediment cores GeoB13823-2 and GeoB13824-1 show turbidite successions from 17 until about 16 cal ka BP (Figure 3.4). No turbidites were identified during the late deglacial and the Holocene. Core GeoB13824-1, within the distal channel of the canyon, presents less turbidite beds with a maximum millennial recurrence rate of 7 T/ka at 16 cal ka BP (Figure 3.7). GeoB13823-2, in contrast, denotes a recurrence rate of 16 T/ka from 17 to 16 cal ka BP in average with a total turbidite thickness of about 50 cm/ka (Figure 3.7).

3.4.4 Sedimentary characteristics of sandy-silty contourites on the Ewing Terrace

Further samples of two additional cores (GeoB2703-5 and GeoB6812-1) were analyzed to investigate sedimentological fingerprints of the sandy-silty contourites from the Ewing Terrace. Both sediment cores are composed by homogenous, grey to dark grey sandy-silty sediments throughout. All sediment samples of GeoB2703-5 and GeoB6812-1 show a unimodal grain-size distribution with a mode of 96.5 μm (skewness -2.0) and 106 μm (skewness -1.3; Figure 9), respectively.

XRD mineralogical quantifications represent quartz (24 wt. %), plagioclase (42 wt. %), kalifeldspar (9 wt. %) and phyllosilicates (17 wt. %) as main components and is followed by minor amounts of clinopyroxene (2.4 wt. %; Figure 3.6b). Trace minerals are orthopyroxene, amphibole, garnet, epidote, zeolite and pyrite. The integrated quartz/feldspar intensity ratio is about 0.16 and quartz/phyllosilicate ratio ranges from 1.1 to 2.1 (Figure 3.6b).

3.5 Discussion

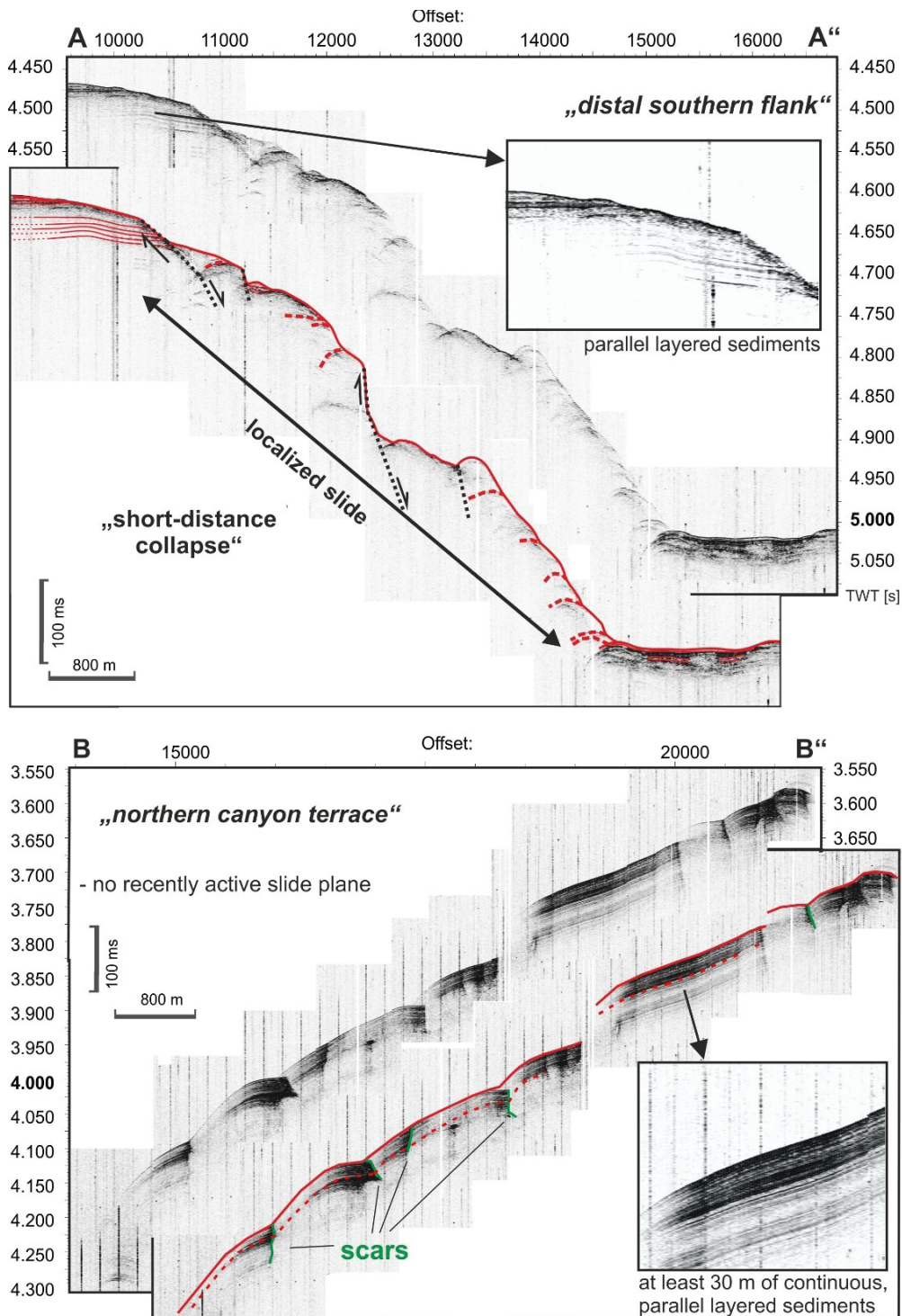
3.5.1 Locations of sediment failure

The entrenched MdP Canyon thalweg reveals variable axial gradients along its path, changing from steeper areas (Figure 3.3, A1 + A2) with specific knickpoints (Figure 3.3, A2) to a gentler slope in the lower, distal part (Figure 3.3, A3 + A4). Potential locations of slope failure were evaluated, starting at the distal canyon sector close to the thalweg coring locations.

Amphitheater-like depressions were observed at the distal southern flank in the canyon exit area. The acoustic profile in area A4 (Figure 3.3) displays a hummocky surface and several scars (Figure 3.8, A-A"). The dimension and position of these slides and their glide planes imply very local rotational slumps. These local restricted features and thalweg slope angles below 0.4°, indicate a low potential of turbidity current generation. Hence, the distal southern flank of the canyon can be excluded as a major source area for turbidites that are present in the cores at the canyon exit area (Figure 3.3, A4).

The inner terrace at the northern canyon flank within A3 (Figure 3.8, B-B") displays another set of scars, but acoustic profile shows more than 30 m of continuous, parallel layered (contouritic or hemipelagic) reflectors draping the terrace. These reflectors indicate that undisturbed sediments cover the scars and that recent slides are not present. A calculation of the slide timing based on a previously published sedimentation rate of $\sim 160 \text{ cm ka}^{-1}$ for hemipelagic or contouritic sediments within the upper MdP Canyon [Voigt *et al.*, 2013] indicates that sliding on this

terrace occurred > 20 ka ago. Therefore, also the inner terraces can be excluded as a major source of turbidite beds in the cores.



* interpreted progression of reflectors depicted with dashed lines

Figure 3.8: Parasound profiles crossing two potential areas for sediment instabilities (original and interpretation). For location compare Figure 3. **Profile A-A'** crossing the southern flank of the canyon exit displays a hummocky surface due to sliding processes. Slide planes are indicated by black dashed lines and arrows. **Profile B-B'** along the northern canyon terrace shows continuous sediment deposition for at least the last 20 ka

The turbidity currents should, therefore, stem from areas A2 and A1 (Figure 3.3), where sharp-edged, v-shaped incisions and amphitheater-like scars occur. Such patterns represent areas of canyon flank failures and retrogressive canyon erosion as suggested by *Krastel et al.* [2011]. Both processes are favored by oversteepening of contouritic sediments from the Ewing Terrace, which generally promote slope instabilities due to their heterogeneous pore pressure distribution [*Laberg and Camerlenghi*, 2008]. Thus, gravity-driven sediments should originate from the Ewing Terrace in vicinity of the canyon head (Figure 3.3, A2) or directly from the uppermost canyon thalweg by retrogressive (head ward) failures (Figure 3.3, A1).

The transformation of slope failures into turbidity currents are typically initiated by liquidation during hydraulic jumps, which may be triggered at knickpoints [inclinations $> 10^\circ$; *Piper et al.*, 1999] along an otherwise smooth thalweg. Such steep knickpoints occur in the uppermost part of the canyon (Figure 3.3; A1 + A2). The existence of knickpoints only in areas A1 and A2 supports the interpretation that most of these low-density turbidity currents had their origin close to the head of the canyon and were deposited in the distal MdP Canyon by deceleration due to the smooth profile of the thalweg ($< 0.4^\circ$; Figure 3.3, A4).

3.5.2 Contourite Facies

Sediment facies 1 was suggested to have its origin in the fine material transported by bottom currents along the Ewing Terrace that is trapped by the MdP canyon [*Voigt et al.*, 2013]. The depositional process within the canyon is similar to hemipelagic settling of particles through the water column. The terrigenous composition is dominant because the source area (Ewing Terrace) is covered by volcanic-pyroclastic elements typical of the Pampa-Patagonian association [*Bozzano et al.*, 2011]. Thus, this sediment type shares characteristic both of hemipelagic and contouritic facies. In this work it is referred as “contourite facies”.

3.5.3 Turbidite provenance and generation

Turbidites from the canyon and contourites from the Ewing Terrace consist of sediments with unimodal grain-size distribution and reveal comparable mode values (very fine sand) and colour (dark grey). Both contain quartz, feldspars and volcanoclastic rock fragments as dominant components (Figure 3.6). Within the Qz-Pl-Kfs ternary diagram (Figure 3.9e), Qz/Fsp, and Kfs/Pl ratios show an almost identical composition (Figure 3.6). MS values in turbidites are significantly higher than those of the contourite facies within the canyon. However, MS measurements from turbidites (Figure 3.5) and contourites from the Ewing Terrace [*Bozzano et al.*, 2011] show very

similar high values. These reflect enhanced amounts of ferromagnetic (e.g. magnetite) and paramagnetic minerals (e.g. amphiboles, pyroxenes and micas). Such minerals are commonly included in volcanoclastic rocks originating from northern Patagonia as mentioned by *Bozzano et al.* [2011]. The similarities between turbiditic and contouritic sediments suggest that the latter provided the main source for turbidity currents within the MdP Canyon.

Detailed observations of the compositional parameters display only minor sedimentary differences. The Qz/Phyllo ratios show an increase from contourites to turbidites. (Figures 3.6a and 3.6b). Turbiditic sediments reveal a slightly finer grain size mode than the contouritic sediments from the Ewing Terrace (Figure 3.9a). However, this fining significantly corroborates the source to sink approach. In addition, turbiditic sediments are characterized by increased sorting (Figure 3.9d) and lower clay contents compared to contouritic sediments. Montmorillonites are the dominant clay minerals within the contouritic sediments from the Ewing Terrace. Montmorillonites have higher potential to lower sediment shear strength than kaolinite and illite [*Laberg and Camerlenghi, 2008*], thus, representing the ability to promote contouritic sediment failures. Since down-slope sediment flow is normally combined with gravity-induced grain-size fining, turbidity currents generating from contourites from the Ewing Terrace show a progressive fining and sorting over the 10 km thalweg distance of the canyon. Both effects, increased sorting and reduced clay contents during the down-slope process, may lead to the relative enrichment of quartz and feldspar in turbidite deposits (Figure 3.6) and provide a reasonable explanation for these minor differences.

Hence, the turbidites resulted from the along-slope delivery of sandy-silty contourites converted into gravity-driven sediment flows after having been trapped and accumulated within the canyon head. This scenario is consistent with the position of the MdP Canyon in a CDS [*Hernández-Molina et al., 2009; Preu et al., 2013*] and with the key role of the AAIW nepheloid layer on rapid and continuous sedimentation around and into the canyon as already suggested by previous studies [*Voigt et al., 2013; Voigt et al., 2016*].

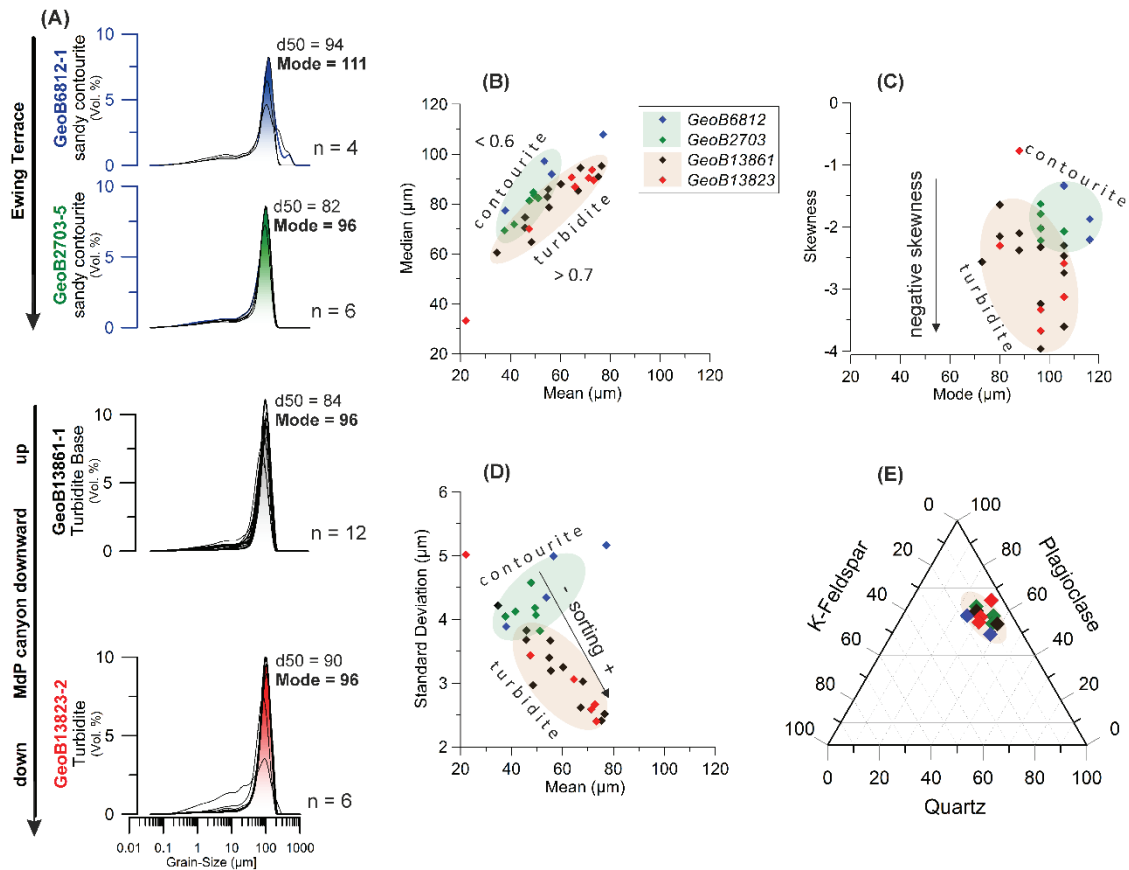


Figure 3.9: Grain-size and compositional data of sediments from the Ewing Terrace (GeoB6812-1 in blue, GeoB2703-5 in green) compared to sandy turbidite beds in the Mar del Plata Canyon (GeoB13861-1 in black, GeoB13823-2 in red). **(a)** Gaussian grain-size distribution (n – number of samples); **(b)** Grain-size median versus mean; **(c)** Grain-size mode versus skewness; **(d)** Grain-size mean versus standard deviation; **(e)** Ternary component diagram of Quartz, Kali-feldspar and Plagioclase.

3.5.4 Timing of turbidite successions

Three possible scenarios for the Mar del Plata Canyon turbidity-current activity are proposed here (Figure 3.10):

- In the LGM and the early deglacial scenario (20-14 cal Ka BP; Figure 3.10a), turbidity currents reached both the proximal and distal sector of the MdP Canyon as well as the northern canyon flank, where turbidites are more abundant than close to the thalweg. As mentioned in paragraph 3.5.1 and 3.5.2, the source of the turbidity currents was restricted close to positions in the canyon head area (Ewing Terrace). As higher sedimentation rates increase pore pressure, turbidity currents might have been triggered by increased sediment accumulation in the canyon head area.

According to *Hernández-Molina et al.* [2009] not only intermediate, but also deep water masses of the South Atlantic shape the Argentine continental slope. The deep water masses,

therefore, influence the sediment distribution on the Necochea Terrace. Based on clay mineralogical investigations as provenance signals of sediments, *Warratz et al.* [2017] have contributed to the understanding of deep water masses along the Argentine continental margin. The data set suggests that the northward flowing LCDW/ABW was continuously present along the Necochea Terrace during the last 20 ka and that the distal canyon sector was influenced by this northward flow. Hence, as soon as the turbiditic sediment cloud was no longer confined by canyon walls, the glacial AABW pushed the sediment cloud off the thalweg and toward the northern canyon flank (Figure 3.10a).

- The late deglacial scenario (14-10 cal ka BP, Figure 3.10b) shows that turbidity current activity only reached the proximal canyon position. The mode of late deglacial turbidites was slightly finer than turbidites of the early deglacial period and LGM (Figure 3.6a, Ts11 + Ts12). This general decrease in grain size indicates that these turbidity currents might have terminated before they reached the distal sector of the canyon. A decline in turbidite grain-size until the late deglacial also indicates a change in the sedimentary dynamics at the source area (Ewing Terrace) due to a modification of the oceanographic regime, i.e. AAIW position and/or intensity. Nevertheless, the existence of turbidites still indicates the potential for oversteepening, sidewall collapses or retrogressive failures triggered by ongoing but slightly finer sediment deposition in the MdP Canyon head area.
- During the Holocene (10 ka BP-present; Figure 3.10c), conditions for turbidite formation at the Ewing Terrace declined. The sedimentation within the canyon was influenced by sediment dynamics of the modern AAIW/UCDW [*Voigt et al.*, 2016; *Voigt et al.*, 2013] and LCDW/ABW nepheloid layers [*Warratz et al.*, 2017] at mid and deep water depths, respectively. Thus, Holocene contouritic sediments are homogenous and strongly bioturbated.

Due to the fact that turbidity currents are restricted to the last glacial period, sea level could be the main trigger for turbidity current activity in the MdP Canyon. However, the Mar del Plata Canyon does not have any connection to the shelf [*Krastel et al.*, 2011], even during LGM sea level lowstand [*Lantzsch et al.*, 2014]. In addition, *Chiessi* [2008] and *Lantzsch et al.* [2014] have shown that during glacial times the La Plata River sedimentary load was directly delivered to the Rio Grande Cone Basin located to the north of the MdP Canyon. Thus, the direct influence of sea level changes and the La Plata River as a potential sediment source for turbidites in the MdP Canyon can be excluded during glacial times.

Similar grain-size, MS, and mineralogical data of contourites and turbidites (Figure 3.9) support the idea that both sediments had their primary origin from northern Patagonia from where they have been transported along the Argentine continental margin to the north, i.e., along the

Ewing Terrace [Bozzano *et al.*, 2011]. As shown in Paragraph 3.5.2, parasound data indicate that the turbidity currents were initiated in the canyon head area (Figure 3.3 A1 + A2). Hence, only enhanced sediment delivery could have most probably caused mass wasting, e.g., due to oversteepening and transformed into turbidity currents at knickpoints.

The Ewing Terrace is shaped by the AAIW [Preu *et al.*, 2013]. Voigt *et al.* [2013] recently proposed that the AAIW is the only water mass responsible for contouritic sediment supply to the MdP Canyon head area. Nevertheless, reasons for glacial turbidite initiations still remain unclear. On the one hand, a strengthened glacial AAIW could have increased the nepheloid layer sediment supply to the MdP Canyon head area. On the other hand, a shallower glacial AAIW could have shifted the position of the responsible nepheloid layer close to the uppermost canyon head, where knickpoints are indicative for retrogressive erosion. Both scenarios could have most probably result in rapidly increasing sedimentation rates of sandy-silty contourites. When exceeding pore pressure during the LGM until the late deglacial, these contourites evolved into turbidity currents reaching the proximal and distal sector of the MdP canyon. Thus, glacial turbidity current activity in the slope-confined canyon was most probably controlled by vertical shifts and/or the enhanced strength of the glacial AAIW nepheloid layer.

During the Holocene, turbidity-current activity was absent. It can be expected that the modern AAIW nepheloid layer supply and the subsequent sedimentation rates along the Ewing Terrace, near to the canyon head sector, were too low to exceed pore pressure. Thus, silty contourite deposition took place within the canyon [Voigt *et al.*, 2013] but the basis for sandy turbidity currents were switched off. Although decreased sedimentation is the most obvious reason for missing turbidity currents, the direct trigger for turbidite initiations are not yet fully understood and need further research.

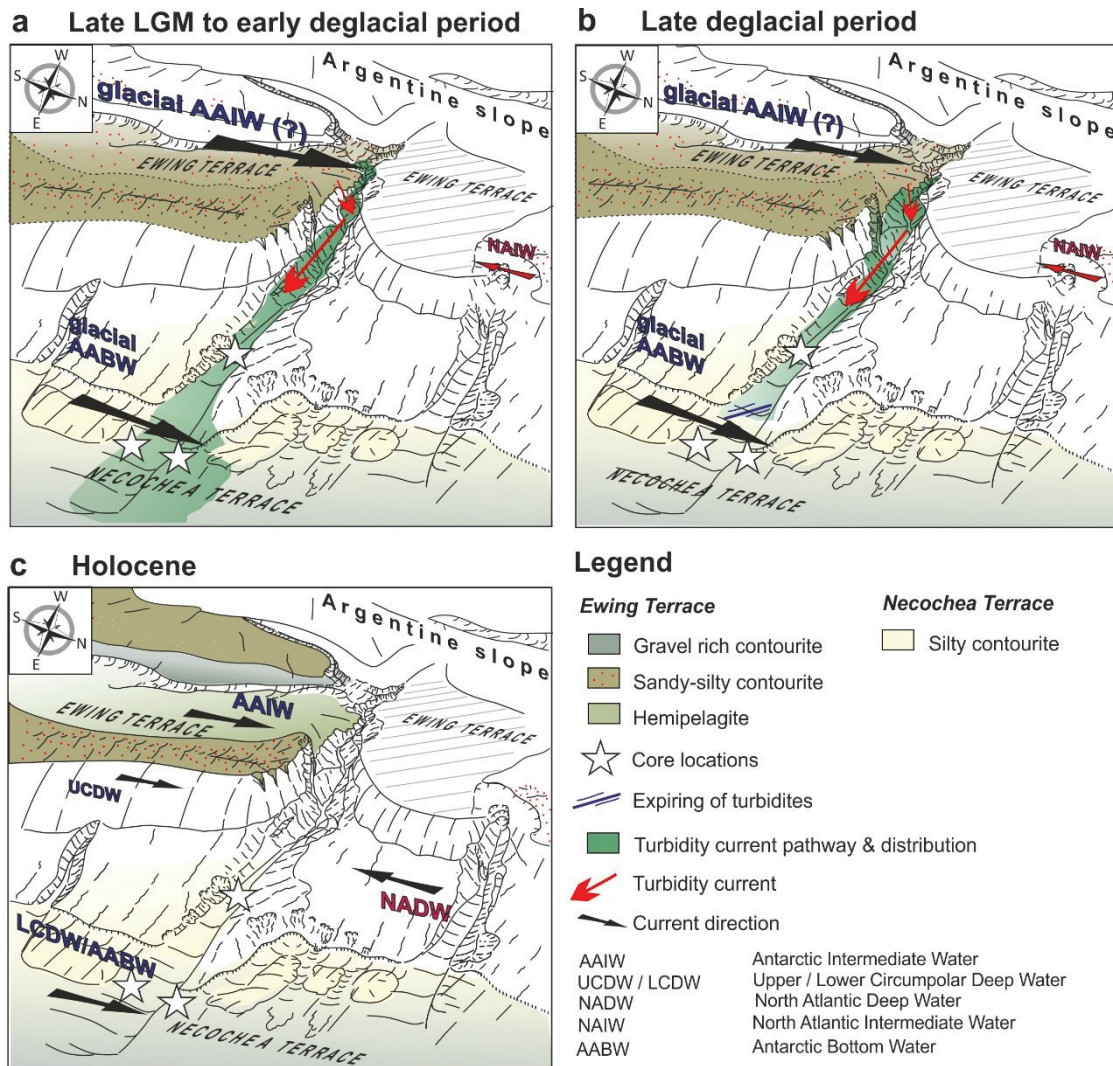


Figure 3.10: Simplified turbidite distribution and oceanographic implications for distinct time periods: LGM to the early deglacial (a), late deglacial (b) and Holocene (c). Surface sediment distribution along the Ewing Terrace inferred from Bozzano et al (2011). Glacial water mass distribution following Howe et al. (2016).

3.6 Conclusions

The Mar del Plata Canon within a CDS at the Argentine continental margin denotes the interaction of along- and down-slope sedimentary processes. However, this study represents a step forward in the understanding of slope-confined canyons. The contourites from the middle slope (Ewing Terrace) and turbidites within the MdP Canyon share a common mineralogical and sedimentological signature. For the first time, it can be confirmed that the turbidites, observed at > 3700 m water depth, rather originate from the middle slope than from the continental shelf off La Plata River.

Turbidite generation in the canyon head area, which is characterized by v-shaped incisions and amphitheater-like scars, might be related to instability processes, i.e., retrogressive erosion or

canyon flank failures, and/or to AAIW dynamics and its nepheloid layer. Thus, rapid drift accumulation along the Ewing Terrace, forced by the AAIW nepheloid layer, and the presence of the canyon head may have favored specific conditions (oversteepening and pore pressure in excess) to trigger turbidity flows during the past 20 ka. Specific knickpoints restricted to the uppermost canyon thalweg probably acted as hydraulic jumps to transform sediment slides into turbidity currents or to accelerate the turbidity flows.

Turbidity currents occurred only during the LGM until the late deglacial. No turbidites were observed during the Holocene. During the LGM and early deglacial, part of the gravity-driven sediments from the distal canyon thalweg were captured by the AABW, carried northward and finally deposited at the northern canyon flank. This conclusion demonstrates the importance of bottom waters in altering sedimentary processes in the MdP Canyon at different water depths. During the late deglacial, very fine sand turbidites thinned out and only reached the proximal canyon sector. This suggests that the mechanisms, i.e., increased sediment accumulation along the Ewing Terrace, triggering turbidite generation at the Ewing Terrace progressively slowed down during the late deglacial until they switched off completely during the Holocene.

The turbidity-current activity in the MdP Canyon is steered by the delivery of contouritic sediments. Concomitant sediment deposits provide valuable information on strength and distribution of water masses. Nevertheless, more investigations on AAIW dynamics, with special emphasis on water mass and sea-floor morphology interaction, are needed.

Acknowledgements

We acknowledge S. Krastel for comments and discussion. We thank B. Kockisch for lab assistance. We thank C. Hilgenfeldt and the Section of Marine Geophysics (University of Bremen) for the good collaboration and providing equipment for MS measurements. We acknowledge C. Vogt for XRD measurements. XRF data were acquired at the XRF Core Scanner Lab at the MARUM, University of Bremen. Sample material was provided by the GeoB Core Repository at MARUM – Center for Marine Environmental Sciences, University of Bremen. Special thanks go to Captain and crew of RV Meteor during cruise M78/3 and the hydro-acoustic watchkeepers. This study was funded through the DFG-Research Center/Cluster of Excellence “The Ocean in the Earth System” (MARUM) and was supported by GLOMAR – Bremen International Graduate School for Marine Sciences. IV further acknowledges the support from DFG grant VO2094/1-1. The new data reported in this paper will be archived in PANGAEA (Pangaea DOI provided after acceptance).

Supporting Information

Table 3.SI 1: Accelerator mass spectrometry radiocarbon dates and calibrated ages used in this study to constrain the age models.

Lab Sample Code	Depth (cm)	Species	Radiocarbon age $\pm 1\sigma$ error (ka)	1σ calibrated age range (cal ka BP)	Calibrated age from 1σ range (cal ka BP)	Reference
GeoB13861-1						
Poz-68951	139	<i>G. inflata</i> , <i>G. bulloides</i>	8.93 \pm 0.050	9.52-9.64	9.58	Warratz et al. (2017)
Poz-68952	250	<i>G. inflata</i> , <i>G. bulloides</i>	10.88 \pm 0.060	12.30-12.54	12.43	Warratz et al. (2017)
Poz-73049	505	mixed foraminifera*	15.12 \pm 0.080	17.8-18.02	17.91	Warratz et al. (2017)
GeoB13823-2						
Poz-38953	120	<i>G. inflata</i> , <i>G. bulloides</i>	10.99 \pm 0.060	12.49-12.61	12.55	Warratz et al. (2017)
Poz-68954	462	mixed foraminifera*	13.57 \pm 0.190	15.50-16.08	15.79	Warratz et al. (2017)
ETH-66209	852	<i>G. inflata</i> , <i>G. bulloides</i>	15.78 \pm .0.160	16.85-16.52	16.69	Warratz et al. (2017)

*Mixed foraminifera consist of *Globorotalia inflata*, *Globigerina bulloides*, *Bolivina inflata* and *Globolumnia affinis*.

Table 3.SI 2: Classification, base depths, thicknesses, and approximated ages of turbidite beds in sediment cores GeoB13861-1, GeoB13823-2, GeoB13824-1. (Tm – muddy Turbidite, Ts – sandy Turbidite).

GeoB13861-1				GeoB13824-1				GeoB13823-2			
Type/No.	Turbidite base (cm)	Turbidite thickness (cm)	Approx. age (cal ka BP)	Type/No.	Turbidite base (cm)	Turbidite thickness (cm)	Approx. age (cal ka BP)	Type/No.	Turbidite base (cm)	Turbidite thickness (cm)	Approx. age (cal ka BP)
Ts1	153	1	10,01	Ts1	710	2	15,93	Ts1	542	1	16,03
Ts2	164	0,5	10,34	Ts2	747	1	16,02	Ts2	595	2	16,17
Ts3	197	7	11,20	Ts3	754	2	16,03	Ts3	608	1	16,21
Ts4	201	1	11,27	Ts4	792	1	16,12	Ts4	644	8	16,28
Ts5	205	1	11,37	Ts5	801	1	16,14	Ts5	662	5	16,33
Ts6	217	3	11,67	Ts6	804	1	16,14	stack of Ts/Tm6	681	10	16,36
Ts7	220	2	11,70	Ts7	896	1	16,37	Ts7	695	4	?
Ts8	245	8	12,26					Ts8	699	4	16,38
Ts9	260	2	12,65					Ts9	702	1	16,39
Ts10	276	5	13,16					Ts10	710	3	16,40
Ts11	287	4	13,26					Ts11	717	3	?
Ts12	293	3	13,36					Ts12	720	3	16,41
Ts13	330	5	14,26					Ts13	726	1	16,43
Ts14	367	6	15,24					Tm14	741,5	3,5	16,47
Ts15	389	10	15,50					Ts15	756,5	0,5	16,50
Ts16	409	2	15,89					Tm16	764	1	16,52
Ts17	440	5	16,43					Ts17	773	1	16,55
TsTmTs18	459	4	16,77					Ts18	783	2	16,57
Ts19	479	2	17,23					Ts19	797	4	16,60
Ts20	515	5	18,04					stack of Ts/Tm20	805	6	16,60
TsTmTs21	546	10	18,62					Tm21	820	1	16,64
Ts22	552	2	18,73					Ts22	822	1	16,65
TsCouple23	594	3	19,73					Ts23	825	2	16,65
Ts24	599	0,5	19,83					Tm24	829	3	16,65
TsCouple25	620	16	19,97					Ts25	832	3	16,65
Ts26	628	3	20,10					Tm26	834,5	0,5	16,66
Ts27	634	4	20,15					Ts27	839	1	16,67
Ts28	638	1	20,23					Ts28	844	3	16,68
Tm29	641	1	20,31					Ts29	859	1	16,71
Ts30	648	4	20,39					Ts30	878	4	16,75
stack of Ts/Tm31	~ 662	13	?					stack of Tm/Ts31	893	13	16,76
								Ts32	900	1	?

Chapter 4
Deglacial shift of deep southern component water in the Southwest
Atlantic

Grit Warratz¹, Ines Voigt¹, Cristiano M. Chiessi², Rüdiger Henrich¹, Hendrik Lantzsch¹

¹University of Bremen, MARUM – Center for Marine Environmental Sciences and Faculty of Geosciences,
Klagenfurter Straße, D-28359 Bremen, Germany.

²School of Arts, Sciences and Humanities, University of São Paulo, Av. Arlindo Bettio 1000, CEP03828-000 São Paulo
SP, Brazil.

- In preparation for submission to *Earth and Planetary Science Letters* -

Abstract

The deep water mass distribution in the glacial Atlantic Ocean was significantly different from today. However, due to the highly corrosive deep southern component water (SCW) in the deep Southwest Atlantic, detailed knowledge about its deglacial paleoceanographic evolution is rather limited. Here we investigate radiocarbon dated sediment cores from a contourite deposit and a core from the adjacent Argentine slope, and integrate the results to recently published records from the same region. Together, these cores provide comprehensive insights into the deglacial shift of the deep SCW based on sortable silt paleocurrent proxies (e.g., SS_{mean}) to identify the Lower Circumpolar Deep Water / Antarctic Bottom Water (LCDW/AABW) interface, an energetic interface that produces strong currents located within the deep SCW. Additional carbonate content records were used to identify the influence of northern component water (NCW) in the deep SCW-dominated Southwest Atlantic. Increased carbonate preservation from ~ 11 cal ka BP on, reflects the influence of NCW below 3000 m water depth, related to the deepening of the deep NCW/SCW interface. A peak in the SS_{mean} records reveals a period (from 15 until 11 cal ka BP) of increased bottom current strength during the late deglacial, characterizing the LCDW/AABW interface. For the first time, we are able to identify the LCDW/AABW interface shift during the late deglacial, which reaches the shallowest (3620 m) and deepest (3780 m) core site by 15 and 14 cal ka BP, respectively, and subsequently shifts downward in the water column. The findings enhance the knowledge about the temporal evolution of deep SCW, which was related to enhanced deglacial NCW spreading and LCDW inflow into the deep Southwest Atlantic. Now, the deglacial oceanic re-organization can be detected by the deepening of the LCDW/AABW interface.

4.1 Introduction

The understanding of deep southern component water (SCW), comprising Lower Circumpolar Deep Water (LCDW) and Antarctic Bottom Water (AABW), remains a critical aspect in the climate-CO₂ relationship, as it is considered to transport and store significant amounts of carbon and heat within the Atlantic Ocean [Barker *et al.*, 2010; Skinner *et al.*, 2010]. As the abyssal Atlantic is the source of the light carbon, enhanced upwelling in the Southern Ocean and outgassing of carbon may have influenced deglacial surface climate and caused atmospheric CO₂ to rise [e.g., Adkins, 2013; R F Anderson *et al.*, 2009; Kwon *et al.*, 2012]. The last deglacial period (19–11.7 cal ka BP) is characterized by a shift from ¹³C-depleted to relatively ¹³C-enriched deep SCW [Curry and Oppo, 2005]. This shift suggests that climatic changes may have controlled deep-water reorganization, making the investigation of deglacial changes in deep Atlantic circulation a mandatory topic.

In recent times, numerous studies applied nutrient tracers, i.e., Cd/Ca and δ¹³C of benthic foraminifera [e.g., Curry and Oppo, 2005; Lund *et al.*, 2015], as well as radiocarbon ventilation ages [Freeman *et al.*, 2016; Skinner *et al.*, 2010] and radiogenic isotope proxies, i.e., neodymium (ε_{Nd}) and ²³¹Pa/²³⁰Th isotopes [e.g., Böhm *et al.*, 2015; Lippold *et al.*, 2016] to provide evidence that water mass distribution in the glacial Atlantic ocean was significantly different from today. The modern deep Atlantic geometry shows North Atlantic Deep Water (NADW) occupying most of the water column (Figure 4.1a and 4.1b), while thinning out to the South (e.g., filling the water column from 2000 to 3000 m at 39°S) [Stramma and England, 1999]. During the LGM, in contrast, a shoaled and freshened northern component water (NCW) poor in nutrients and saturated in CO₃²⁻ was present in the Atlantic around 2000 m water depth, whereas a mixture with a large fraction of deep SCW and a smaller fraction of deep NCW, nutrient-rich and CO₃²⁻-undersaturated, occupied the Atlantic below 2000 m water depth [e.g., Freeman *et al.*, 2016; Howe *et al.*, 2016; Lippold *et al.*, 2016; Lynch-Stieglitz *et al.*, 2007].

Despite the major changes in the mid-depth and deep Atlantic Ocean during the last deglaciation [Lund *et al.*, 2015; Voigt *et al.*, 2017], the presence of highly corrosive deep water masses in the Southwest Atlantic [Volbers and Henrich, 2004] hampered an in depth understanding of the evolution of deep SCW. There is surprisingly little knowledge about the deglacial deep SCW, i.e. strength and vertical distribution, in the Southwest Atlantic. Only recently the highly energetic LCDW/AABW interface within deep SCW in the deep Southwest Atlantic was addressed [Warratz *et al.*, 2017]. Quantitative analysis of the grain-size populations in the terrigenous sediment fine fraction was applied as this proxy provides near-bottom flow strength, with the advantage of having a direct physical connection to immediate changes in flow strength [McCave *et al.*, 1995].

Here we show a new sortable silt paleocurrent and two carbonate records from a deep contourite deposit in the range of modern deep SCW. These records were integrated to two other nearby sortable silt records from 3715 and 3780 m water depth [Warratz *et al.*, 2017] to produce a deep water transect from 2,800 to 4,000 m. Within the frame of this transect, our aim is (i) to further extend the current knowledge of the deglacial Southwest Atlantic re-arrangement and (ii) to record the temporal and spatial shift of the LCDW/AABW interface located within the deep SCW.

4.2 Modern oceanographic setting

The Southwest Atlantic is considered to be a region where major deep-water masses interact (Figure 4.1) [Stramma and England, 1999]. Along the Argentine Margin, North Atlantic Deep Water (NADW) and Antarctic Bottom Water (AABW) mix with Circumpolar Deep Water (CDW) over the rough topography of the Scotia Sea [Broecker *et al.*, 1998].

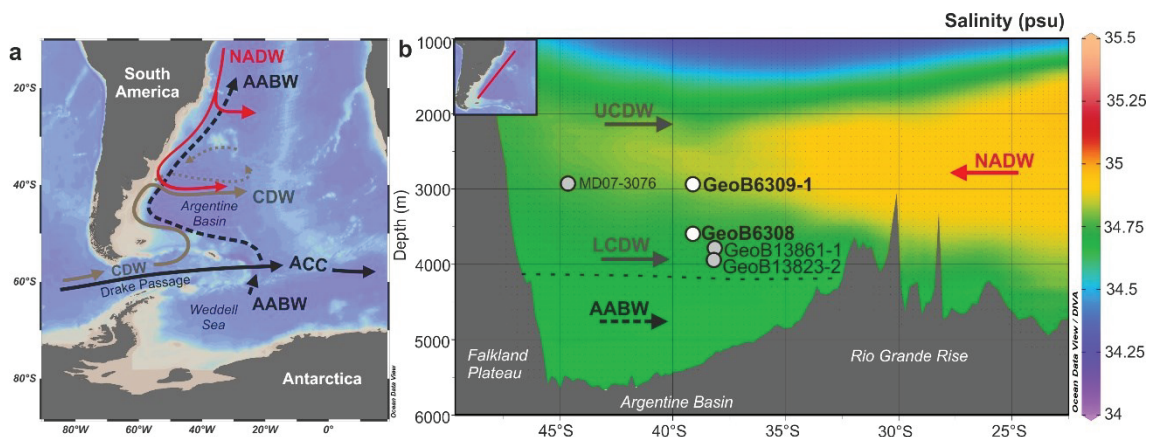


Figure 4.1: (a) Oceanographic setting at the southeastern South American continental margin. (b) Modern along-slope salinity profile [Zweng *et al.*, 2013] in the Southwest Atlantic and location of core sites discussed in this study (white dots – this study, grey dots – Warratz *et al.*, 2017; Skinner *et al.* 2013) (figure prepared with the Ocean Data View using DIVA-gridded data, <http://odv.awi.de>, [Schlitzer, 2015]). (AABW – Antarctic Bottom Water, ACC – Antarctic Circumpolar Current, CDW – Circumpolar Deep Water, LCDW – Lower Circumpolar Deep Water, NADW – North Atlantic Deep Water, UCDW – Upper Circumpolar Deep Water).

NADW is a relatively warm, saline, nutrient-poor and well-ventilated water mass formed in the high latitudes of the North Atlantic, while the cold, fresh, nutrient-rich and poor-ventilated AABW originates near Antarctica [Figure 4.1b, Reid, 1996]. AABW is generally formed by mixing of ice-shelf water (ISW) and CDW beneath the major Antarctic ice shelves (i.e., Weddell Sea, Ross Sea) [Foldvik *et al.*, 1985; Foster and Carmack, 1976] and/or coastal polynya activity around Antarctica [e.g., Marsland *et al.*, 2007; Ohshima *et al.*, 2013; Tamura *et al.*, 2008].

CDW, which is a mixture of deep water from the main oceanic basins [Orsi *et al.*, 1995], enters the South Atlantic from the South Pacific through the Drake Passage (Figure 4.1a) as part of the

Antarctic Circumpolar Current (ACC, Figure 4.1a) [Reid, 1989]. The southward flow of NADW splits CDW into an upper and a lower layer [UCDW and LCDW, respectively, Figure 4.1b, Arhan *et al.*, 2003; Piola and Matano, 2001]. UCDW is characterized by relatively low oxygen and high nutrient concentrations and is thought to originate in the Indian and Pacific Oceans [Callahan, 1972], whereas LCDW is the highly saline component of CDW, which occupies most of the deep ACC [Orsi *et al.*, 1995] and is derived from modified NADW [Dinniman *et al.*, 2011; Whitworth and Nowlin, 1987].

The ACC flow (Figure 4.1a) is mainly driven by vigorous mid-latitude westerly winds [Boning *et al.*, 2008; Orsi *et al.*, 1995; Reid, 1989] and is constricted to its narrowest extent in the Drake Passage [Lamy *et al.*, 2015]. This circumpolar current is one important pathway of fresh and cold waters to the Atlantic, which strongly affects the strength of the Atlantic meridional overturning circulation (AMOC) [Lamy *et al.*, 2015; Roberts *et al.*, 2017]. Thus, the ACC provides an effective connection between surface waters and the deep ocean [Boning *et al.*, 2008].

4.3 Material and Methods

We investigated sediment cores GeoB6308 and GeoB6309-1 from the deep Argentine continental margin at 39°S collected during RV Meteor cruise M46/3 [Bleil *et al.*, 2001, Table 4.1 and Figure 4.1b].

Table 4.1: Location and water depth of the cores investigated in this study^a and previously published^b [Warratz *et al.*, 2017] neighboring cores.

Core ID	Water Depth [m]	Latitude	Longitude
GeoB6309-1 ^a	2,867	39°10.0'S	54°08.7'W
GeoB6308-1	3,620	39°18.1'S	53°57.9'W
GeoB6308-3 ^a	3,620	39°18.1'S	53°57.9'W
GeoB13861-1 ^b	3,715	38°09.2'S	53°60.9'W
GeoB13823-2 ^b	3,780	38°08.7'S	53°20.6'W

Core GeoB6308 was recovered within a contourite drift, i.e., the Necochea Terrace, which is in modern times influenced by the northward flowing LCDW. Due to continuous sedimentation within contourite drifts, GeoB6308 is eligible for paleoceanographic reconstructions using the sortable silt paleocurrent proxy. Core GeoB6309-1 was recovered 800 m above GeoB6308, outside of the contourite drift at the deep slope, and is bathed by the lower boundary of NADW. In order to verify the representativeness of the new data presented here, we compared it to previously published data from neighboring cores GeoB13861-1 and GeoB13823-2 [Warratz *et al.*, 2017].

4.3.1 Age models

Cores GeoB6308 and GeoB6309-1 have age models based in ^{14}C accelerator mass spectrometry (AMS) analyses obtained on monospecific samples of planktonic foraminifera (pF; i.e. the deep-dwelling foraminifera *Globorotalia inflata*). Due to the lack of carbonate in the glacial section of GeoB6308-3, three new and total organic carbon (TOC) AMS ^{14}C ages were produced and used to extend the age model of GeoB6308 through the last deglaciation (Table 4.2). The age model of GeoB6308 was produced merging ten AMS ^{14}C ages of gravity core GeoB6308-3 [Lantzsch *et al.*, 2014] and two AMS ^{14}C ages of companion multicore GeoB6308-1 as published in Voigt *et al.* [2015] and accomplished by incorporating the three TOC AMS ^{14}C ages. To produce a composite core, gravity core GeoB6308-3 was synchronized with multicore GeoB6308-1 based on ^{14}C AMS results.

All AMS ^{14}C ages were calibrated using the CALIB 7.0 software [Stuiver and Reimer, 2016] applying the Marine13 calibration curve [Reimer *et al.*, 2013]. The age model was acquired by linear interpolation between calibrated ages (cal ka BP). However, pF and TOC based ^{14}C ages may show systematic differences caused by: (i) bioturbation which would cause younger pF ages; and (ii) lateral advection of resuspended organic matter (OM), since re-deposition of advected fine particles would cause OM ages to be older than pF ages. Mollenhauer *et al.* [2006] investigated pF and TOC AMS ^{14}C ages of surface samples from the Argentine Basin. Based on these results, we corrected the three ^{14}C TOC ages of GeoB6308-3 with an average reservoir age of $\Delta R=1035$ years [Mollenhauer *et al.*, 2006] and an error of ± 200 years to account for unknown changes in reservoir age through time (to compare: TOC AMS ^{14}C ages with and without corrected reservoir age of 1035 ± 200 years are shown in the supporting information; Figure 4.SI 1).

Stratigraphic correlation between core GeoB6308 and the nearby core GeoB6309-1 was based on two additional pF AMS ^{14}C ages performed on the latter and X-ray fluorescence (XRF) Fe/K downcore records using AnalySeries 1.1 core-to-core tuning (Figure 4.2a and b).

We are comparing the GeoB6308 record to other nearby cores GeoB13861-1 and GeoB13823-2 (Table 4.1) based on AMS ^{14}C ages obtained on the same deep-dwelling foraminifera [age model published in Warratz *et al.*, 2017], thus, we can exclude additional uncertainties due to local offsets of TOC AMS ^{14}C ages. Taking these reservoir ages of TOC AMS ^{14}C ages [Mollenhauer *et al.*, 2006] into account, uncertainties affecting the long term trends seem to be negligible.

Table 4.2: AMS ^{14}C ages used to compile the age model of cores GeoB6308 and GeoB6309-1 (pF – planktonic foraminifera, i.e., *Globorotalia inflata*, TOC – total organic carbon, *corrected with $\Delta R = 1035 \pm 200$ years).

	Composite core depth (cm)	Core depth (cm)	Material	Radiocarbon age (a BP) \pm error	1 σ calibrated age range (cal a BP)	Calibrated age (cal ka BP)
GeoB6309						
Poz-92686 ^a		4	pF	2140 \pm 30	1687-1784	1.74
Poz-92687 ^a		50	pF	7960 \pm 40	8367-8457	8.41
GeoB6308-1						
Poz-42364 ^b	2	2	pF	750 \pm 70	270-499	0.38
Poz-42363 ^b	11	11	pF	1310 \pm 30	769-924	0.85
GeoB6308-3						
Poz-43433 ^c	13	4	pF	1500 \pm 30	993-1097	1.04
Poz-43435 ^c	25	16	pF	2770 \pm 30	2428-2579	2.50
Poz-43436 ^c	37	28	pF	3645 \pm 30	3495-3593	3.54
Poz-43437 ^c	49.5	40.5	pF	4490 \pm 35	4636-4775	4.71
Poz-43438 ^c	61	52	pF	5240 \pm 25	5574-5624	5.59
Poz-43439 ^c	73	64	pF	6290 \pm 40	7175-7224	7.19
Poz-43440 ^c	85	76	pF	7310 \pm 40	7717-7823	7.77
Poz-43441 ^c	97	88	pF	8970 \pm 40	9544-9667	9.61
Poz-43442 ^c	109	100	pF	9930 \pm 50	10791-10994	10.89
Poz-43443 ^c	116	107	pF	10130 \pm 50	11087-11195	11.14
Beta-341847 ^d	190	181	TOC	13490 \pm 50	*13641-14215	*13.93
Beta-341848 ^d	275	266	TOC	14280 \pm 60	*15011-15722	*15.37
Beta-341849 ^d	360	351	TOC	17060 \pm 70	*18654-19118	*18.89

^a ^{14}C (pF) ages being first published in this study, ^b Voigt et al. [2015], ^cLantzsch et al. [2014], ^d TOC ^{14}C ages first being published in this study.

4.3.2 Sortable silt grain-size measurements

Grain-size distributions of the terrigenous fraction were analyzed with a Beckman Coulter Counter (LS 13320 Laser Diffraction Particle Size Analyzer), resulting in 116 size classes from 0.04 to 2000 μm . Although measurements of laser diffraction particle sizing might be biased due to potential particle shape effects [McCave et al., 2006], this technique has been shown to yield high-precision data that accurately reflect even small changes in the mixing proportion of sediments [e.g., Goossens, 2008; Jonkers et al., 2009]. Prior to grain-size measurements, the terrigenous fraction (i.e., organic carbon-, carbonate-, and opal-free) was isolated using several pretreatment steps as described in Mulitza et al. [2008].

In order to reliably support SS_{mean} trends, grain-size analyses were repeated with the Sedigraph D5100. Prior to measurements with a sample interval of 10 cm, clay contents were minimized to < 5 % adding dispersive agent $\text{Na}_4\text{P}_2\text{O}_7 \cdot 10 \text{H}_2\text{O}$ and using Atterberg settling tubes (10-20 times) according to Stoke's Law.

We applied the sortable silt paleocurrent proxy, i.e., sortable silt mean size (SS_{mean} in μm), to reconstruct relative changes in bottom current strength of the deep SCW. Hence, *McCave et al.* [1995] have proposed that the SS_{mean} refers to the terrigenous 10–63 μm size fraction, whose size sorting varies in response to hydrodynamic processes. Low (high) SS_{mean} values indicates weak (strong) current flow strength [*McCave*, 2008]. The SS_{mean} has been used successfully applied in different paleocurrent studies in the North Atlantic [e.g., *Channell et al.*, 2016], the South Atlantic [e.g., *Voigt et al.*, 2016; *Warratz et al.*, 2017] and the Southern Ocean [*McCave et al.*, 2014]. In addition, a new approach of SS_{mean} relative bottom-current flow strength calibration was introduced by *McCave et al.* [2017]. The authors suggest that is difficult to define a universal conversion of SS_{mean} to absolute flow speed. However, there is a local calibration, such as for the Scotia Sea, which makes it possible to estimate absolute changes in flow speed with some confidence. The corresponding sensitivity of SS_{mean} to bottom current flow speed is $1.36 \pm 0.19 \text{ cm s}^{-1}$ [for Sedigraph, compare Supporting Information and Figure 4.SI 2].

4.3.3 Total carbon, total organic carbon and carbonate content

Total carbon (TC) and total organic carbon (TOC) were determined using freeze dried and homogenized bulk samples of cores GeoB6308-3 and GeoB6309-1 in 5 cm and 20 cm intervals, respectively. The samples were measured twice with the LECO CS200 element analyzer [*Bernard et al.*, 1995]. The first run defines the TC content. For determination of TOC, calcium carbonate was removed in advance of a second run by adding some aliquots of 0.25 N HCl. Calcium carbonate content was calculated according to the equation: $\text{CaCO}_3 = (\text{TC} - \text{TOC}) \times 8.33$.

4.4 Results

4.4.1 Age models

The resulting age model of core GeoB6308 from the Necochea Terrace covers the last ~ 19 cal ka BP (Figure 4.2) and represents linear sedimentation rates (LSR) of about 30 cm/ka during the deglacial period with a peak from 15 to 14 cal ka BP. Holocene LSR are comparably low (10 cm/ka). Investigated sediment sections of core GeoB6309-1, which is located at the slope, cover the last ~ 16.5 cal ka BP and presents lower LSR of 16 and 8 cm/ka during the deglacial and the Holocene, respectively (Figure 4.2).

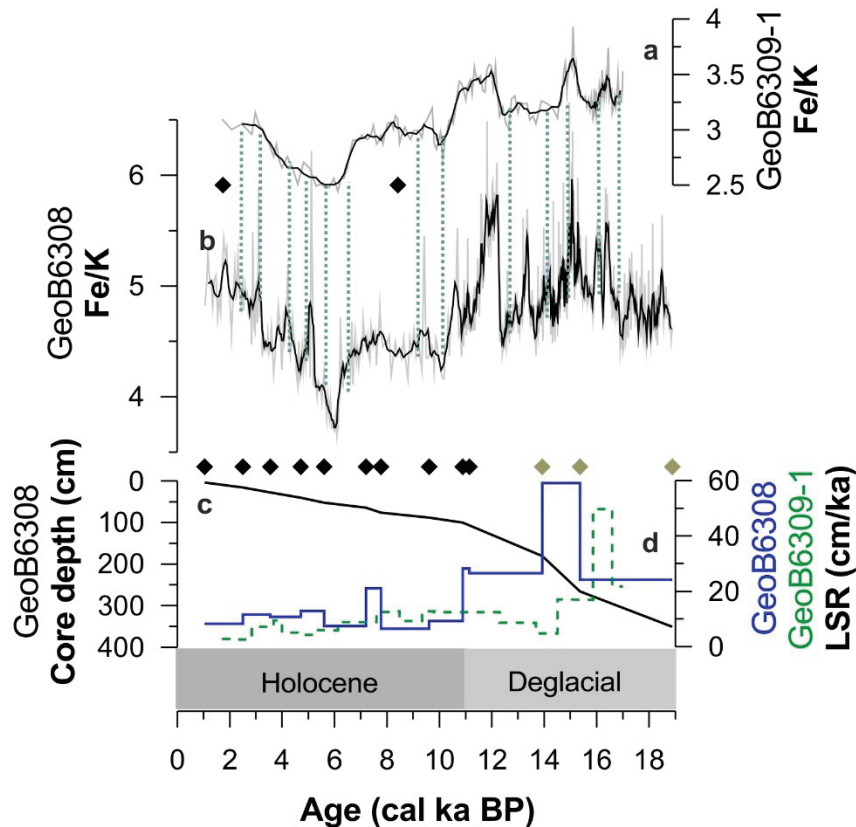


Figure 4.2: Age model of cores GeoB6308 and GeoB6309-1 based on AMS ^{14}C ages (planktonic foraminifera - black diamonds; total organic carbon - khaki rhombs) and XRF Fe/K downcore record tuning. **(a and b)** Fe/K records (grey line) of cores GeoB6309-1 and GeoB6308, also given as 5-point running mean (black line). Tie points are indicated as light green vertical dotted lines. **(c)** Age versus depth record of core GeoB6308 and **(d)** linear sedimentation rates (LSR) of cores GeoB6308 (blue) and GeoB6309-1 (green).

4.4.2 Sortable silt and grain-size measurements

The SS_{mean} of core GeoB6308 vary between 28 and 35 μm (Laser Coulter, Figure 4.3a). A pronounced peak in SS_{mean} occurs between ~ 15 and 11 cal ka BP. A minima is observed at 8 cal ka BP, whereas SS_{mean} increase again to 31 μm from 7 cal ka BP until present. The total terrigenous grain-size distribution support SS_{mean} variations with a pronounced maxima (i.e. 19% fine sand, Figure SI4.3) during the late deglaciation and lower values during the Holocene (i.e. 13% fine sand, Figure SI4.3). Magnetic susceptibility (MS, Figure 3b; for method see Supplement information) further support grain-size curve progression with increased terrigenous coarse-grain proportion during the late deglacial.

The late deglacial (at $\sim 15\text{ka}$) SS_{mean} increase indicates a change in current flow speed change (min/max) of 6.9-9.1 cm s^{-1} and a decline of 7 – 9.3 cm s^{-1} by 11 ka [McCave *et al.*, 2017].

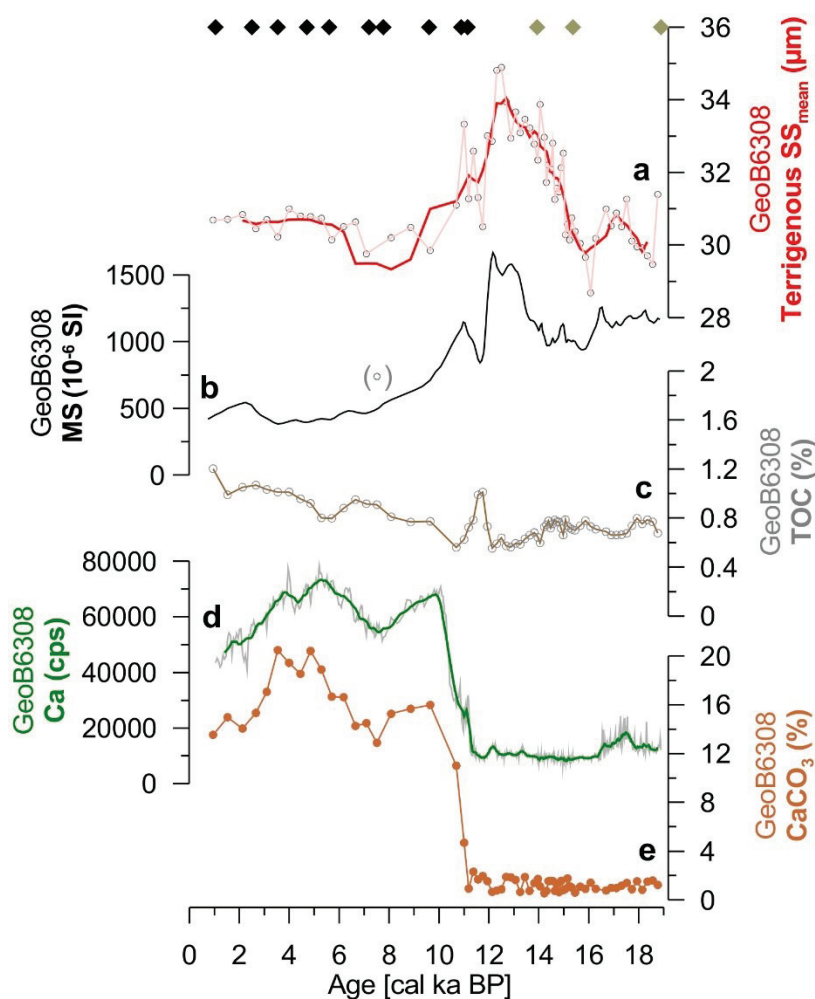


Figure 4.3: Grain-size dependent records of core GeoB6308. **(a)** Terrigenous sortable silt mean (SS_{mean}) measured with a Laser Coulter. One possible outlier at 7.5 cal ka BP is depicted in brackets. **(b)** Magnetic susceptibility (MS). **(c)** Total organic carbon (TOC). **(d)** XRF calcium (Ca) counts per second. **(e)** CaCO_3 content. Black (planktonic foraminifera AMS ^{14}C ages) and khaki diamonds (TOC AMS ^{14}C ages) indicate age control.

4.4.3 Total organic carbon and carbonate content

TOC of core GeoB6308 varies between 0.6 and 1.2 % and reveals a minor increase from the LGM until present (Figure 4.3c). Carbonate content of core GeoB6308 fluctuates from 0.5 to 2 % from ~ 19 until 11 cal ka BP and coincides with XRF Ca/Fe variations (Figure 4.3e and 4.4d). A fast and pronounced increase in CaCO_3 (to 15%) is present at 11 to 10 cal ka BP, which is stable until 6 cal ka BP (Figure 4.3e). A maximum in carbonate content (16-20 %) occurs from 6 until 3 cal ka BP, whereas CaCO_3 decreases to 12 % from 3 cal ka BP until the present.

GeoB6309 indicates a similar carbonate content trend by also showing a strong increase from 11 (< 1%) to 10 (13%) cal ka BP (Figure 4.4b), which is depicted by the Fe/Ca record in higher resolution (Figure 4.4c).

4.5 Discussion

4.5.1 Deglacial changes in deep water mass source reflected by carbonate content

Calcium carbonate was almost absent in both of our investigated sediment cores during the last deglacial period, which points to carbonate corrosion (Figure 4.4a to d). In the modern ocean, deep SCW is undersaturated in CO_3^{2-} leading to strong carbonate corrosion, whereas NADW is saturated in CO_3^{2-} resulting in carbonate preservation [Henrich *et al.*, 2003; Volbers and Henrich, 2004]. In contrast to the modern setting, calcite dissolved several hundred meters above the present level during the LGM due to the presence of a corrosive water mass below the NADW [e.g., Gröger *et al.*, 2003; Volbers and Henrich, 2004]. Hence, very low carbonate content indicates that the investigated cores were primarily affected by corrosion of glacial deep SCW during the deglacial period, i.e. until 11 cal ka BP. Such a glacial deep SCW dominance within the Atlantic Ocean was proposed by Lynch-Stieglitz *et al.* [2007], Freeman *et al.* [2016], and Lippold *et al.* [2016]. These studies have shown the presence of a shallow glacial NCW, allowing the SCW to develop below 2,000 m water depth. The rise in carbonate content at 11 cal ka BP (Figure 4.4a to f) would then indicate that glacial intermediate NCW developed into the modern NADW, spreading into the deep Southwest Atlantic at the expense of deep SCW.

The emplacement of NADW in the deep Southwest Atlantic should be accompanied by a change in sediment provenance. Indeed, bulk sediment neodymium isotopes of core GeoB6308 indicate a late deglacial/Holocene increase in northern sourced sediment delivery to the deep Argentine Margin [Lantzsch *et al.*, 2014], which corroborates our interpretation of a downward shift of the NCW/SCW interface and, thus, an increased contribution of NCW in more than 2,800m water depth abruptly increasing carbonate content from 1% to 20% by 11 cal ka BP (Figure 4.4a to f). Howe *et al.* [2016] provide additional evidences for a greater volume of deep SCW below 2,500 m water depth during the LGM compared to the Holocene situation. Howe *et al.* [2016] demonstrate that ~15 % and ~25 % NCW contribution reached a water depth of 3,700 m during LGM and Holocene, respectively. Furthermore, Skinner *et al.* [2013] report a rise in NCW contribution in 3,000 m water depth already since 12 cal ka BP (Figure 4.6d). The combination of these data support that the proportion of deep NCW was reduced in depths below ~ 2,000 m water depth and that corrosive deep SCW was the dominant endmember in the glacial and deglacial deep Southwest Atlantic [Böhm *et al.*, 2015; Curry and Oppo, 2005; Lippold *et al.*, 2016]. Then, the NCW/SCW interface shifted downwards during the late deglaciation affecting our deep sites (i.e., below ~ 2,800 m) at the Argentine Margin by 11 cal ka BP (Figure 4.4). Only since

11 cal ka BP, all core sites were bathed by a mixture of the deep SCW and minor proportions of deepened NCW, i.e., NADW, characterizing the NCW/SCW interface present today at around 3,000 m water depth as well [Stramma and England, 1999].

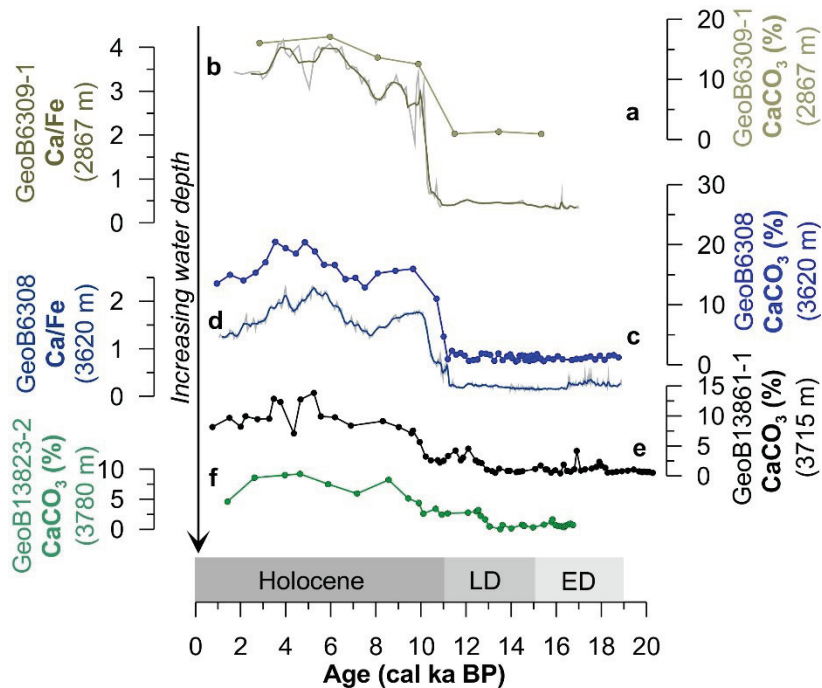


Figure 4.4: Carbonate content vertical transect covering water depths from ~ 2800 to 4000 m and displaying low (higher) carbonate values due to carbonate dissolution (preservation) of deep southern component water (Northern Component Water). **(a)** Calcium carbonate (CaCO₃) and **(b)** Ca/Fe downcore records of GeoB6309-1 (this study, thick line displays 5-point running mean). **(c)** CaCO₃ and **(d)** Ca/Fe records of GeoB6308 (this study, thick line displays 5-point running mean). **(e and f)** CaCO₃ of GeoB13861-1 and GeoB13823-2 from Warratz et al. [2017] (LD-Late deglacial, ED – Early deglacial).

4.5.2 Deglacial changes in deep water mass strength

The sortable silt record of core GeoB6308 from the Necochea Terrace contourite displays a period of increased SS_{mean} from 15 to 11 cal ka BP (Figure 4.5a). These increased SS_{mean} reflect a phase of strengthened deep SCW paleocurrent flow and present a flow speed change [McCave et al., 2017] of 8 cm s^{-1} (Figure 4.6a).

During the glacial period, lowered sea level may have reduced ISW as it depends on the existence of Antarctic ice shelves [Anderson et al., 2002]. The ice shelves were replaced by grounded ice masses that resulted in a decline of super-cooled water and deep SCW formation [Krueger et al., 2012]. Thus, glacial deep SCW was mainly formed through enhanced polynya activity along the Antarctic continental margin and brine rejection [Smith et al., 2010]. The deglacial sea level rise, in contrast, enhanced ISW-related deep SCW formation rates. This increase may have resulted in a late deglacial intensification in deep SCW flow strength as recorded in core GeoB6308 (Figure 4.5a and 4.6a). However, an intensification of ISW-related deep SCW formation would

imply comparably high current strengths during the Holocene, which would contrast the observed decrease in SS_{mean} (Figure 4.5a).

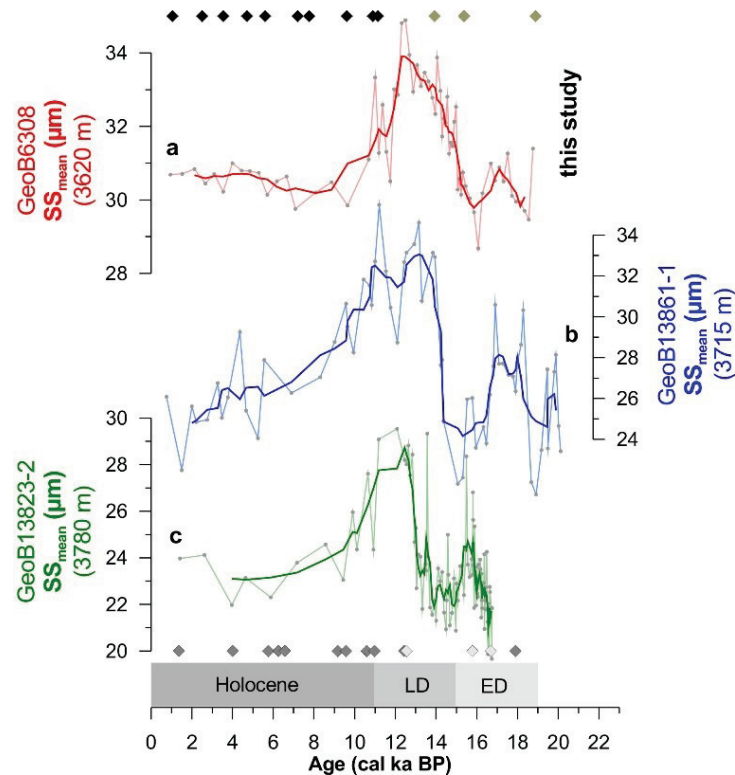


Figure 4.5: Terrigenous sortable silt paleocurrent records (SS_{mean}) from the Argentine Margin (from the shallowest to the deepest): **(a)** GeoB6308 (red, this study) with a SS_{mean} maximum from 15 to 11 cal ka BP, **(b)** GeoB13861-1 (blue), and **(c)** GeoB13823-2 (green, both Warratz et al. [2017]) with a SS_{mean} maximum from 14 to 10 cal ka BP. Thick colored lines display 5-point running mean.

Another factor contributing to a deglacial increase in deep SCW strength was given by *Roberts et al.* [2017]. This study presents a new SS_{mean} paleocurrent proxy (Figure 4.6e) responding to the strength of sub-Antarctic Frontal (SAF) jet, thereby indicating a strengthened Cold Water Route (ACC) through-flow since 14/15 ka [*Roberts et al.*, 2017]. Since 14/15 ka, the increased eustatic sea level and a transition to an in-phase SSTs upstream and downstream of the Drake Passage are consistent with a southward migration of the SAF (Figure 4.6e). This migration increases the inter-basin exchange between the Pacific and Atlantic [*Roberts et al.*, 2017]. The enhanced inter-basin exchange increased the low-salinity, low-density sub-Antarctic Mode Water (SAMW) flow into the Atlantic. This increased inflow, in turn, decreased AAIW density relative to NADW, producing a more stable AMOC [*Keeling and Stephens*, 2001]. Applying this scenario to the deep Argentine Margin, the southward shift of the SAF jet promoted the ACC and, thus, the CDW flow into the Southwest Atlantic [*Dinniman et al.*, 2011]. This development supports the late deglacial increase in CDW spreading since 15 ka. In addition, a late deglacial NADW re-initiation (section 4.5.1) and expansion in the Southwest Atlantic may have vertically narrowed deep SCW spreading (Figure 4.7a and 4.7b). A greater volume of NADW (Figure 4.7a and

4.7b), in turn, may have also enhanced LCDW formation, which is partly generated from modified NADW [Whitworth and Nowlin, 1987]. We relate such a deglacial increased LCDW inflow into the Southwest Atlantic to a simultaneous downward shift of the LCDW/AABW interface. Hence, the early deglacial LCDW/AABW interface was located above our core sites (Figure 4.7c). The NADW re-initiation and increased deep SCW inflow vertically deepened the LCDW/AABW interface occupying our core sites during the late deglacial (Figure 4.7b) and shifted further downwards during the Holocene (Figure 4.7a).

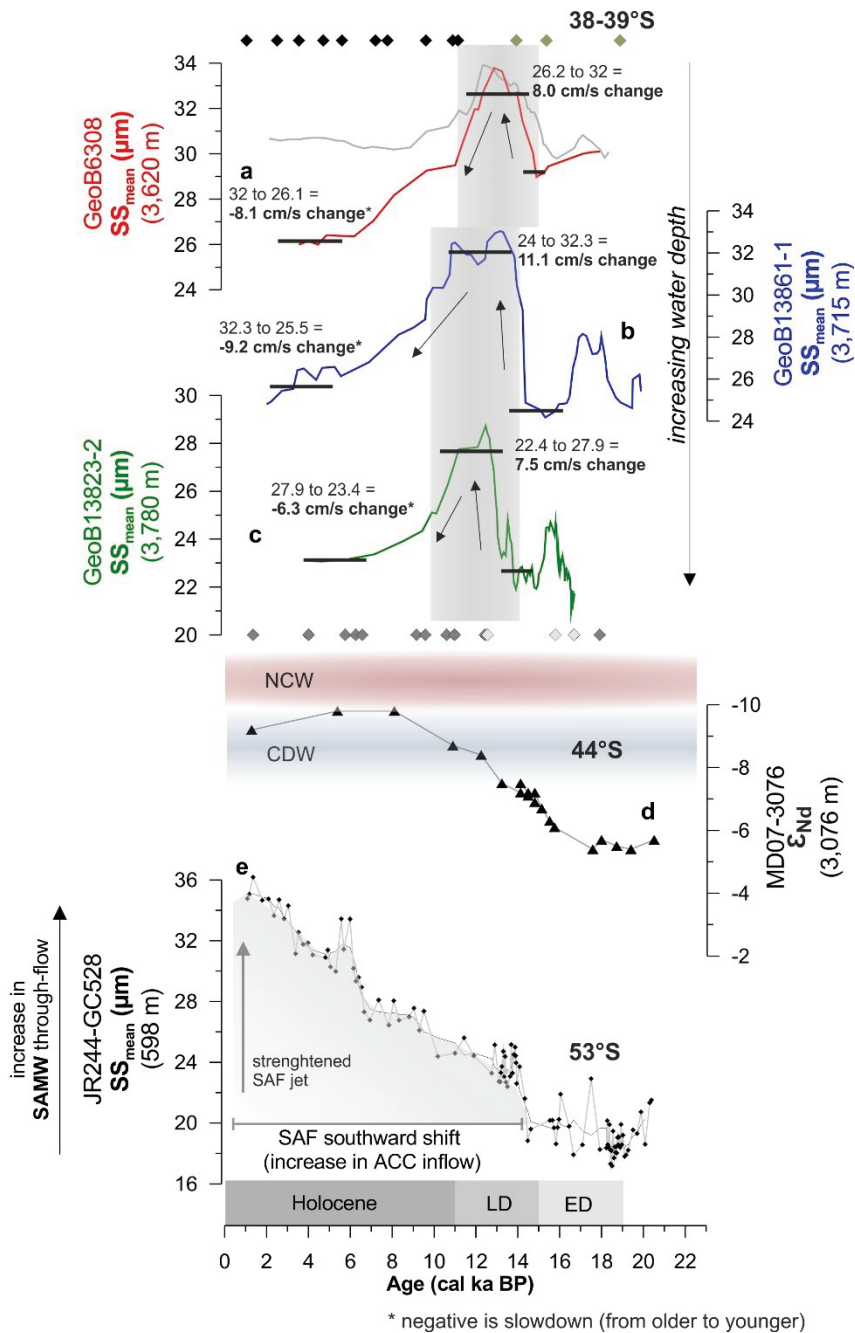


Figure 4.6: Paleocurrent strength proxy records displaying the vertical deepening of the LCDW/AABW interface. (a, b, and c) SS_{mean} 5-point running mean records (Sedigraph measurements) of three core locations at the Argentine Margin displaying increased current strength marking the deepening of the LCDW/AABW interface during the late deglacial. Changes in current strength sensitivity [McCave *et al.*,

2017] are indicated (Black and khaki diamonds at the top of panel (a) display pF and TOC ages of core GeoB6308, respectively; dark and light grey diamonds mark age control of cores GeoB13861-1 and GeoB13823-2, respectively). **(d)** MD07-3076 ϵ ND from Skinner *et al.* [2013] indicates an increasing NCW contribution in \sim 3000 m water depth since the late deglacial. **(e)** JR244-GC528 [Roberts *et al.*, 2017] indicates an increase of sub-Antarctic Frontal (SAF) jet strength enhancing low-density sub-Antarctic Mode Water (SAMW) export since 15 cal ka BP due to a southward shift of the SAF. This further led to enhanced Antarctic Circumpolar Current (ACC) flow into the South Atlantic (LD – late deglacial, ED – early deglacial).

The LCDW/AABW interface, located below the NCW/SCW interface, is suggested to be highly energetic resulting in higher current strength [Preu *et al.*, 2013]. This energetic zone is dominated by turbulent and intense bottom currents due to pycnoclines affected by diverse baroclinic activities, such as vertical mixing [Arhan *et al.*, 2002a; Cacchione *et al.*, 2002; Pomar *et al.*, 2012]. The energetic pattern is enforced by internal tides and internal waves, which have a tremendous effect on sediment dynamics and result in erosion at the water mass interface and deposition next to it [e.g., Hosegood and van Haren, 2003; Preu *et al.*, 2013]. Hence, increased SS_{mean} (Figure 4.6a) most probably reflect the proximity of the LCDW/AABW in core GeoB6308 from 15 to 11 cal ka BP (3620 m water depth). During the early deglacial (and Holocene), lower SS_{mean} values indicate a downward shift of the LCDW/AABW interface resulting in a weaker current strength (Figure 4.6a).

Two cores from the same contourite (GeoB13861-1 and GeoB13823-2; Figures 4.5b to 4.5c and 4.6b to 4.6c) show comparable deglacial and Holocene shifts in the LCDW/AABW interface [Warratz *et al.*, 2017]. Therefore, we suggest that a simultaneous deepening of the NCW/SCW and the underlying LCDW/AABW interface affected the three core sites (GeoB6308, GeoB13861-1, and GeoB13823-2) during the late deglacial (Figure 4.7b). Since that time, the LCDW//AABW interface shifted further downward and is located in about 4000-4200 m water depth at modern times (Figure 4.7a) [e.g., Arhan *et al.*, 2002b; Piola and Matano, 2001].

The three aforementioned cores (GeoB6308, GeoB13861-1, and GeoB13823-2) stem from the same contourite system in water depths ranging from 3600 to 3800 m (Figure 4.6a to 4.6c). Despite these similarities, the shallowest core GeoB6308 displays highest current velocities from 15 to 11 cal ka BP, thereby showing an earlier strengthening than the two deeper core sites where velocities were intensified from 14 to 10 cal ka BP (Figure 4.6a to 4.6c) [Warratz *et al.*, 2017]. This offset points towards a successive deepening of the glacial LCDW/AABW interface (Figure 4.7a to 4.7c), but further studies are needed to prove this investigation.

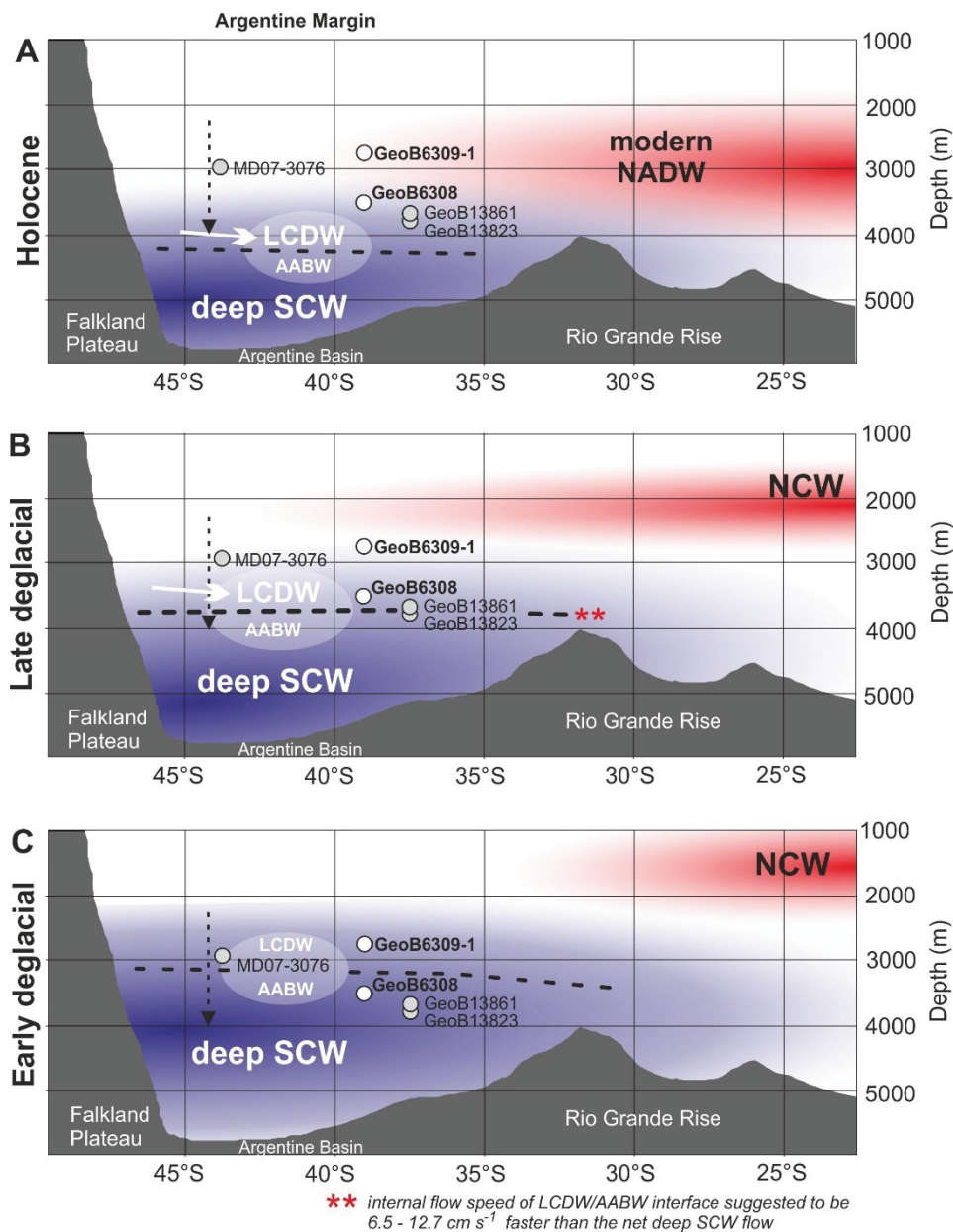


Figure 4.7: Schematic evolution of deep southern component water (SCW) in the Southwest Atlantic during the (a) Holocene, (b) late deglacial and (c) early deglacial. Modern North Atlantic Deep Water (red) spreading into the Southwest Atlantic vertically narrows the deep SCW spreading (blue), thereby deepening the LCDW/AABW interface (black dotted line).

4.6 Conclusions

Our knowledge about deep SCW in the Southwest Atlantic is fragmented due to the lack of appropriate paleoceanographic archives due to strong carbonate corrosivity. The suite of cores from the Argentine Margin investigated here, overcome this obstacle providing new insights into the vertical shift of the deep NCW/SCW and the LCDW/AABW interfaces. The investigated sediment cores were collected from the Necochea Terrace contourite, where continuous sedimentation supports detailed paleoceanographic reconstructions. Four coherent carbonate content

records spanning 2,800 to 4,000 m water depth indicate enhanced values since 11 cal ka BP. We can hypothesize that the increased influence of NADW at the expense of deep SCW at this water depth range improved carbonate preservation. This was most probably related to a slight deepening of the NCW/SCW interface from the late deglacial until the Holocene. Additionally, three coherent SS_{mean} records ranging from 3,800 to 3,600 m water depth reveal a peak in current strength between 15 and 11 cal ka BP. We suggest that this peak characterizes the LCDW/AABW interface, which is suggested to be an energetic interface producing high current strength. For the first time, we are able to identify a downward shift in the LCDW/AABW interface due (i) to NCW deepening at the expense of deep SCW spreading and (ii) enhanced LCDW inflow into the deep Southwest Atlantic during the late deglacial. The latter might be caused by the SAF southward shift within the Drake Passage by 15 ka, which in turn increased ACC inflow. During the LCDW/AABW downward shift, the interface reaches the shallowest (deepest) core site by 15 (14) cal ka BP and shifts further downward in the water column.

Acknowledgement

This study was funded through the DFG-Research Center/Cluster of Excellence “The Ocean in the Earth System” (MARUM) and was supported by GLOMAR-Bremen International Graduate School for Marine Sciences. We acknowledge T. Bickert for contributing XRF data of GeoB6309-1, which were produced in the frame of a Bachelor thesis. This research used data acquired at the XRF Core Scanner Lab at the MARUM. IV further acknowledges the support from DFG grant VO2094/1-1. C.M. Chiessi acknowledges the financial support from FAPESP (grant 2012/17517-3), CAPES (grant 564/2015) and CNPq (grants 302607/2016-1 and 422255/2016-5). New data reported in this paper will be achieved in PANGAEA (www.pangaea.de).

Supplementary Information

Methods

Age model comparison of GeoB6308 with and without reservoir age

Table 4.SI 1: Comparison of reservoir age uncorrected (blue) and corrected (red) TOC AMS ^{14}C ages used to compile the age model of cores GeoB6308 (compare Figure 4.SI 1).

Core depth (cm)	Material	Radiocarbon age (yr BP) \pm error	Calibration without ΔR		Calibration with $\Delta R = 1035 \pm 200$	
			1σ calibrated age range (cal a BP)	Calibrated age (cal ka BP)	1σ calibrated age range (cal a BP)	Calibrated age (cal ka BP)
Beta-341847	181 TOC	13490 \pm 50	15606-15798	15,702	13641-14215	13,928
Beta-341848	266 TOC	14280 \pm 60	16679-16950	16,8145	15011-15722	15,3665
Beta-341849	351 TOC	17060 \pm 70	19985-20204	20,0945	18654-19118	18,886

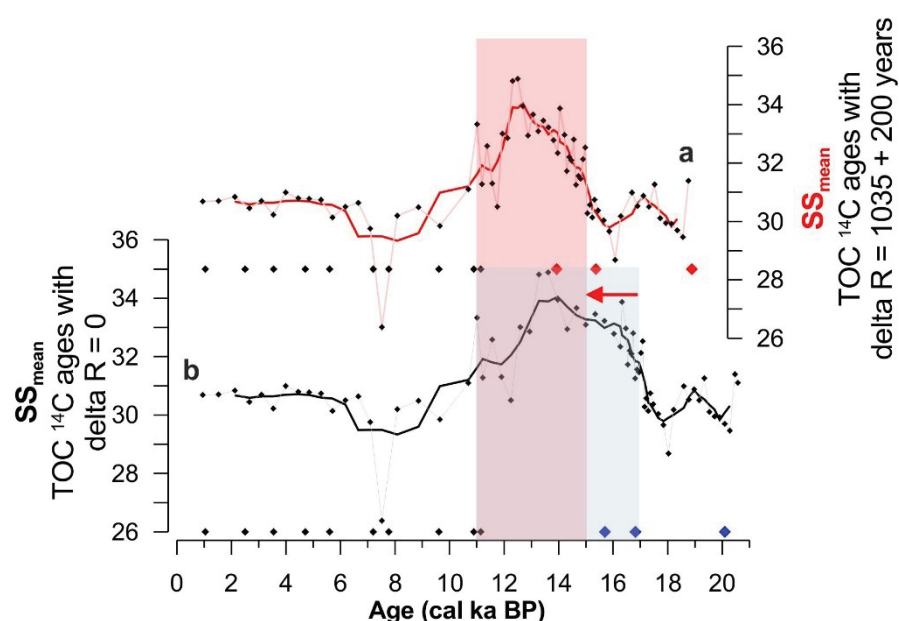


Figure 4.SI 1: Comparison of sortable silt (SS_{mean}) results applying **(a)** the age model of this study (red diamonds) and **(b)** an age model disregarding an additional TOC ^{14}C reservoir age of 1035 ± 200 (blue diamonds) [Mollenhauer et al., 2006]. AMS ^{14}C ages based on planktonic foraminifera (black diamonds) are similar in both age models. Both timelines show a difference of 2,000 years for the increase of the SS_{mean} peak.

X-ray Fluorescence

High resolution X-ray fluorescence (XRF) scans (element intensities in counts per second; cps) of GeoB6308-3 (GeoB6309-1) were performed with an AVAATECH XRF core scanner on split cores at 0.5 (1.0) cm intervals. Fe/K ratios were used to tune the age models. Ca/Fe variations were

used to display relative calcium carbonate fluctuations in higher resolution than measured carbonate contents.

Magnetic Susceptibility

Magnetic susceptibility (MS) of GeoB6308-3 was measured on-board [Frederichs and Bleil, 2001] using the GEOTEK Multi Sensor Core Logger (MSCL, whole round). The logger is equipped with a MS coil sensor (Bartington MS2C, diameter 140 mm) and an effective resolution of $2 \times 10E-6$ SI.

Justification of Grain-size Measurements

McCave *et al.* [2006] stated that Laser diffraction measurements might be influenced by potential particle shape effects. However, Goossens [2008] added that there is no optimum technique to measure grain-size distribution of fine grained sediments, but that different techniques and devices generally result in similar trends. Accordingly, laser diffraction particle sizing is well suited for paleoceanographic reconstructions as it shows high correlation with values measured with the Sedigraph [Jonkers *et al.*, 2009]. In our case, Sedigraph and Laser Coulter resulted in similar SS_{mean} values with a good correlation (Figure 4.SI 2). In addition, our results support the application of different SS_{mean} measured with diverse measurement principles, i.e., Sedigraph (GeoB13861-1 and GeoB13823-2) and Laser Coulter (GeoB6308-3). Importantly, Jonkers *et al.* [2009] proposed the accuracy of Laser Coulter for sortable silt measurement.

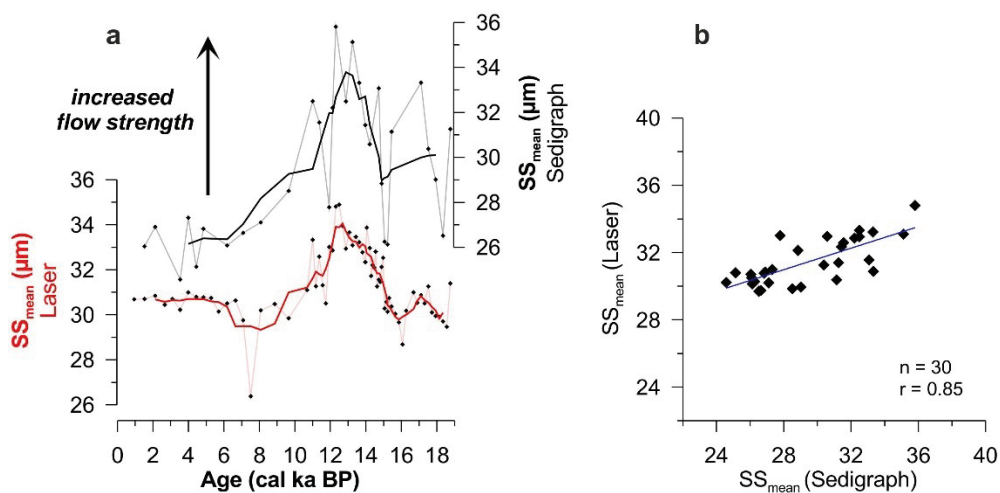


Figure 4.SI 2: (a) Sortable silt mean values measured with Laser Coulter and Sedigraph showing similar values that support the use of the highly reproducible Laser Coulter measurements for sortable silt analyses. (b) High correlation of Sedigraph and Laser SS_{mean} ($r=0.85$).

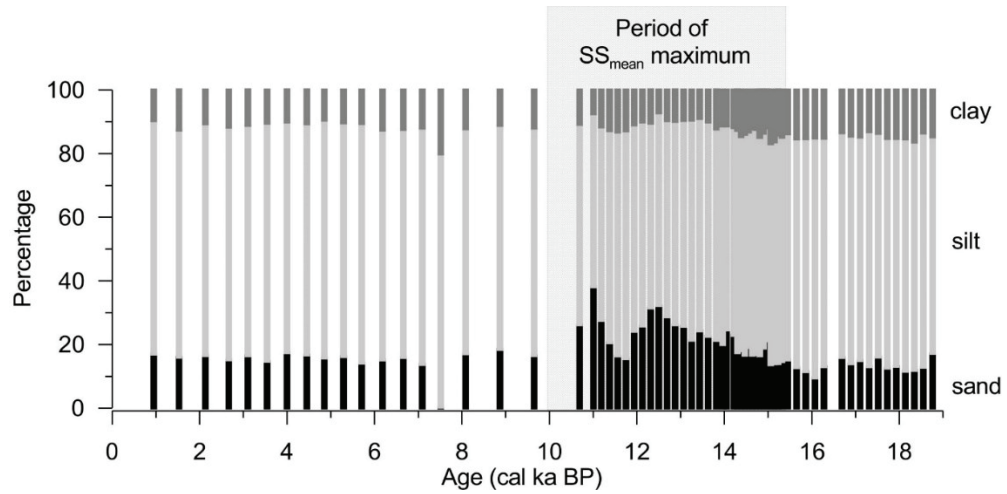


Figure 4.SI 3: Terrigenous grain-size distribution showing percentages of fine sand, silt and clay fractions. Period of increased SS_{mean} values are indicated and corresponds to period of SS_{mean} maximum.

This page was intentionally left blank.

Chapter 5

Conclusions and future perspectives

Deglacial re-organization of deep water mass distribution

(I) The reconstruction of deep Southwest Atlantic circulation during the last 20,000 years by three source-proximal deep SCW paleocurrent records indicate a continuous terrigenous sediment discharge of the deep SCW nepheloid layer along the Necochea Terrace since the Last Glacial Maximum. This consistent deep SCW nepheloid layer was able to construct contourite drift deposits along this terrace.

- *This deep SCW nepheloid layer was continuously present in more than 3600 m water depth during the last 20,000 years.*

(II) Since the deglacial period, carbonate variability, observed in four deep core sites, indicates that the NCW/SCW interface shifted downward in the water column. Especially between 20 and 11 cal ka BP, an intermediate NCW left space for deep SCW expansion, which in fact reduced carbonate preservation at all deep core sites. Additionally, the NCW/SCW interface migrated downward in the water column at ca. 11 cal ka BP.

- *The NCW/SCW interface deepening was detected during the late deglacial and carbonate content notably increased in > 3600 m water depth at 11 ka.*

(III) The deglacial shift of deep SCW was identified by classifying the energetic LCDW/AABW interface along the deep Argentine continental margin. The identification of this high energetic interface was based on the sortable silt paleocurrent proxy. Based on the deepening of the NCW/SCW interface from the late deglacial until the Holocene, the data set provides further support that the energetic LCDW/AABW interface shifted downward in the water column.

- *The deglacial deepening of the NCW/SCW interface progressively affected the LCDW/AABW interface.*

Reconstruction of deep southern component water strength

(IV) Increased deep SCW flow strength from 14 to 10 cal ka BP (late deglacial) was shown by consistent records, although a glacial/interglacial variability was not recorded. The increased deep SCW flow may have been a response to enhanced production rate of AABW and LCDW or, more likely, a result of modern (deep) NADW re-initiation, narrowing the deep SCW spreading.

NADW re-initiation was accompanied by a vertical migration of the LCDW/AABW interface, represented as a high-energetic interface, creating intense bottom currents.

- *The rise of deep SCW flow strength during the late deglacial can be related to the energetic LCDW/AABW interface therein.*

(V) The shift of the LCDW/AABW interface, creating strong bottom currents, occurred from 3,600 to 3,800 m during the late deglacial period and shifted further downwards during the Holocene. The shallowest core (3600 m) displays strongest current velocities from 15 to 11 cal ka BP, thereby showing a strengthening earlier than the two deeper core sites (3700-3800 m), in which velocities were intensified from 14 to 10 cal ka BP. This offset points towards a successive deepening of the glacial LCDW/AABW interface. These findings support the deglacial re-organization of the deep Southwest Atlantic by identifying the deep SCW deepening.

- *The energetic LCDW/AABW interface was detected from 3,600 to 3,800 m water depth at 15 to 10 ka and supports a downward shift from the deglacial period towards the Holocene.*

Contourite-turbidite interaction within a blind canyon system

(VI) During the LGM and early deglacial, turbidity current activity was pronounced within the entire canyon. Part of the gravity-driven sediments from the distal canyon thalweg were captured by the deep SCW, carried northward and finally deposited at the northern canyon flank. During the late deglacial, very fine sand turbidites were not as extensive as before.

- *Turbidity current activity within the Mar del Plata Canyon was restricted to the last glacial and deglacial period.*

(VII) Mineralogical and sedimentological classifications of turbidite deposits and contouritic sediments from the Ewing Terrace have shown that sandy-silty contourites were the main source for down-slope currents during the glacial period. The glacial turbidite activity further implies that AAIW nepheloid layer discharge along the Ewing Terrace varied through time.

- *The Ewing Terrace contourite deposit was the main source of glacial turbidity currents and created a contourite-turbidite interaction in the blind Mar del Plata Canyon.*

Influence of Antarctic Intermediate Water on slope instabilities

(VIII) From the LGM to 10 cal ka BP, rapid drift accumulation along the Ewing Terrace was forced by the AAIW nepheloid layer building up sediments in the canyon head area. V-shaped incisions and amphitheater-like scars in the canyon head area imply that turbidity current generation may be related to instability processes, i.e. retrogressive erosion or canyon flank failures. Specific knickpoints, restricted to the uppermost canyon thalweg, acted as hydraulic jumps to transform

sediment slides into turbidity currents. However, these mechanisms progressively slowed down during the late deglacial until turbidites totally disappeared during the Holocene. This contourite-turbidite conversion further classifies the role of AAIW flow variability during the last 20,000 years.

- *The AAIW nepheloid layer sediment supply is the main trigger for turbidity currents generated by instabilities in the canyon head area.*

(IX) The blind Mar del Plata Canyon supports the hypothesis of enhanced glacial contourite deposition as the main trigger for slope instabilities due to pore pressure in excess. The instability potential was most probably related to a shallowed glacial AAIW or increased AAIW nepheloid layer sediment supply to the canyon head area. During the Holocene, in contrast, AAIW nepheloid layer discharge progressively slowed down and decreased sediment failure potential.

- *Turbidity current activity reinforces an enhanced or shallowed AAIW nepheloid layer during the glacial and deglacial periods.*

Future perspectives

The new findings of the deglacial Southwest Atlantic re-arrangement, comprising an increased deglacial deep SCW flow, and the effect of AAIW nepheloid layer discharge show that contour currents have a tremendous effect on sedimentation and slope architecture. The Argentine continental margin is a representative regional example for the interaction of along- and down-slope sediment transports processes at continental margins. Important future tasks will be the comparison of these results with other continental margins affected by major water masses. Further key scientific questions regarding the study of continental slopes and the deep Southwest Atlantic circulation are:

- Is it possible to detect the LCDW/AABW interface farther north or south along the South American continental margin between 3,500 and 4,000 m water depth?
- How did the AAIW current strength change during the last glacial/interglacial cycle? Is it possible to generate source-proximal paleocurrent records covering the last 20,000 years?
- How do other blind canyons interact with deep western boundary currents along the South American continental margin?

An upcoming research cruise to the Argentine/Uruguay continental margin in January and February 2018 (SO260) will provide a new comprehensive data set, comprising sediment cores and hydro-acoustic/seismic data. I will participate in this cruise and hope that we can receive a gravity core covering at least the last 20,000 years, e.g., from the small terrace of the Mar del

Plata Canyon (compare Chapter 3, ParaSound profile in Figure 3.8). This terrace covers undisturbed sedimentation of the last 20,000 years and is currently bathed by the NADW. However, the sediments were supposed to be delivered by the AAIW nepheloid layer crossing the canyon. This continuous sedimentation might provide the opportunity to use these sediments as a paleoceanographic archive for the interaction of AAIW, UCDW, NADW and LCDW since the LGM.

References

- Adkins, J. F. (2013), The role of deep ocean circulation in setting glacial climates, *Paleoceanography*, 28(3), 539-561, doi:10.1002/palo.20046.
- Anderson, J. B., S. S. Shipp, A. L. Lowe, J. S. Wellner, and A. B. Mosola (2002), The Antarctic Ice Sheet during the Last Glacial Maximum and its subsequent retreat history: a review, *Quaternary Science Reviews*, 21(1), 49-70, doi: 10.1016/S0277-3791(01)00083-X.
- Anderson, R. F., S. Ali, L. I. Bradtmiller, S. H. H. Nielsen, M. Q. Fleisher, B. E. Anderson, and L. H. Burckle (2009), Wind-Driven Upwelling in the Southern Ocean and the Deglacial Rise in Atmospheric CO₂, *Science*, 323(5920), 1443-1448, doi:10.1126/science.1167441.
- Arhan, M., X. Carton, A. Piola, and W. Zenk (2002a), Deep lenses of circumpolar water in the Argentine Basin, *Journal of Geophysical Research: Oceans*, 107(C1), 7-1-7-12, doi:10.1029/2001JC000963.
- Arhan, M., A. C. N. Garabato, K. J. Heywood, and D. P. Stevens (2002b), The Antarctic Circumpolar Current between the Falkland Islands and South Georgia, *Journal of Physical Oceanography*, 32(6), 1914-1931, doi:10.1175/1520-0485(2002)032<1914:taccbt>2.0.co;2.
- Arhan, M., H. Mercier, and Y.-H. Park (2003), On the deep water circulation of the eastern South Atlantic Ocean, *Deep Sea Research Part I: Oceanographic Research Papers*, 50(7), 889-916, doi:10.1016/S0967-0637(03)00072-4.
- Bard, E., T. Tuna, Y. Fagault, L. Bonvalot, L. Wacker, S. Fahrni, and H.-A. Synal (2015), AixMICADAS, the accelerator mass spectrometer dedicated to 14 C recently installed in Aix-en-Provence, France, *Nuclear Instruments and Methods in Physics Research Section B: Beam Interactions with Materials and Atoms*, 361, 80-86, doi: 10.1016/j.nimb.2015.01.075.
- Barker, P. F., and E. Thomas (2004), Origin, signature and palaeoclimatic influence of the Antarctic Circumpolar Current, *Earth-Science Reviews*, 66(1-2), 143-162, doi:10.1016/j.earscirev.2003.10.003.
- Barker, S., G. Knorr, M. J. Vautravers, P. Diz, and L. C. Skinner (2010), Extreme deepening of the Atlantic overturning circulation during deglaciation, *Nature Geosci*, 3(8), 567-571, doi:doi:10.1038/ngeo921.
- Berger, W., V. Smetacek, and G. Wefer (1989), Ocean productivity and paleoproductivity - an overview, in *Productivity of the ocean: present and past*, vol. 44, pp. 1-34.
- Bernard, B. B., H. Bernard, and J. M. Brooks (1995), *Determination of total carbon, total organic carbon and inorganic carbon in sediments*, vol. 1-5, TDI-Brooks International/ B&B Laboratories Inc. College Station, Texas.
- Bernhardt, A., D. Hebbeln, M. Regenberg, A. Lückge, and M. R. Strecker (2016), Shelfal sediment transport by an undercurrent forces turbidity-current activity during high sea level along the Chile continental margin, *Geology*, 44(4), 295-298, doi: 10.1130/G37594.1.
- Bianchi, G. G., and I. N. McCave (1999), Holocene periodicity in North Atlantic climate and deep-ocean flow south of Iceland, *Nature*, 397(6719), 515-517.
- Bindoff, N. L., M. A. Rosenberg, M. J. Warner (2000), On the circulation and water masses over the Antarctic continental slope and rise between 80 and 150°E, *Deep Sea Research Part II: Tropical Studies in Oceanography*, 47(12-13), 2299-2326, doi:10.1016/S0967-0645(00)00038-2.
- Biscaye, P. E. (1965), Mineralogy and Sedimentation of Recent Deep-Sea Clay in the Atlantic Ocean and Adjacent Seas and Oceans, *Geol. Society of Amer. Bull.*, 76(7), 803-832, doi:10.1130/0016-7606(1965)76[803:masord]2.0.co;2.
- Biscaye, P. E., and S. L. Eitrem (1977), Suspended Particulate Loads and Transports in the Nepheloid Layer of the Abyssal Atlantic Ocean, *Marine Geology*, 23, 155-172, doi:10.1016/00253227(77)90087-1.
- Blasi, A., and M. J. Manassero (1990), The Colorado River of Argentina: Source, climate, and transport as controlling factors on sand composition, *Journal of South American Earth Sciences*, 3(1), 65-70, doi: 10.1016/0895-9811(90)90018-V.
- Bleil, U., A. Alin, T. Bickert, W. Böke, M. Breitzke, D. S. E. E. T. Frederichs, et. al. (2001), Report and preliminary results of Meteor-cruise M46/3, *Berichte aus dem Fachbereich für Geowissenschaften, Universität Bremen*, 172, 161.

- Böhm, E., J. Lippold, M. Gutjahr, M. Frank, P. Blaser, B. Antz, J. Fohlmeister, N. Frank, M. B. Andersen, and M. Deininger (2015), Strong and deep Atlantic meridional overturning circulation during the last glacial cycle, *Nature*, *517*(7532), 73-76, doi:10.1038/nature14059.
- Bond, G., W. Broecker, S. Johnsen, J. McManus, L. Labeyrie, J. Jouzel, and G. Bonani (1993), Correlations between climate records from North Atlantic sediments and Greenland ice, *Nature*, *365*(6442), 143-147.
- Boning, C. W., A. Dispert, M. Visbeck, S. R. Rintoul, and F. U. Schwarzkopf (2008), The response of the Antarctic Circumpolar Current to recent climate change, *Nature Geosci.*, *1*(12), 864-869.
- Bouma, A. H., P. H. Kuenen, and F. P. Shepard (1962), *Sedimentology of some flysch deposits: a graphic approach to facies interpretation*, Elsevier Pub. Co., New York, Amsterdam.
- Bouma, A. H. (1978), X-ray radiography, in *Sedimentology, Encyclopedia of Earth Science*, pp. 1279-1280, Springer, Berlin Heidelberg, doi:10.1007/3-540-31079-7_250.
- Boyle, E. A., and L. Keigwin (1987), North Atlantic thermohaline circulation during the past 20, 000 years linked to high-latitude surface temperature, *Nature*, *330*(6143), 35-40.
- Boyle, E. A., and L. D. Keigwin (1982), Deep circulation of the North Atlantic over the last 200,000 years: Geochemical evidence, *Science*, *218*(4574), 784-787.
- Bozzano, G., R. A. Violante, and M. E. Cerredo (2011), Middle slope contourite deposits and associated sedimentary facies off NE Argentina, *Geo-Marine Letters*, *31*(5), 495-507, doi:10.1007/s00367-011-0239-x.
- Brackenkridge, R. E., F. J. Hernández-Molina, D. A. V. Stow, and E. Llave (2013), A Pliocene mixed contourite-turbidite system offshore the Algarve Margin, Gulf of Cadiz: Seismic response, margin evolution and reservoir implications, *Marine and Petroleum Geology*, *46*, 36-50, doi: 10.1016/j.marpetgeo.2013.05.015.
- Broecker, W. S., et al. (1998), How much deep water is formed in the Southern Ocean?, *Journal of Geophysical Research: Oceans*, *103*(C8), 15833-15843, doi:10.1029/98JC00248.
- Burone, L., et al. (2013), A multiproxy study between the Río de la Plata and the adjacent South-western Atlantic inner shelf to assess the sediment footprint of river vs. marine influence, *Continental Shelf Research*, *55*, 141-154, doi: 10.1016/j.csr.2013.01.003.
- Cacchione, D. A., L. F. Pratson, and A. S. Ogston (2002), The Shaping of Continental Slopes by Internal Tides, *Science*, *296*(5568), 724-727, doi:10.1126/science.1069803.
- Callahan, J. E. (1972), The structure and circulation of deep water in the Antarctic, *Deep Sea Research and Oceanographic Abstracts*, *19*(8), 563-575, doi: 10.1016/0011-7471(72)90040-X.
- Came, R. E., D. W. Oppo, W. B. Curry, and J. Lynch-Stieglitz (2008), Deglacial variability in the surface return flow of the Atlantic meridional overturning circulation, *Paleoceanography*, *23*(1), doi: 10.1029/2007PA001450.
- Cavallotto, J. L., R. A. Violante, and G. Parker (2004), Sea-level fluctuations during the last 8600 years in the de la Plata river (Argentina), *Quaternary International*, *114*(1), 155-165, doi: 10.1016/S1040-6182(03)00050-8.
- Channell, J. E. T., R. J. Harrison, I. Lascu, I. N. McCave, F. D. Hibbert, and W. E. N. Austin (2016), Magnetic record of deglaciation using FORC-PCA, sortable-silt grain size, and magnetic excursion at 26 ka, from the Rockall Trough (NE Atlantic), *Geochemistry, Geophysics, Geosystems*, *17*(5), 1823-1841, doi:10.1002/2016GC006300.
- Chelton, D. B., M. G. Schlax, D. L. Witter, and J. G. Richman (1990), Geosat altimeter observations of the surface circulation of the Southern Ocean, *Journal of Geophysical Research: Oceans*, *95*(C10), 17877-17903, doi:10.1029/JC095iC10p17877.
- Chiessi, C. M. (2008), Ocean circulation and climate variability in the western South Atlantic and eastern South America during the last deglaciation, *Dissertation*, Universität Bremen.
- Curry, W. B., and G. P. Lohmann (1983), Reduced advection into Atlantic Ocean deep eastern basins during last glaciation maximum, *Nature*, *306*(5943), 577-580.
- Curry, W. B., and D. W. Oppo (2005), Glacial water mass geometry and the distribution of $\delta^{13}\text{C}$ of ΣCO_2 in the western Atlantic Ocean, *Paleoceanography*, *20*(1), doi:10.1029/2004PA001021.
- Dalla Salda, L., L. Spalletti, D. Poiré, R. De Barrio, H. Echeveste, and A. Benialgo (2006), Tandilia, *Serie correlación geológica*, *21*(1), 17-46.
- de Mahiques, M. M., M. G. Tessler, A. Maria Ciotti, I. C. A. da Silveira, S. H. d. M. e Sousa,

- R. C. L. Figueira, C. C. G. Tassinari, V. V. Furtado, and R. F. Passos (2004), Hydrodynamically driven patterns of recent sedimentation in the shelf and upper slope off Southeast Brazil, *Continental Shelf Research*, *24*(15), 1685-1697, doi: 10.1016/j.csr.2004.05.013.
- Dearing, J. A., R. Dann, K. Hay, J. Lees, P. Loveland, B. A. Maher, and K. O'grady (1996), Frequency-dependent susceptibility measurements of environmental materials, *Geophysical Journal International*, *124*(1), 228-240, doi: 10.1111/j.1365-246X.1996.tb06366.x
- Diekmann, B., and G. Kuhn (1999), Provenance and dispersal of glacial-marine surface sediments in the Weddell Sea and adjoining areas, Antarctica: ice-rafting versus current transport, *Marine Geology*, *158*(1-4), 209-231, doi:10.1016/S0025-3227(98)00165-0.
- Diekmann, B., and G. Kuhn (2002), Sedimentary record of the mid-Pleistocene climate transition in the southeastern South Atlantic (ODP Site 1090), *Palaeogeography, Palaeoclimatology, Palaeoecology*, *182*(3-4), 241-258, doi: 10.1016/S0031-0182(01)00498-9.
- Diekmann, B., G. Kuhn, V. Rachold, A. Abelmann, U. Brathauer, D. K. Fütterer, R. Gersonde, and H. Grobe (2000), Terrigenous sediment supply in the Scotia Sea (Southern Ocean): response to Late Quaternary ice dynamics in Patagonia and on the Antarctic Peninsula, *Palaeogeography, Palaeoclimatology, Palaeoecology*, *162*(3-4), 357-387, doi:10.1016/S0031-0182(00)00138-3.
- Diekmann, B., R. Petschick, F. X. Gingele, D. K. Fütterer, A. Abelmann, U. Brathauer, R. Gersonde, and A. Mackensen (1996), Clay Mineral Fluctuations in Late Quaternary Sediments of the Southeastern South Atlantic: Implications for Past Changes of Deep Water Advection, in *The South Atlantic: Present and Past Circulation*, edited by G. Wefer, W.H. Berger, G. Siedler and D.J. Webb, pp. 621-644, Springer Berlin Heidelberg, doi:10.1007/978-3-642-80353-6_31.
- Dinniman, M. S., J. M. Klinck, and W. O. Smith Jr (2011), A model study of Circumpolar Deep Water on the West Antarctic Peninsula and Ross Sea continental shelves, *Deep Sea Research Part II: Topical Studies in Oceanography*, *58*(13-16), 1508-1523, doi: 10.1016/j.dsr2.2010.11.013.
- Dittert, N., K.H. Baumann, T. Bickert, R. Henrich, R. Huber, H. Kinkel and H. Meggers (1999), Carboante dissolution in the deep-sea: Methods, quantification and paleoceanographic application, in *Use of Proxies in Paleoceanography: Examples from the South Atlantic*, edited by G. Fischer and G. Wefer, 255-284, Springer, Berlin.
- Duplessy, J. C., N. Shackleton, R. Fairbanks, L. Labeyrie, D. Oppo, and N. Kallel (1988), Deepwater source variations during the last climatic cycle and their impact on the global deepwater circulation, *Paleoceanography*, *3*(3), 343-360, doi: 10.1029/PA003i003p00343.
- Ehrmann, W. U., M. Melles, G. Kuhn, and H. Grobe (1992), Significance of clay mineral assemblages in the Antarctic Ocean, *Marine Geology*, *107*(4), 249-273, doi:10.1016/0025-3227(92)90075-S.
- Ellwood, B. B., and M. T. Ledbetter (1977), Antarctic bottom water fluctuations in the Vema Channel: Effects of velocity changes on particle alignment and size, *Earth and Planetary Science Letters*, *35*(2), 189-198, doi: 10.1016/0012-821X(77)90121-2.
- Esquevin, J. (1969), Influence de la composition chimique des illites sur leur cristallinité. *Bull. Centre Rech. Pau-SNPA*, *3*(1), 147-153.
- Ewing, M., and A. G. Lonardi (1971), Sediment transport and distribution in the Argentine Basin. 5. Sedimentary structure of the Argentine margin, basin, and related provinces, *Physics and Chemistry of the Earth*, *8*, 125-251, doi:10.1016/0079-1946(71)90017-6.
- Faugères, J.-C., and D. A. V. Stow (1993), Bottom-current-controlled sedimentation: a synthesis of the contourite problem, *Sedimentary Geology*, *82*(1), 287-297, doi: 10.1016/0037-0738(93)90127-Q.
- Fischer, G., V. Ratmeyer, and G. Wefer (2000), Organic carbon fluxes in the Atlantic and the Southern Ocean: relationship to primary production compiled from satellite radiometer data, *Deep Sea Research Part II: Topical Studies in Oceanography*, *47*(9), 1961-1997, doi:10.1016/S0967-0645(00)00013-8.
- Flood, R. D., and A. N. Shor (1988), Mud waves in the Argentine Basin and their relationship to regional bottom circulation patterns, *Deep Sea Research Part A. Oceanographic Research Papers*, *35*(6), 943-971, doi: 10.1016/0198-0149(88)90070-2.
- Foldvik, A., T. Gammelsrød, and T. Tørresen (1985), Circulation and Water Masses on the Southern Weddell Sea Shelf, in *Oceanology of the Antarctic Continental Shelf*, edited by S.S. Jacobs, pp. 5-20, American Geophysical Union, doi:10.1029/AR043p0005.

- Foldvik, A., and T. Gammelsrød. (1988), Notes on Southern Ocean hydrography, sea-ice and bottom water formation, *Palaeogeography, Palaeoclimatology, Palaeoecology*, 67 (1-2), 3-17, doi:10.1016/0031-0182(88)90119-8.
- Foster, T. D., and E. C. Carmack (1976), Frontal zone mixing and Antarctic Bottom water formation in the southern Weddell Sea, *Deep Sea Research and Oceanographic Abstracts*, 23(4), 301-317, doi: 10.1016/0011-7471(76)90872-X.
- Franke, D., S. Neben, S. Ladage, B. Schreckenberger, and K. Hinz (2007), Margin segmentation and volcano-tectonic architecture along the volcanic margin off Argentina/Uruguay, South Atlantic, *Marine Geology*, 244(1), 46-67, doi: 10.1016/j.margeo.2007.06.009.
- Frederichs, T. h., and U. Bleil (2001), Volume susceptibility of sediment core GeoB6308-3., doi:doi:10.1594/PANGAEA.61168.
- Freeman, E., L. C. Skinner, C. Waelbroeck, and D. Hodell (2016), Radiocarbon evidence for enhanced respired carbon storage in the Atlantic at the Last Glacial Maximum, *Nat Commun*, 7, doi:10.1038/ncomms11998.
- Frenz, M., R. Höppner, J.-B. Stuut, T. Wagner, and R. Henrich (2003), Surface sediment bulk geochemistry and grain-size composition related to the oceanic circulation along the South American continental margin in the Southwest Atlantic, in *The South Atlantic in the Late Quaternary*, edited by G. Wefer, S. Mulitza and V. Ratmeyer, pp. 347-373, Springer, Berlin, Heidelberg.
- Gaiero, D. M., P. J. Depetris, J.-L. Probst, S. M. Bidart, and L. Leleyter (2004), The signature of river- and wind-borne materials exported from Patagonia to the southern latitudes: a view from REEs and implications for paleoclimatic interpretations, *Earth and Planetary Science Letters*, 219(3), 357-376, doi: 10.1016/S0012-821X(03)00686-1.
- Gaiero, D. M., J. L. Probst, P. J. Depetris, S. M. Bidart, and L. Leleyter (2003), Iron and other transition metals in Patagonian riverborne and windborne materials: geochemical control and transport to the southern South Atlantic Ocean, *Geochimica et Cosmochimica Acta*, 67(19), 3603-3623, doi:10.1016/S0016-7037(03)00211-4.
- Giberto, D. A., C. S. Bremec, E. M. Acha, and H. Mianzan (2004), Large-scale spatial patterns of benthic assemblages in the SW Atlantic: the Río de la Plata estuary and adjacent shelf waters, *Estuarine, Coastal and Shelf Science*, 61(1), 1-13, doi: 10.1016/j.ecss.2004.03.015.
- Goldstein, S.L., and Hemming, S.R. (2003), Long-lived isotopic tracers in oceanography, paleoceanography and ice-sheet dynamics, in *The Oceans and Marine Geochemistry, Treatise on Geochemistry, vol. 6*, edited by H.D. Holland and K.K. Turekian, pp. 453-489, Elsevier Science, Amsterdam, doi: 10.1016/B0-08-043751-6/06179-X.
- Goossens, D. (2008), Techniques to measure grain-size distributions of loamy sediments: a comparative study of ten instruments for wet analysis, *Sedimentology*, 55(1), 65-96, doi:10.1111/j.1365-3091.2007.00893.x.
- Gordon, A. L. (1971), Oceanography of Antarctic Waters, in *Antarctic Oceanology I*, edited by J. L. Ried, pp. 169-203, American Geophysical Union, Washington, D. C., doi:10.1029/AR015p0169.
- Gordon, A. L. (1981), South Atlantic thermocline ventilation, *Deep Sea Research Part A. Oceanographic Research Papers*, 28(11), 1239-1264, doi: 10.1016/0198-0149(81)90033-9.
- Gröger, M., R. Henrich, and T. Bickert (2003), Glacial-interglacial variability in lower North Atlantic deep water: inference from silt grain-size analysis and carbonate preservation in the western equatorial Atlantic, *Marine Geology*, 201, 321-332.
- Gwiliam, C. S. (1996), Modelling the global ocean circulation on the T3D., in *Parallel Computational Fluid Dynamics*, edited by A.S. Ecer, J.P.N.S Taylor, and S. Taylor, North Holland, Amsterdam, 33-40.
- Harris, P. T., and T. Whiteway (2011), Global distribution of large submarine canyons: Geomorphic differences between active and passive continental margins, *Marine Geology*, 285(1-4), 69-86, doi: 10.1016/j.margeo.2011.05.008.
- Hendry, K. R., L. Robinson, M. Meredith, S. Mulitza, C. M. Chiessi, and H. Arz (2012), Abrupt changes in high-latitude nutrient supply to the Atlantic during the last glacial cycle, *Geology*, 40(2), 123-126, doi: 10.1130/G32779.1.
- Henrich, R., K.-H. Baumann, S. Gerhardt, M. Gröger, and A. Volbers (2003), Carbonate preservation in deep and intermediate water masses in the South Atlantic: evaluation and geological record (a review), in *The South Atlantic in the Late Quaternary*, edited by G. Wefer, S. Mulitza and V. Ratmeyer, pp. 645-670, Springer, Berlin, Heidelberg.

- Henrich, R., Y. Cherubini, and H. Meggers (2010), Climate and sea level induced turbidite activity in a canyon system offshore the hyperarid Western Sahara (Mauritania): The Timiris Canyon, *Marine Geology*, 275(1–4), 178–198, doi: 10.1016/j.margeo.2010.05.011.
- Hernández-Molina, J., E. Llave, L. Somoza, M. C. Fernández-Puga, A. Maestro, R. León, T. Medialdea, A. Barnolas, M. García, and V. D. del Río (2003), Looking for clues to paleoceanographic imprints: a diagnosis of the Gulf of Cadiz contourite depositional systems, *Geology*, 31(1), 19–22, doi: 10.1130/0091-7613(2003)031<0019:LFC TPI>2.0.CO;2.
- Hernández-Molina, J., E. Llave, and D. Stow (2008a), Continental slope contourites, in *Contourites, Developments in Sedimentology*, vol. 60, edited by M. Rebesco and A. Camerlenghi, pp. 379–408, Elsevier, Amsterdam, Oxford, doi: 10.1016/S0070-4571(08)10019-X.
- Hernández-Molina, J., A. Maldonado, and D. Stow (2008b), Abyssal plain contourites, in *Contourites, Developments in Sedimentology*, vol. 60, edited by M. Rebesco and A. Camerlenghi, pp. 345–378, Elsevier, Amsterdam, Oxford, doi: 10.1016/S0070-4571(08)10018-8.
- Hernández-Molina, J., M. Paterlini, L. Somoza, R. Violante, M. A. Arecco, M. de Isasi, M. Rebesco, G. Uenzelmann-Neben, S. Neben, and P. Marshall (2010), Giant mounded drifts in the Argentine Continental Margin: Origins, and global implications for the history of thermohaline circulation, *Marine and Petroleum Geology*, 27(7), 1508–1530, doi:org/10.1016/j.marpetgeo.2010.04.003
- Hernández-Molina, J., M. Paterlini, R. Violante, P. Marshall, M. de Isasi, L. Somoza, and M. Rebesco (2009), Contourite depositional system on the Argentine Slope: an exceptional record of the influence of Antarctic water masses, *Geology*, 37(6), 507–510, doi:10.1130/G25578A.1.
- Hinz, K., S. Neben, B. Schreckenberger, H. A. Roeser, M. Block, K. G. d. Souza, and H. Meyer (1999), The Argentine continental margin north of 48°S: sedimentary successions, volcanic activity during breakup, *Marine and Petroleum Geology*, 16(1), 1–25, doi:org/10.1016/S0264-8172(98)00060-9.
- Hosegood, P., and H. van Haren (2003), Ekman-induced turbulence over the continental slope in the Faeroe–Shetland Channel as inferred from spikes in current meter observations, *Deep Sea Research Part I: Oceanographic Research Papers*, 50(5), 657–680, doi:10.1016/S0967-0637(03)00038-4.
- Howe, J. A., and C. J. Pudsey (1999), Antarctic Circumpolar Deep Water; a Quaternary paleoflow record from the northern Scotia Sea, South Atlantic Ocean, *Journal of Sedimentary Research*, 69(4), 847–861, doi:10.2110/jsr.69.847.
- Howe, J. N. W., A. M. Piotrowski, T. L. Noble, S. Mulitza, C. M. Chiessi, and G. Bayon (2016), North Atlantic Deep Water Production during the Last Glacial Maximum, *Nat Commun*, 7, doi:10.1038/ncomms11765.
- Huang, K.-F., D. W. Oppo, and W. B. Curry (2014), Decreased influence of Antarctic intermediate water in the tropical Atlantic during North Atlantic cold events, *Earth and Planetary Science Letters*, 389, 200–208, doi: 10.1016/j.epsl.2013.12.037.
- Jacobs, S. S., R. G. Fairbanks, and Y. Horibe (1985), Origin and Evolution of Water Masses Near the Antarctic continental Margin: Evidence from H218O/H216O Ratios in Seawater, in *Oceanology of the Antarctic Continental Shelf*, pp. 59–85, American Geophysical Union, doi:10.1029/AR043p0059.
- Jeandel, C. (1993), Concentration and isotopic composition of Nd in the South Atlantic Ocean, *Earth and Planetary Science Letters*, 117(3), 581–591, doi:10.1016/0012-821X(93)90104-H.
- Jonkers, L., M. A. Prins, G.-J. A. Brummer, M. Konert, and B. C. Lougheed (2009), Experimental insights into laser diffraction particle sizing of fine-grained sediments for use in palaeoceanography, *Sedimentology*, 56(7), 2192–2206, doi:10.1111/j.1365-3091.2009.01076.x.
- Jonkers, L., R. Zahn, A. Thomas, G. Henderson, W. Abouchami, R. François, P. Masque, I. R. Hall, and T. Bickert (2015), Deep circulation changes in the central South Atlantic during the past 145 kyrs reflected in a combined 231Pa/230Th, Neodymium isotope and benthic record, *Earth and Planetary Science Letters*, 419, 14–21, doi:10.1016/j.epsl.2015.03.004.
- Keeling, R. F., and B. B. Stephens (2001), Antarctic sea ice and the control of Pleistocene climate instability, *Paleoceanography*, 16(1), 112–131, doi:10.1029/2000PA000529.
- Keigwin, L. D., and E. A. Boyle (2008), Did North Atlantic overturning halt 17,000 years ago?, *Paleoceanography*, 23(1), doi:10.1029/2007PA001500.
- Kilmurray, J. (1975), Las Sierras Australes de la Provincia de Buenos Aires. Las fases de deformación y nueva interpretación

- estratigráfica, *Rev Asoc geol Argentina*, 30, 221-248.
- Killworth, P.D. (1977), Mixing on the Weddell Sea continental slope, *Deep-Sea Research*, 24, 427-448, doi.org/10.1016/0146-6291(77)90482-9.
- Krastel, S., H. U. Schmincke, and C. Jacobs (2001), Formation of submarine canyons on the flanks of the Canary Islands, *Geo-Marine Letters*, 20(3), 160-167, doi: 10.1007/s003670000049.
- Krastel, S., G. Wefer, T. J. Hanebuth, A. A. Antobreh, T. Freudenthal, B. Preu, T. Schwenk, M. Strasser, R. Violante, and D. Winkelmann (2011), Sediment dynamics and geohazards off Uruguay and the de la Plata River region (northern Argentina and Uruguay), *Geo-Marine Letters*, 31(4), 271-283, doi: 10.1007/s00367-011-0232-4
- Krastel, S., G. Wefer, and cruise participants (2012), Report and preliminary results of RV METEOR Cruise M78/3. Sediment transport off Uruguay and Argentina: From the shelf to the deep sea. 19.05.2009 – 06.07.2009, Montevideo (Uruguay) – Montevideo (Uruguay). Berichte aus dem Fachbereich für Geowissenschaften, Universität Bremen, 285, 79.
- Krueger, S., D. C. Leuschner, W. Ehrmann, G. Schmiedl, and A. Mackensen (2012), North Atlantic Deep Water and Antarctic Bottom Water variability during the last 200 ka recorded in an abyssal sediment core off South Africa, *Global and Planetary Change*, 80–81, 180-189, doi: 10.1016/j.gloplacha.2011.10.001.
- Krueger, S., D. C. Leuschner, W. Ehrmann, G. Schmiedl, A. Mackensen, and B. Diekmann (2008), Ocean circulation patterns and dust supply into the South Atlantic during the last glacial cycle revealed by statistical analysis of kaolinite/chlorite ratios, *Marine Geology*, 253(3–4), 82-91, doi:10.1016/j.margeo.2008.04.015.
- Kuhlbrodt, T., A. Griesel, M. Montoya, A. Levermann, M. Hofmann, and S. Rahmstorf (2007), On the driving processes of the Atlantic meridional overturning circulation, *Reviews of Geophysics*, 45(2), doi:10.1029/2004RG000166.
- Kuhn, G., and B. Diekmann (2002), Late Quaternary variability of ocean circulation in the southeastern South Atlantic inferred from the terrigenous sediment record of a drift deposit in the southern Cape Basin (ODP Site 1089), *Palaeogeography, Palaeoclimatology, Palaeoecology*, 182(3–4), 287-303, doi: 10.1016/S0031-0182(01)00500-4.
- Kwon, E. Y., M. P. Hain, D. M. Sigman, E. D. Galbraith, J. L. Sarmiento, and J. R. Toggweiler (2012), North Atlantic ventilation of “southern-sourced” deep water in the glacial ocean, *Paleoceanography*, 27(2), doi:10.1029/2011PA002211.
- Laberg, J. S. and A. Camerlenghi (2008), The Significance of Contourites for Submarine Slope Stability, in *Contourites, Developments in Sedimentology*, edited by M. Rebesco and A. Camerlenghi, pp. 537-556, Elsevier, Amsterdam, Oxford, doi:10.1016/S0070-4571(08)10025-5.
- Lamy, F., H. W. Arz, R. Kilian, C. B. Lange, L. Lembke-Jene, M. Wengler, J. Kaiser, O. Baeza-Urrea, I. R. Hall, and N. Harada (2015), Glacial reduction and millennial-scale variations in Drake Passage throughflow, *Proceedings of the National Academy of Sciences*, 112(44), 13496-13501, doi: 10.1073/pnas.1509203112.
- Lantzsch, H., T. J. J. Hanebuth, C. M. Chiessi, T. Schwenk, and R. A. Violante (2014), The high-supply, current-dominated continental margin of southeastern South America during the late Quaternary, *Quaternary Research*, 81(2), 339-354, doi:10.1016/j.yqres.2014.01.003.
- Lippold, J., et al. (2016), Deep water provenance and dynamics of the (de)glacial Atlantic meridional overturning circulation, *Earth and Planetary Science Letters*, 445, 68-78, doi: 10.1016/j.epsl.2016.04.013.
- Liu, X., R. Rendle-Bühning, and R. Henrich (2016), Climate and sea-level controls on turbidity current activity on the Tanzanian upper slope during the last deglaciation and the Holocene, *Quaternary Science Reviews*, 133, 15-27, doi: 10.1016/j.quascirev.2015.12.002.
- Lopes dos Santos, R. A., M. Prange, I. S. Castañeda, E. Schefuß, S. Mulitza, M. Schulz, E. M. Niedermeyer, J. S. Sinninghe Damsté, and S. Schouten (2010), Glacial–interglacial variability in Atlantic meridional overturning circulation and thermocline adjustments in the tropical North Atlantic, *Earth and Planetary Science Letters*, 300(3), 407-414, doi: 10.1016/j.epsl.2010.10.030.
- Lumpkin, R., and K. Speer (2007), Global Ocean Meridional Overturning, *Journal of Physical Oceanography*, 37(10), 2550-2562, doi:10.1175/jpo3130.1.
- Lund, D. C., J. F. Adkins, and R. Ferrari (2011), Abyssal Atlantic circulation during the Last Glacial Maximum: Constraining the ratio between transport and vertical mixing,

- Paleoceanography*, 26(1), doi:10.1029/2010PA001938.
- Lund, D. C., A. Tessin, J. Hoffman, and A. Schmittner (2015), Southwest Atlantic water mass evolution during the last deglaciation, *Paleoceanography*, 30(5), 477-494, doi:10.1002/2014PA002657.
- Lynch-Stieglitz, J., et al. (2007), Atlantic Meridional Overturning Circulation During the Last Glacial Maximum, *Science*, 316(5821), 66-69, doi:10.1126/science.1137127.
- Mahiques, M.M., Tassinari, C.C.G., Marcolini, S., Violante, R.A., Figueira, R.C.L., da Silveira, I.C.A., Burone, L., de Mello e Sousa, S.H. (2008), Nd and Pb isotope signatures on the Southeastern South American upper margin: implications for sediment transport and source rocks. *Marine Geology* 250 (1-2), 51-63, doi: 10.1016/j.margeo.2007.11.007.
- Marchitto, T. M., and W. S. Broecker (2006), Deep water mass geometry in the glacial Atlantic Ocean: A review of constraints from the paleonutrient proxy Cd/Ca, *Geochemistry, Geophysics, Geosystems*, 7(12), Q12003, doi:10.1029/2006GC001323.
- Marchitto, T. M., W. B. Curry, and D. W. Oppo (1998), Millennial-scale changes in North Atlantic circulation since the last glaciation, *Nature*, 393(6685), 557-561, doi:10.1038/31197.
- Marsland, S. J., J. A. Church, N. L. Bindoff, and G. D. Williams (2007), Antarctic coastal polynya response to climate change, *Journal of Geophysical Research: Oceans*, 112(C7), doi:10.1029/2005JC003291.
- McCave, I. N. (2008), Chapter 8 Size Sorting During Transport and Deposition of Fine Sediments: Sortable Silt and Flow Speed, in *Contourites, Developments in Sedimentology, vol. 60*, edited by M. Rebesco and A. Camerlenghi, pp. 121-142, Elsevier, Amsterdam, Oxford, doi: 10.1016/S0070-4571(08)10008-5.
- McCave, I. N., S. J. Crowhurst, G. Kuhn, C. D. Hillenbrand, and M. P. Meredith (2014), Minimal change in Antarctic Circumpolar Current flow speed between the last glacial and Holocene, *Nature Geosci*, 7(2), 113-116, doi:10.1038/ngeo2037
- McCave, I. N., and I. R. Hall (2006), Size sorting in marine muds: Processes, pitfalls, and prospects for paleoflow-speed proxies, *Geochemistry, Geophysics, Geosystems*, 7(10), doi:10.1029/2006GC001284.
- McCave, I. N., I. R. Hall, and G. G. Bianchi (2006), Laser vs. settling velocity differences in silt grainsize measurements: estimation of palaeocurrent vigour, *Sedimentology*, 53(4), 919-928, doi:10.1111/j.1365-3091.2006.00783.x.
- McCave, I. N., B. Manighetti, and S. G. Robinson (1995), Sortable silt and fine sediment size/composition slicing: Parameters for palaeocurrent speed and palaeoceanography, *Paleoceanography*, 10(3), 593-610, doi:10.1029/94PA03039.
- McCave, I. N., D. J. R. Thornalley, and I. R. Hall (2017, in press), Relation of sortable silt grain-size to deep-sea current speeds: Calibration of the 'Mud Current Meter', *Deep Sea Research Part I: Oceanographic Research Papers*, doi:10.1016/j.dsr.2017.07.003.
- McManus, J. F., R. Francois, J. M. Gherardi, L. D. Keigwin, and S. Brown-Leger (2004), Collapse and rapid resumption of Atlantic meridional circulation linked to deglacial climate changes, *Nature*, 428(6985), 834-837.
- Menviel, L., J. Yu, F. Joos, A. Mouchet, K. J. Meissner, and M. H. England (2016), Poorly ventilated deep ocean at the Last Glacial Maximum inferred from carbon isotopes: a data-model comparison study, *Paleoceanography*, doi:10.1002/2016PA003024.
- Mix, A. C., E. Bard, and R. Schneider (2001), Environmental processes of the ice age: land, oceans, glaciers (EPILOG), *Quaternary Science Reviews*, 20(4), 627-657, doi:10.1016/S0277-3791(00)00145-1.
- Mollenhauer, G., J. F. McManus, A. Benthien, P. J. Müller, and T. I. Eglinton (2006), Rapid lateral particle transport in the Argentine Basin: Molecular 14C and 230Thxs evidence, *Deep Sea Research Part I: Oceanographic Research Papers*, 53(7), 1224-1243, doi: 10.1016/j.dsr.2006.05.005.
- Moore, D. M., and R. C. Reynolds (1989), *X-ray Diffraction and the Identification and Analysis of Clay Minerals*, Oxford University press, Oxford.
- Mulder, T., et al. (2006), The western part of the Gulf of Cadiz: contour currents and turbidity currents interactions, *Geo-Marine Letters*, 26(1), 31-41, doi:10.1007/s00367-005-0013-z.
- Mulitza, S., M. Prange, J. B. Stuut, M. Zabel, T. von Dobeneck, A. C. Itambi, J. Nizou, M. Schulz, and G. Wefer (2008), Sahel megadroughts triggered by glacial slowdowns of Atlantic meridional overturning, *Paleoceanography*, 23(4), doi: 10.1029/2008PA001637.
- Müller, P. J., and R. Schneider (1993), An automated leaching method for the

- determination of opal in sediments and particulate matter, *Deep Sea Research Part I: Oceanographic Research Papers*, 40(3), 425-444, doi:10.1016/0967-0637(93)90140-X.
- Negre, C., R. Zahn, A. L. Thomas, P. Masque, G. M. Henderson, G. Martinez-Mendez, I. R. Hall, and J. L. Mas (2010), Reversed flow of Atlantic deep water during the Last Glacial Maximum, *Nature*, 468(7320), 84-88, doi:10.1038/nature09508.
- Nittrouer, C. A., and L. D. Wright (1994), Transport of particles across continental shelves, *Reviews of Geophysics*, 32(1), 85-113, doi:10.1029/93RG02603.
- Ohshima, K. I., Y. Fukamachi, G. D. Williams, S. Nihashi, F. Roquet, Y. Kitade, T. Tamura, D. Hirano, L. Herraiz-Borreguero, and I. Field (2013), Antarctic Bottom Water production by intense sea-ice formation in the Cape Darnley polynya, *Nature Geoscience*, 6(3), 235.
- Oldfield, F. (1991), Environmental magnetism — A personal perspective, *Quaternary Science Reviews*, 10(1), 73-85, doi:10.1016/0277-3791(91)90031-O.
- Olson, D. B., G. P. Podesta, R. H. Evans, and O. B. Brown (1988), Temporal variations in the separation of Brazil and Malvinas Currents, *Deep Sea Research Part A. Oceanographic Research Papers*, 35(12), 1971-1990, doi:10.1016/0198-0149(88)90120-3.
- Oppo, D. W., and W. B. Curry (2012), Deep Atlantic circulation during the Last Glacial Maximum and deglaciation, *Nat. Educ. Knowl*, 3(10), 1.
- Oppo, D. W., and R. G. Fairbanks (1987), Variability in the deep and intermediate water circulation of the Atlantic Ocean during the past 25,000 years: Northern Hemisphere modulation of the Southern Ocean, *Earth and Planetary Science Letters*, 86(1), 1-15, doi:10.1016/0012-821X(87)90183-X.
- Orange, D. L., and N. A. Breen (1992), The effects of fluid escape on accretionary wedges 2. Seepage force, slope failure, headless submarine canyons, and vents, *Journal of Geophysical Research: Solid Earth*, 97(B6), 9277-9295, doi:10.1029/92JB00460.
- Orsi, A. H., G. C. Johnson, and J. L. Bullister (1999), Circulation, mixing, and production of Antarctic Bottom Water, *Progress in Oceanography*, 43(1), 55-109, doi:10.1016/S0079-6611(99)00004-X.
- Orsi, A. H., T. Whitworth, and W. D. Nowlin (1995), On the meridional extent and fronts of the Antarctic Circumpolar Current, *Deep Sea Research Part I: Oceanographic Research Papers*, 42(5), 641-673, doi:10.1016/0967-0637(95)00021-W.
- Pahnke, K., S. L. Goldstein, and S. R. Hemming (2008), Abrupt changes in Antarctic Intermediate Water circulation over the past 25,000 years, *Nature Geosci*, 1(12), 870-874.
- Peterson, R. G., C. S. Johnson, W. Krauss, and R. E. Davis (1996), Lagrangian Measurements in the Malvinas Current, in *The South Atlantic: Present and Past Circulation*, edited by G. Wefer, W.H. Berger, G. Siedler and D.J. Webb, pp. 239-247, Springer, Berlin, Heidelberg, doi:10.1007/978-3-642-80353-6_12.
- Peterson, R. G., and L. Stramma (1991), Upper-level circulation in the South Atlantic Ocean, *Progress in oceanography*, 26(1), 1-73, doi:10.1016/0079-6611(91)90006-8.
- Petschick, R., G. Kuhn, and F. Gingele (1996), Clay mineral distribution in surface sediments of the South Atlantic: sources, transport, and relation to oceanography, *Marine Geology*, 130(3-4), 203-229, doi:10.1016/0025-3227(95)00148-4.
- Pierau, R., T. J. J. Hanebuth, S. Krastel, and R. Henrich (2010), Late Quaternary climatic events and sea-level changes recorded by turbidite activity, Dakar Canyon, NW Africa, *Quaternary Research*, 73(2), 385-392, doi:10.1016/j.yqres.2009.07.010.
- Piola, A. R., and A. L. Gordon (1989), Intermediate waters in the southwest South Atlantic, *Deep Sea Research Part A. Oceanographic Research Papers*, 36(1), 1-16, doi:10.1016/0198-0149(89)90015-0.
- Piola, A. R., and R. Matano (2001), Brazil and Falklands (Malvinas) currents, in *Encyclopedia of Ocean Sciences: Ocean currents*, 2nd edition, edited by J.H. Steele, S.A. Thorpe, and K.K. Turekian, pp. 35-43, Elsevier, London, Burlington, San Diego.
- Piola, A. R., R. P. Matano, E. D. Palma, O. O. Möller, and E. J. Campos (2005), The influence of the Plata River discharge on the western South Atlantic shelf, *Geophysical Research Letters*, 32(1), doi:10.1029/2004GL021638.
- Piper, D. J. (2005), Late Cenozoic evolution of the continental margin of eastern Canada, *Norwegian Journal of Geology/Norsk geologisk tidsskrift*, 85(4), 305.
- Piper, D. J. W., P. Cochonot, and M. L. Morrison (1999), The sequence of events around the epicentre of the 1929 Grand Banks earthquake: initiation of debris flows and turbidity current inferred from sidescan

- sonar, *Sedimentology*, 46(1), 79-97, doi:10.1046/j.1365-3091.1999.00204.x.
- Pomar, L., M. Morsilli, P. Hallock, and B. Bádenas (2012), Internal waves, an under-explored source of turbulence events in the sedimentary record, *Earth-Science Reviews*, 111(1), 56-81, doi:10.1016/j.earscirev.2011.12.005.
- Pratson, L. F., and B. J. Coakley (1996), A model for the headward erosion of submarine canyons induced by downslope-eroding sediment flows, *Geological Society of America Bulletin*, 108(2), 225-234, doi: 10.1130/0016-7606(1996)108<0225:AMFTHE>2.3.CO;2.
- Pratson, L. F., W. B. Ryan, G. S. Mountain, and D. C. Twichell (1994), Submarine canyon initiation by downslope-eroding sediment flows: evidence in late Cenozoic strata on the New Jersey continental slope, *Geological Society of America Bulletin*, 106(3), 395-412, doi: 10.1130/0016-7606(1994)106<0395:SCIBDE>2.3.CO;2.
- Preu, B., F. J. Hernández-Molina, R. Violante, A. R. Piola, C. M. Paterlini, T. Schwenk, I. Voigt, S. Krastel, and V. Spiess (2013), Morphosedimentary and hydrographic features of the northern Argentine margin: The interplay between erosive, depositional and gravitational processes and its conceptual implications, *Deep Sea Research Part I: Oceanographic Research Papers*, 75, 157-174, doi: 10.1016/j.dsr.2012.12.013.
- Preu, B., T. Schwenk, F. J. Hernández-Molina, R. Violante, M. Paterlini, S. Krastel, J. Tomasini, and V. Spieß (2012), Sedimentary growth pattern on the northern Argentine slope: the impact of North Atlantic Deep Water on southern hemisphere slope architecture, *Marine Geology*, 329, 113-125, doi: 10.1016/j.margeo.2012.09.009.
- Puig, P., A. Palanques, and J. Martín (2014), Contemporary sediment-transport processes in submarine canyons, *Annual review of marine science*, 6, 53-77, doi: 10.1146/annurev-marine-010213-135037.
- Rahmstorf, S. (2002), Ocean circulation and climate during the past 120,000 years, *Nature*, 419(6903), 207-214.
- Rebesco, M. (2014), Contourites, in *Reference Module in Earth Systems and Environmental Sciences*, Elsevier, doi:10.1016/B978-0-12-409548-9.09094-1.
- Reid, J. L. (1989), On the total geostrophic circulation of the South Atlantic Ocean: Flow patterns, tracers, and transports, *Progress in Oceanography*, 23(3), 149-244, doi: 10.1016/0079-6611(89)90001-3.
- Reid, J. L. (1996), On the circulation of the South Atlantic Ocean, in *The South Atlantic – Present and Past Circulation*, edited by G. Wefer, H. Berger, G. Siedler, D.J. Webb, pp. 13-44, Springer, Berlin, Heidelberg, doi: 10.1007/978-3-642-80353-6
- Reid, J. L., W. D. Nowlin Jr, and W. C. Patzert (1977), On the characteristics and circulation of the southwestern Atlantic Ocean, *Journal of Physical Oceanography*, 7(1), 62-91, doi:10.1175/1520-0485(1977)007<0062:OTCACO>2.0.CO;2.
- Reimer, P. J., E. Bard, A. Bayliss, J. W. Beck, P. G. Blackwell, C. Bronk Ramsey, C. E. Buck, H. Cheng, R. L. Edwards, and M. Friedrich (2013), IntCal13 and Marine13 radiocarbon age calibration curves 0-50,000 years cal BP, *Radiocarbon*, 55, 1869-1887, doi: 10.2458/azu_js_rc.55.16947.
- Roberts, J., I. N. McCave, E. L. McClymont, S. Kender, C. D. Hillenbrand, R. Matano, D. A. Hodell, and V. L. Peck (2017), Deglacial changes in flow and frontal structure through the Drake Passage, *Earth and Planetary Science Letters*, 474, 397-408, doi: 10.1016/j.epsl.2017.07.004.
- Roberts, N. L., A. M. Piotrowski, J. F. McManus, and L. D. Keigwin (2010), Synchronous Deglacial Overturning and Water Mass Source Changes, *Science*, 327(5961), 75-78, doi:10.1126/science.1178068.
- Robinson, S. G., and I. N. McCave (1994), Orbital forcing of bottom-current enhanced sedimentation on Feni Drift, NE Atlantic, during the mid-Pleistocene, *Paleoceanography*, 9(6), 943-972, doi:10.1029/94PA01439
- Rutberg, R. L., S. R. Hemming, and S. L. Goldstein (2000), Reduced North Atlantic Deep Water flux to the glacial Southern Ocean inferred from neodymium isotope ratios, *Nature*, 405(6789), 935-938.
- Ryan, W. B. F., et al. (2009), Global Multi-Resolution Topography synthesis, *Geochemistry, Geophysics, Geosystems*, 10(3), doi:10.1029/2008GC002332.
- Sarnthein, M., K. Winn, S. J. A. Jung, J.-C. Duplessy, L. Labeyrie, H. Erlenkeuser, and G. Ganssen (1994), Changes in East Atlantic Deepwater Circulation over the last 30,000 years: Eight time slice reconstructions, *Paleoceanography*, 9(2), 209-267, doi:10.1029/93PA03301.
- Schlitzer, R (2002), Interactive analysis and visualization of geoscience data with Ocean Data View, *Computers &*

- Geosciences*, 28(10), 1211-1218, doi: 10.1016/S0098-3004(02)00040-7.
- Schlitzer, R. (2015), Ocean Data View, <http://odv.awi.de>.
- Segl, M., and cruise participants (1994), Report and preliminary results of Meteor-Cruise M29/1, Buenos-Aires - Montevideo, 17.6.-13.7.1994, *Berichte aus dem Fachbereich für Geowissenschaften, Universität Bremen*, 58.
- Shanmugam, G. (1997), The Bouma Sequence and the turbidite mind set, *Earth-Science Reviews*, 42, 201-229.
- Skinner, L. C., S. Fallon, C. Waelbroeck, E. Michel, and S. Barker (2010), Ventilation of the Deep Southern Ocean and Deglacial CO₂ Rise, *Science*, 328(5982), 1147-1151, doi:10.1126/science.1183627.
- Skinner, L. C., A. Scrivner, D. Vance, S. Barker, S. Fallon, and C. Waelbroeck (2013), North Atlantic versus Southern Ocean contributions to a deglacial surge in deep ocean ventilation, *Geology*, 41(6), 667-670, doi: 10.1130/G34133.1.
- Smith, J., D. Vance, R. A. Kemp, C. Archer, P. Toms, M. King, and M. Zárate (2003), Isotopic constraints on the source of Argentinian loess – with implications for atmospheric circulation and the provenance of Antarctic dust during recent glacial maxima, *Earth and Planetary Science Letters*, 212(1), 181-196, doi: 10.1016/S0012-821X(03)00260-7.
- Smith, J. A., C.-D. Hillenbrand, C. J. Pudsey, C. S. Allen, and A. G. C. Graham (2010), The presence of polynyas in the Weddell Sea during the Last Glacial Period with implications for the reconstruction of sea-ice limits and ice sheet history, *Earth and Planetary Science Letters*, 296(3-4), 287-298, doi: 10.1016/j.epsl.2010.05.008.
- Spieß, V., and cruise participants (2003), Report and Preliminary results of Meteor cruise M49/1 Cape Town (South Africa) - Montevideo (Uruguay) 04.01.2000 - 10.02.2000, *Berichte aus dem Fachbereich Geowissenschaften, Universität Bremen*, 205.
- Stichel, T., M. Frank, J. Rickli, and B. A. Haley (2012), The hafnium and neodymium isotope composition of seawater in the Atlantic sector of the Southern Ocean, *Earth and Planetary Science Letters*, 317, 282-294, doi:10.1016/j.epsl.2011.11.025.
- Stow, D. A. V., J.-C. Faugères, J. A. Howe, C. J. Pudsey, and A. R. Viana (2002), Bottom currents, contourites and deep-sea sediment drifts: current state-of-the-art, *Geological Society*, 22(1), 7-20, London, doi:10.1144/gsl.mem.2002.022.01.02.
- Stow, D. A. V., and J. C. Faugères (2008), Contourite Facies and the Facies Model, in *Contourites, Developments in Sedimentology*, vol. 60, edited by M. Rebesco and A. Camerlenghi, pp. 223-256, Elsevier, Amsterdam, Oxford, doi:10.1016/S0070-4571(08)10013-9.
- Stow, D. A. V., S. Hunter, D. Wilkinson, and F. J. Hernández-Molina (2008), The Nature of Contourite Deposition, in *Contourites, Developments in Sedimentology*, edited by M. Rebesco and A. Camerlenghi, pp. 143-156, Elsevier, Amsterdam, Oxford, doi:10.1016/S0070-4571(08)10009-7.
- Stramma, L., and M. England (1999), On the water masses and mean circulation of the South Atlantic Ocean, *Journal of Geophysical Research: Oceans*, 104(C9), 20863-20883, doi:10.1029/1999JC900139.
- Stuiver, M., and P. J. Reimer (2016), Extended 14C Data Base and Revised CALIB 3.0 14C Age Calibration Program, *Radiocarbon*, 35(1), 215-230, doi:10.1017/S0033822200013904.
- Talley, L. D. (2013), Some aspects of ocean heat transport by the shallow, intermediate and deep overturning Circulations, in *Mechanisms of Global Climate Change at Millennial Time Scales*, edited by P.U. Clark, R.S. Webb and L.D. Keigwin, pp. 1-22, American Geophysical Union, Washington, D.C., doi:10.1029/GM112p0001.
- Tamura, T., K. I. Ohshima, and S. Nishihashi (2008), Mapping of sea ice production for Antarctic coastal polynyas, *Geophysical Research Letters*, 35(7), doi:10.1029/2007GL032903.
- Toggweiler, J. R. (1999), Variation of atmospheric CO₂ by ventilation of the ocean's deepest water, *Paleoceanography*, 14(5), 571-588, doi:10.1029/1999PA900033.
- Twicheil, D. C., and D. G. Roberts (1982), Morphology, distribution, and development of submarine canyons on the United States Atlantic continental slope between Hudson and Baltimore Canyons, *Geology*, 10(8), 408-412, doi:10.1130/0091-613(1982)10<408:mdados>2.0.co;2.
- Urien, C. M., and M. Ewing (1974), Recent Sediments and Environment of Southern Brazil, Uruguay, Buenos Aires, and Rio Negro Continental Shelf, in *The Geology of Continental Margins*, edited by C.A. Burk and C.L. Drake, pp. 157-177, Springer Berlin Heidelberg, doi:10.1007/978-3-662-01141-6_12.

- Violante, R. A., C. M. Paterlini, I. P. Costa, F. J. Hernández-Molina, L. M. Segovia, J. L. Cavalotto, S. Marcolini, G. Bozzano, C. Laprida, and N. García Chaporí (2010), Sismoestratigrafía y evolución geomorfológica del talud continental adyacente al litoral del este bonaerense, Argentina, *Latin American Journal of Sedimentology and basin analysis*, 17(1), 33-62.
- Vogt, C., J. Lauterjung, and R. X. Fischer (2002), Investigation of the Clay Fraction (< 2 µm) of the Clay Minerals Society Reference Clays, *Clays, Clays and Clay Minerals*, 50(3), 388-400, doi: 10.1346/000986002760833765.
- Voigt, I., C. M. Chiessi, A. R. Piola, and R. Henrich (2016), Holocene changes in Antarctic Intermediate Water flow strength in the Southwest Atlantic, *Palaeogeography, Palaeoclimatology, Palaeoecology*, 463, 60-67, doi: 10.1016/j.palaeo.2016.09.018.
- Voigt, I., C. M. Chiessi, M. Prange, S. Mulitza, J. Groeneveld, V. Varma, and R. Henrich (2015), Holocene shifts of the southern westerlies across the South Atlantic, *Paleoceanography*, 30(2), 39-51, doi:10.1002/2014PA002677.
- Voigt, I., A.P.S. Cruz, S. Mulitza, C.M. Chiessi, A. Mackensen, J. Lippold, B. Antz, M. Zabel, Y. Zhang, C.F. Barbosa, and A.A. Tisserand (2017), Variability in mid-depth ventilation of the western Atlantic Ocean during the last deglaciation, *Paleoceanography*, 32, 948-965, doi:10.1002/2017PA003095.
- Voigt, I., R. Henrich, B. M. Preu, A. R. Piola, T. J. J. Hanebuth, T. Schwenk, and C. M. Chiessi (2013), A submarine canyon as a climate archive — Interaction of the Antarctic Intermediate Water with the Mar del Plata Canyon (Southwest Atlantic), *Marine Geology*, 341, 46-57, doi: 10.1016/j.margeo.2013.05.002.
- Volbers, A. N. A., and R. Henrich (2002), Present water mass calcium carbonate corrosiveness in the eastern South Atlantic inferred from ultrastructural breakdown of *Globigerina bulloides* in surface sediments, *Marine Geology*, 186(3-4), 471-486, doi: 10.1016/S0025-3227(02)00333-X.
- Volbers, A. N. A., and R. Henrich (2004), Calcium carbonate corrosiveness in the South Atlantic during the Last Glacial Maximum as inferred from changes in the preservation of *Globigerina bulloides*: A proxy to determine deep-water circulation patterns?, *Marine Geology*, 204(1-2), 43-57, doi: 10.1016/S0025-3227(03)00372-4.
- von Lom-Keil, H., V. Spieß, and V. Hopfauf (2002), Fine-grained sediment waves on the western flank of the Zapiola Drift, Argentine Basin: evidence for variations in Late Quaternary bottom flow activity, *Marine Geology*, 192(1), 239-258, doi: 10.1016/S0025-3227(02)00557-1.
- Walter, H.J., E. Hegner, B. Diekmann, G. Kuhn, and M.M. Rutgers van der Loeff (2000), Provenance and transport of terrigenous sediment in the south Atlantic Ocean and their relations to glacial and interglacial cycles: Nd and Sr isotopic evidence, *Geochimica et Cosmochimica Acta*, 64(12), 3813-3827, doi:10.1016/S0016-7037(00)00476-2.
- Warratz, G., R. Henrich, I. Voigt, C. M. Chiessi, G. Kuhn, and H. Lantzsch (2017), Deglacial changes in the strength of deep southern component water and sediment supply at the Argentine continental margin, *Paleoceanography*, 32, 796-812, doi:10.1002/2016PA003079.
- Weaver, A. J., O. A. Saenko, P. U. Clark, and J. X. Mitrovica (2003), Meltwater Pulse 1A from Antarctica as a Trigger of the Bølling-Allerød Warm Interval, *Science*, 299(5613), 1709-1713, doi:10.1126/science.1081002.
- Whitworth, T., and W. D. Nowlin (1987), Water masses and currents of the Southern Ocean at the Greenwich Meridian, *Journal of Geophysical Research: Oceans*, 92(C6), 6462-6476, doi:10.1029/JC092iC06p06462.
- Wien, K., C. Holz, M. Kölling, and H. D. Schulz (2006), Age models for pelagites and turbidites from the Cap Timiris Canyon off Mauritania, *Marine and Petroleum Geology*, 23(3), 337-352, doi:10.1016/j.marpetgeo.2005.10.005.
- Zárate, M. A. (2003), Loess of southern South America, *Quaternary Science Reviews*, 22(18), 1987-2006, doi: 10.1016/S0277-3791(03)00165-3.
- Zweng, M. M., et al. (2013), World Ocean Atlas 2013, Salinity, NOAA Atlas NESDIS 72, 2(74), 39.

Acknowledgements

First of all, I wish to thank *Prof. Rüdiger Henrich* for giving me the opportunity to conduct this PhD project. I would like to thank him for his patience and enthusiasm, and for giving me the opportunity to work efficiently and independently.

I feel honored and like to thank *Prof. Bernhard Diekmann* for agreeing on being the second reviewer of my thesis.

I would like to thank all co-authors: *Dr. Ines Voigt, Dr. Hendrik Lantzsch, Dr. Tilmann Schwenk, Prof. Gerhard Kuhn, Dr. Graziella Bozzano, Prof. Roberto Violante, and Dr. Cristiano Chiessi*. Many thanks for all discussions, revisions and critical remarks that significantly improved the content and quality of the manuscripts. I greatly benefitted from these close collaborations and I am thankful for all supporting and encouraging words, which gave me the chance to improve my scientific knowledge and efficient methods.

Special thanks go to the Paleoceanography and Sedimentology working group. *Hendrik, Kalle, Brit, Debs, Catarina and Mariem*: thank you for your support. *Debs*, thanks for being such a balanced and calm office roommate, who gave me the space to work focused and efficiently. I wish to thank *Brit* for your scientific/technical/administrative assistance and human support in challenging situations. Thank you *Hendrik*, for the opportunity to participate in POS482 and all inspiring scientific discussions. I also like to thank my student assistants *Johanna* and *Johannes*, who helped me to deal with the large quantities of samples.

I also like to thank *Christoph Vogt* for XRD measurements. I thank *Ursula Röhl* and *Vera Luckies* for the support during XRF core scans as well as *Jürgen Titschack* for the support in the Laser Coulter lab.

I also like to thank the Bremen International Graduate School for Marine Sciences (GLOMAR) for supporting me financially to present my work during international conferences and courses, i.e. the IGC 2016 in Cape Town (South Africa) and the IMS 2017 in Toulouse (France). In addition, GLOMAR gave me the chance to broaden my mind and to educate myself by attending courses. Herewith I wish to thank all other members of my GLOMAR thesis committee not mentioned before: *Prof. Sebastian Krastel, Dr. Sabine Kasten* and *Prof. Javier Hernández-Molina*.

Life and work would have been less beneficial without you: Thank you *Asli, Carlos, Debs, Fenna, Julia, Lena, Nora, Stefan*, and all others I forgot to mention here.

I would certainly not be where I am today without my family. Many thanks again to my parents, *Ruth* and *Jürgen*, for all your love, support and assistance during the last 29 years of life.

Special thanks to my sister *Brigit*, my cousin *Anne*, and my dearest friends *Sandra* and *Cordy* from far away for the wonderful time together.

Finally I wish to thank *Jan*. Your constant encouragement and support brought a lot of happiness in my life. You are the best that could have ever happened to me.

***„What we know is drop,
what we don't know is an ocean“***

Issac Newton
(* 04.01.1643 † 31.03.1727)

